

PDEformer-2: A Versatile Foundation Model for Two-Dimensional Partial Differential Equations

Zhanhong Ye¹, Zining Liu², Bingyang Wu², Hongjie Jiang²,
Leheng Chen¹, Minyan Zhang⁶, Xiang Huang⁷, Qinghe Meng⁸,
Jingyuan Zou⁸, Hongsheng Liu⁶, Bin Dong^{1,3,4,5*}

^{1*}Beijing International Center for Mathematical Research, Peking University, Beijing, China.

²School of Mathematical Sciences, Peking University, Beijing, China.

³Center for Machine Learning Research, Peking University, Beijing, China.

⁴Beijing International Center for Mathematical Research and the New Cornerstone Science Laboratory, Peking University, Beijing, China.

⁵Zhongguancun Academy, Beijing, China.

⁶Central Software Institute, Huawei Technology Co. Ltd, Shanghai, China.

⁷Central Software Institute, Huawei Technology Co. Ltd, Hangzhou, China.

⁸Computing Product Line, Huawei Technology Co. Ltd, Hangzhou, China.

*Corresponding author(s). E-mail(s): dongbin@math.pku.edu.cn;

Contributing authors: yezhanhong@pku.edu.cn; liuzining@stu.pku.edu.cn;
wby2003@stu.pku.edu.cn; jianghongjie@stu.pku.edu.cn;
chenlh@pku.edu.cn; zhangminyan3@huawei.com;
huangxiang42@huawei.com; qinghe.meng@huawei.com;
zoujingyuan@huawei.com; liuhongsheng4@huawei.com;

Abstract

Partial differential equations (PDEs) play a central role in describing many physical phenomena. Various scientific and engineering applications demand a versatile and differentiable PDE solver that can quickly generate solutions with adequate accuracy, and limitations of the traditional solvers and specialized neural operators motivate the development of foundation models for solving PDEs. This paper introduces PDEformer-2, a versatile foundation model for two-dimensional PDEs. Based on our previous one-dimensional PDEformer-1 model, PDEformer-2 receives the PDE form as network input via computational graph representation,

which has the flexibility to encode most common PDEs. The mesh-free predicted solutions can be directly queried at arbitrary spatio-temporal coordinates. A large (40TB) diverse dataset is employed to pretrain the current model, making it capable of simultaneously addressing PDEs with different symbolic forms, domain shapes, boundary conditions, number of variables, and time-dependency. Accurate zero-shot prediction is allowed for PDEs that resemble the pretraining ones. When adapted to new unseen PDEs, PDEformer-2 demonstrates faster learning than many specialized models, and has smaller errors given limited (less than 100) samples. Additionally, PDEformer-2 can be employed in the inverse problems thanks to its fast and differentiable nature, and produces reasonable results in our experiments to recover coefficient scalars and fields of a PDE.

1 Introduction

Partial differential equations (PDEs) form the mathematical backbone of countless scientific and engineering disciplines, with applications ranging from aircraft design and climate modeling to medical imaging and energy systems. PDE solvers are thus at the core of the overall design, control, or inverse problem solving pipeline for these engineering scenarios. In light of the practical and computational challenges, engineers demand PDE solvers with the following properties:

- *Fast prediction:* Solutions of the PDEs should be generated within limited time and computational resources. This is very important for real-time scenarios like autonomous vehicle control and disaster response, as well as multi-query scenarios that typically arises in solving inverse problems, design optimization, and uncertainty quantification. To accelerate the online solving process, a more expensive offline preparation stage is often allowed.
- *Adequate accuracy:* The prediction error should lie within a reasonable range to make it useful for scientists and engineers. It is also noteworthy that, according to the requirements of downstream tasks, not all applications demand ultra-high precision. For example, engineering design workflows often tolerate small errors in exchange for rapid prototyping. Furthermore, the exact physical mechanisms and material properties may not be completely known in some scenarios, and adopting the approximate versions in PDE modeling would incur errors in parallel with PDE solving.
- *Differentiability:* It should be convenient to compute the derivative of solution with respect to PDE parameters. Downstream tasks such as design and inverse problems typically involve an optimization process. Without the derivative information, engineers have to restrict their choice to gradient-free optimizers that could be relatively inefficient.
- *Versatility:* The solver should be general-purposed, and applies to a wide range of PDEs. Engineering systems increasingly involve coupled physics, requiring simultaneous handling of multiple PDE types. Domain-specific solvers force engineers to deploy and master disparate tools for different equations, creating workflow fragmentation and validation overhead. Exploring new system designs may involve variations

in geometry, boundary conditions, material properties, and governing equations, which demands a unified framework rather than specialized implementations.

Table 1: Comparison of various PDE solvers.

*A few exceptions exist, in which the numerical scheme is implemented using a deep learning framework that supports auto-differentiation.

Solver Type	Fast	Differentiable	Versatile
traditional solvers	✗	✗*	✓
neural operators	✓	✓	✗
PDE foundation models	✓	✓	✓

Traditional numerical solvers, such as finite difference, finite element, and spectral methods, have played a pivotal role in PDE solving over decades of development. These well-established methods are built upon rigorous mathematical foundations, providing reliable solutions that can converge to machine precision—a testament to their reliability and versatility across numerous applications. Their adaptability to diverse problem configurations has made them indispensable tools in both academic research and industrial practice. When considering modern computational demands, however, certain practical constraints emerge. Many real-world applications prioritize computational efficiency over excessive precision, and traditional methods may face challenges in such contexts due to their inherent computational complexity. Compensation techniques like reduced-order modeling [1] have been introduced to improve their online efficiency, but require scenario-specific development, and may encounter accuracy limitations for systems involving convection phenomenon or variable geometries. While gradients can be computed via adjoint methods, their implementation and execution would introduce additional cost, and may hinder seamless integration with differentiable workflows. Moreover, achieving generality may demand careful, problem-specific tuning. Engineers need to rebuild meshes, select appropriate discretization schemes, and adjust solver parameters for new PDEs. This compromises their practical versatility, as adapting these methods to coupled physics or novel equations demands additional expertise and time.

Along with the recent advancements in deep learning, neural operators have emerged as a promising data-driven alternative, learning mappings between function spaces to work as approximate PDE solvers. By predicting the PDE solution via a direct neural network inference, neural operators such as Fourier Neural Operator (FNO)[2] and DeepONet [3] are typically much faster than traditional solvers (often achieving speedups of orders of magnitude), and directly compatible with auto-differentiation as well. This computational efficiency comes at the cost of a lower solution accuracy and reliability, making it currently unsuitable for safety-critical simulations requiring certified precision, but remains acceptable if the target application can tolerate small relative errors. While the data preparation and training procedure consumes resources,

this cost can be justified in the offline stage when the same PDE system requires repeated online evaluations. However, neural operators are not general-purpose solvers. They are designed to solve a specific PDE, and usually require retraining from-scratch for new equation types, boundary conditions, or physical regimes, which are computationally intensive. These specialized models may also require a relatively large number of training samples to achieve desired accuracy, impeding their usage for scenarios in which data generation is very expensive.

The specialized nature of existing neural operators highlights a fundamental challenge in equation-level generalization desired in many scenarios. This mirrors the broader machine learning community’s pursuit of foundation models, which achieve broad task-level adaptability through large-scale pretraining on diverse data, as exemplified by their success in natural language processing and computer vision. Inspired by this paradigm, we focus on the development of a foundation model for solving PDEs—a unified architecture pretrained on diverse PDE families to handle downstream tasks with minimal adaptation. Such a model could inherit the prediction speed and differentiability of neural operators while overcoming their narrow specialization through cross-equation pretraining. In the ideal case, we would expect a foundation PDE model with the following additional properties:

- *Discretization flexibility*: The model can deal with arbitrary discretization instead of being restricted to fixed Cartesian grids. This helps model tackle with different domain shapes, and utilize data generated by different traditional solvers in its pretraining. Furthermore, a mesh-free predicted solution that can be queried at any locations is also desired in many scientific and engineering scenarios.
- *Zero-shot inference*: Pretrained on diverse physical scenarios, the model should be directly applicable to the settings, making predictions without the help of another traditional solver. This would provide a unified solver framework for engineers, without involving additional deployment and computational cost.
- *Efficient adaptation*: For PDEs not encountered in pretraining, the model should allow efficient finetuning to be applied to these settings. Having acquired the shared knowledge across various physical systems, the model is expected to be more efficient than training a specialized neural operator from-scratch, requiring less time and data samples.

Many explorations have been made to develop such a general-purpose foundation model for PDEs. Some approaches attempt to include the symbolic form of the PDE as explicit model input, using textual representations [4–9] or Polish notation of expression trees [10–13]. These methods may face challenges to capture the intricate interplay between the PDE form and the numeric information (coefficient fields, boundary values, etc.) involved, and the generalization to a diverse set of PDEs has not been systematically verified. Other strategies seek to inform model of the underlying PDE in an implicit manner, via either parameter-solution pairs [14–16] or history solution snapshots of time-dependent evolutionary PDEs [17–20]. These methods could be insufficient for PDE classes with greater variety, and have to be accompanied with a traditional solver to prepare additional solution examples. Another line of work only pretrains the model on a (relatively small) collection of PDEs, and requires finetuning

to adapt to any downstream physical systems [21–23]. Zero-shot predictions are not available as well for these methods.

In this work, we introduce PDEformer-2, a foundation model for solving two-dimensional PDEs. Compared with PDEformer-1 [24], our previous exploration for one-dimensional PDEs, we extend the computational graph representation to tackle with the more complicated domain shapes and boundary conditions involved in 2D equations, and employ a much more diverse dataset to pretrain our model. Notable features of our PDEformer-2 model include:

- *Architectural flexibility*: Our model adopt the computational graph representation to encode the symbolic formulation of the PDE, which is flexible and applicable to most common PDEs, laying a good foundation for it to achieve versatility.
- *Versatility after pretraining*: We design and generate a large (40TB) diverse pre-training dataset, and validate that the PDEformer-2 model can simultaneously solve PDEs with different symbolic forms, domain shapes and boundary conditions, number of equations and unknown variables, as well as time-dependency.
- *Mesh-independence*: The predicted solution is represented by an implicit neural representation (INR) that can be directly queried at arbitrary coordinate, without being confined to any fixed set of discretization points.
- *Unified space and time*: The model directly generates solutions on the full spatio-temporal domain, which avoids the time-consuming and error-accumulating autoregressive prediction in its inference, and does not require the inconvenient backpropagation through rollout to compute the derivative.
- *Zero-shot prediction*: By taking the PDE form as explicit model input, the model supports zero-shot inference for specific systems, as long as it is included in the pretraining dataset. We do not need to employ another traditional solver to prepare parameter-solution pairs, history snapshots, or finetuning data samples as some existing foundation models.
- *Efficient adaptation*: When adapted to specific PDEs, PDEformer-2 exhibits better accuracy than specialized models with limited samples, and requires less finetuning time.
- *Downstream task support*: Thanks to the fast inference and differentiable property, our model can be conveniently employed in downstream tasks. This is priliminarily verified on several inverse problems, in which the coefficient scalars and coefficient fields in PDEs need to be recovered.

The paper is organized as follows. Section 2 presents the main experimental results, including model pretraining, solving specific PDEs, and application to inverse problems. We discuss about the results in Section 3, and briefly describe our method in Section 4. Some detailed descriptions are left for the Supplementary Information.

2 Results

We first describe the pretraining dataset for PDEformer-2 and present test set evaluations in Section 2.1. The pretrained model solves specific PDEs via zero-shot inference

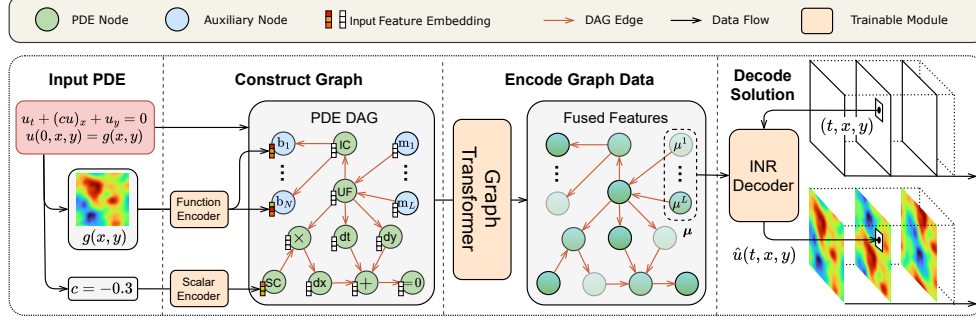


Fig. 1: Overall architecture of PDEformer-2, taking the advection equation $u_t + (cu)_x + u_y = 0$, $u(0, \mathbf{r}) = g(\mathbf{r})$ on $\Omega = [0, 1]^2$ with periodic boundary conditions as an example. This equation involves only a single unknown field variable $u_1 = u$, and we omit the subscript $j = 1$ for u_j and μ_j in the figure.

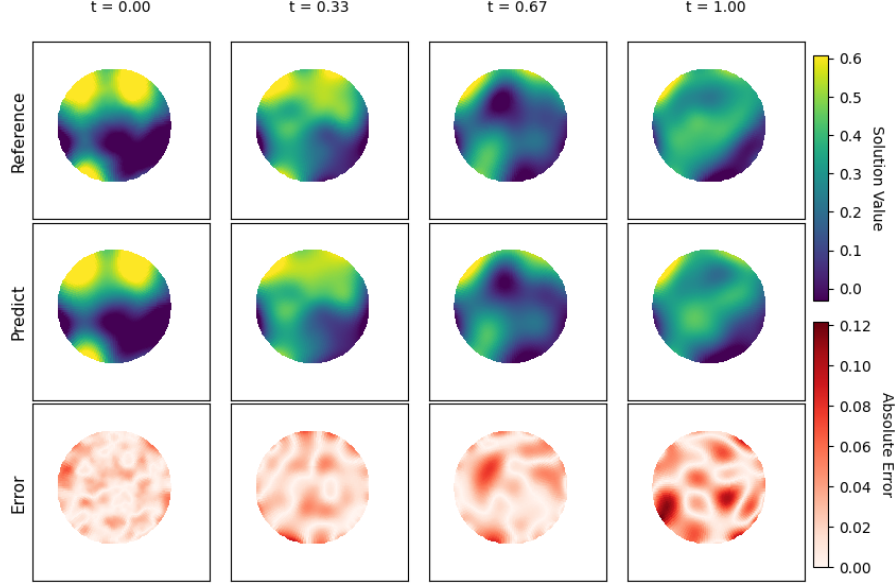
Table 2: Overview of pretraining data size and model normalized root mean square error (nRMSE) on the test set. The dataset we used involve 8 PDE types, each with a corresponding generic PDE form that can yield various specific PDEs via coefficient selection.

PDE Type	Training Samples	Data Size	nRMSE (base)	nRMSE (fast)
DCR	745k	4.85TB	6.9%	8.4%
Wave	605k	4.34TB	6.5%	8.6%
MV-DCR	660k	12.24TB	12.6%	13.5%
DC-DCR	400k	7.49TB	17.0%	19.7%
MV-Wave	320k	6.20TB	5.3%	6.5%
DC-Wave	200k	2.62TB	9.5%	12.2%
G-SWE	100k	1.93TB	13.0%	14.3%
Elasticity	255k	0.38TB	3.8%	3.5%
Total	3.29M	40TB	8.7%	10.3%

or after finetuning (Section 2.2), and is also employed to address inverse problems (Section 2.3).

2.1 Pretraining Results

Dataset Overview. Pretraining a foundation PDE model requires a large diverse dataset, involving many different forms of PDEs. In order to generate random PDEs that constitute our dataset, we first choose a *generic form* of PDE including many terms. Some coefficients in this generic form are then randomly set to be zero or one, which eliminates or simplifies the corresponding terms, leading to a *specific form* of PDE. A total of 8 such generic forms are introduced for improved diversity, including diffusion-convection-reaction (DCR), wave, multi-variable DCR (MV-DCR), divergence-constrained DCR (DC-DCR), MV-Wave, DC-Wave, generalized shallow-water equation



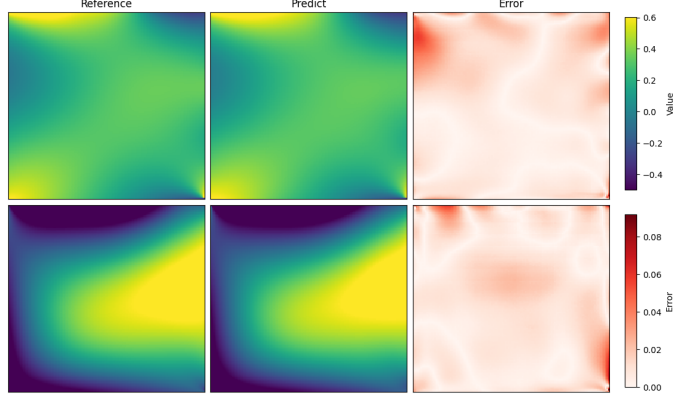
$$\begin{cases} u_{tt} + \mu u_t - a \nabla \cdot (a \nabla u) + s + u + (c_{13} u^3)_x + (u + u^2)_y = 0, \\ (u_t + \alpha u + \gamma(\mathbf{r}))|_{\partial\Omega} = 0. \end{cases}$$

Fig. 2: Test set predictions of PDEformer-2-base after pretraining. The sample corresponds to a nonlinear wave equation on a disk domain Ω , with the specific PDE form shown below visualization.

(G-SWE), and steady-state elasticity equations. Besides various PDE forms, our pretraining dataset also includes different domain shapes, boundary conditions (BCs), number of unknown variables¹, and time-dependency. We prepare this dataset using traditional numerical solvers, including Dedalus V3 [25] based on spectral method and FEniCSx [26] based on finite-element method. A brief summary of the dataset is shown in Table 2, and readers may refer to Supplementary Information C.1 for a detailed description. It is noteworthy that this dataset, in which different samples correspond to different PDE forms, is not suitable for training common neural operators that are designed only for a specific PDE.

Test Set Predictions. We pretrained two models, *PDEformer-2-base* and *PDEformer-2-fast*. The hyperparameters of PDEformer-2-base is selected mainly according to our previous experience on one-dimensional model, PDEformer-1 [24]. This model exhibits relatively long inference time when queried at a lot of spatio-temporal points, which is the common case to make a full space-time prediction for

¹Some PDEs involve multiple interacting variables, and they need to be solved simultaneously, constituting of different components of the complete solution. The terms “variables” and “solution components” will be used interchangeably in this work.



$$\begin{cases} (\lambda(\mathbf{r})(u_x + v_y) + \mu_2(\mathbf{r})u_x)_x + (\frac{1}{2}\mu_2(\mathbf{r})(u_y + v_x))_y + f_1(\mathbf{r}) = 0, \\ (\frac{1}{2}\mu_2(\mathbf{r})(u_y + v_x))_x + (\lambda(\mathbf{r})(u_x + v_y) + \mu_2(\mathbf{r})v_y)_y + f_2(\mathbf{r}) = 0, \\ (\partial_n u + \beta_L)|_L = 0, \quad (u + \beta_R(\mathbf{r}))|_R = 0, \quad (u + \beta_D)|_D = 0, \quad (u + \beta_U(\mathbf{r}))|_U = 0, \\ v|_L = 0, \quad (\partial_n v)|_R = 0, \quad v|_D = 0, \quad (v + \beta_U(\mathbf{r}))|_U = 0. \end{cases}$$

Fig. 3: Test set predictions of PDEformer-2-base. The sample corresponds to a steady-state elasticity equation, with the two variables u, v shown in separate rows. Boundary conditions at the left (L), right (R), top (up, U), and bottom (down, D) edges are specified separately.

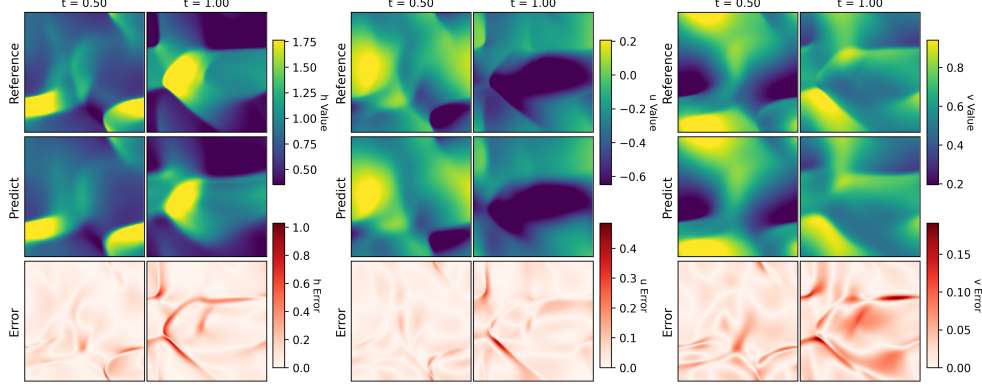
two-dimensional PDEs. PDEformer-2-fast is designed to be relatively more efficient in this aspect (see Table 3 for the comparison), despite a slight sacrifice of accuracy as shown in Table 2.

Figure 2, 3, and 4 visualize the predictions of PDEformer-2-base on test datasets, selecting three cases² as examples. We note that these cases differ in PDE forms, domain shapes, boundary conditions, number of variables, as well as time-dependency, illustrating the flexibility of our pretrained PDEformer-2 model.

Extrapolating to PDEs with More Variables. While the common expectation for foundation PDE models is to generalize within the pretraining distribution³, many practical scenarios also require to handle out-of-distribution cases, which presents a more challenging but valuable capability. Here we investigate this aspect by examining the model performance on PDEs with varying numbers of interacting variables, particularly focusing on its extrapolation ability beyond the pretraining distribution. The pretraining dataset contains multi-variable PDEs with at most four such variables.

²As the specific PDE forms are randomly generated as explained above, they may not possess a clear physical interpretation.

³For readers without machine learning background: Data instances in the pretraining dataset can be viewed as samples from a certain probability distribution. Being “in-distribution” of a new PDE instance means that it can be drawn from this distribution with a reasonable likelihood, and the features are similar to the existing pretraining data. Conversely, “out-of-distribution” PDEs has patterns that were not encountered during the pretraining stage, and requires extrapolation for the model.



$$\begin{cases} h_t + ((h + H(\mathbf{r}))u)_x + ((h + H(\mathbf{r}))v)_y - \nabla \cdot (a_0 \nabla h) + u + v + b_{022}v^2 = 0, \\ u_t + uu_x + vv_y + G_1 h_x - \nabla \cdot (a_1 \nabla u) + s_1 + c_{10}h + hv = 0 \\ v_t + uv_x + vv_y + G_2 h_y - a_2 \Delta v + c_{23}v = 0 \end{cases}$$

Fig. 4: Test set predictions of PDEformer-2-base, showing snapshots of a generalized shallow-water equation with periodic boundary conditions. Shock-like patterns can be observed in the figure.

When tested on PDEs with five variables, PDEformer-2 demonstrates reasonable zero-shot prediction accuracy as shown in Figure 5, suggesting some degree of extrapolation capability.

We note that, in addition to the variable number, other types of extrapolation may also be of interest in real applications, including new PDE forms as well as coefficient fields coming from a new distribution. The corresponding model performance will be examined in Section 2.2, in which few-shot adaptation is allowed besides direct zero-shot predictions.

Robustness against Non-Physical Patterns. A small number of non-physical solutions appear in the pretraining dataset due to the limitation of Dedalus solver⁴. To assess the robustness of PDEformer-2 against numerical errors and artifacts, we regenerate reference solutions of several DCR PDEs using the FEniCSx solver, and compare them with the predictions made by Dedalus and PDEformer-2-base. As illustrated in Figure 6, a representative case demonstrates non-physical oscillations in the Dedalus solution, which do not present in the FEniCSx solution and the PDEformer-2 prediction. This should not be deemed as an isolated case, as indicated by the scatter plot shown in Figure 23 in the Supplementary Information. We infer from the results that PDEformer-2 is not misled by the “incorrect” samples in the pretraining data,

⁴Traditional solvers often require problem-specific tuning. A careful case-by-case selection of the solver parameters may eliminate these non-physical patterns, but is intractable in our data generation since the randomly sampled PDEs differ a lot from each other. This also applies to the failure cases mentioned in the following text.

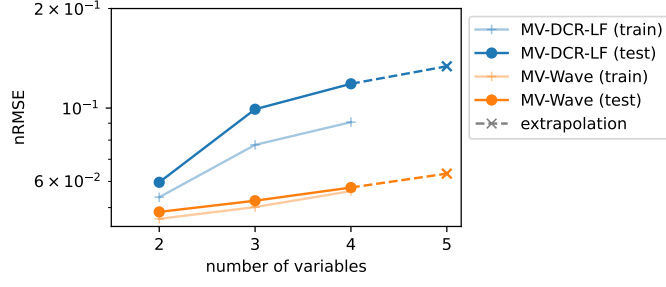
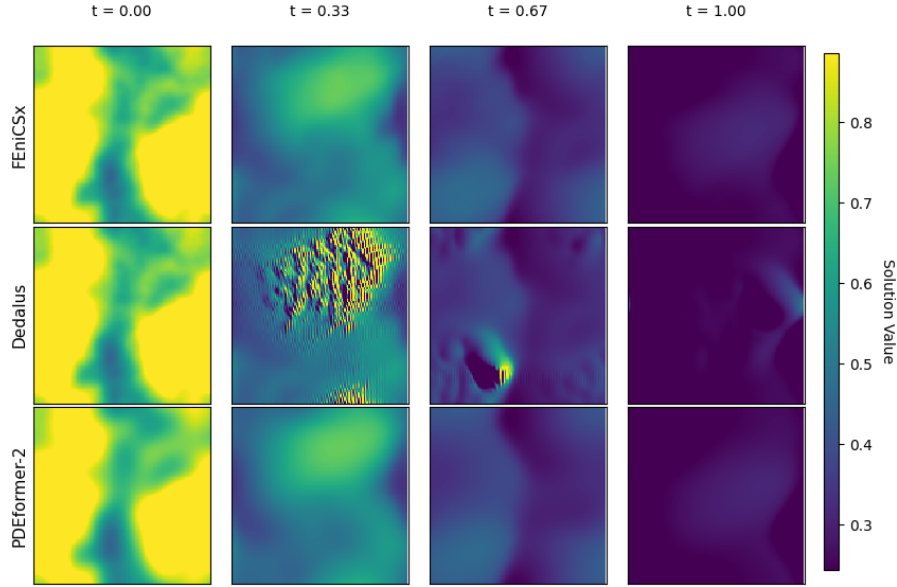
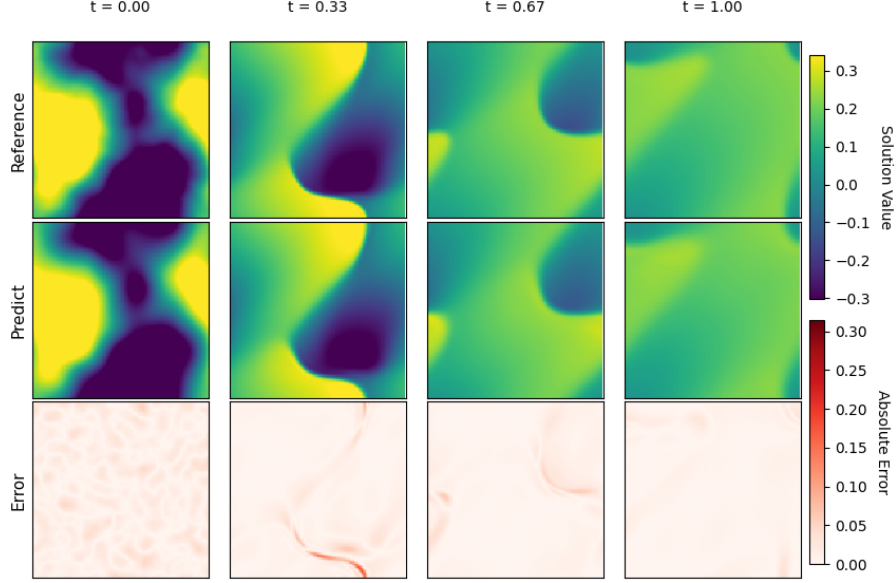


Fig. 5: Accuracy of PDEformer-2-base under different numbers of PDE variables. The datasets include MV-DCR equations with linear fluxes (LF) as well as MV-Wave equations. Although the pretraining datasets involves no more than four unknown variables, PDEformer-2 can make reasonable zero-shot extrapolation to PDEs with five variables.



$$u_t - a \nabla \cdot (a \nabla u) + u + u^3 + (u + c_{12}u^2 + c_{13}u^3)_x + (u + c_{22}u^2)_y = 0$$

Fig. 6: Comparison of the FEniCSx solution (top), the Dedalus solution (middle), and the PDEformer-2 prediction (bottom). The Dedalus solution exhibits non-physical oscillations, while the PDEformer-2 prediction aligns well with the FEniCSx solution.



$$u_t - a\Delta u + s + u + u^2 + c_{03}u^3 + (c_{11}u + u^2 + u^3)_x + (u + u^2)_y = 0$$

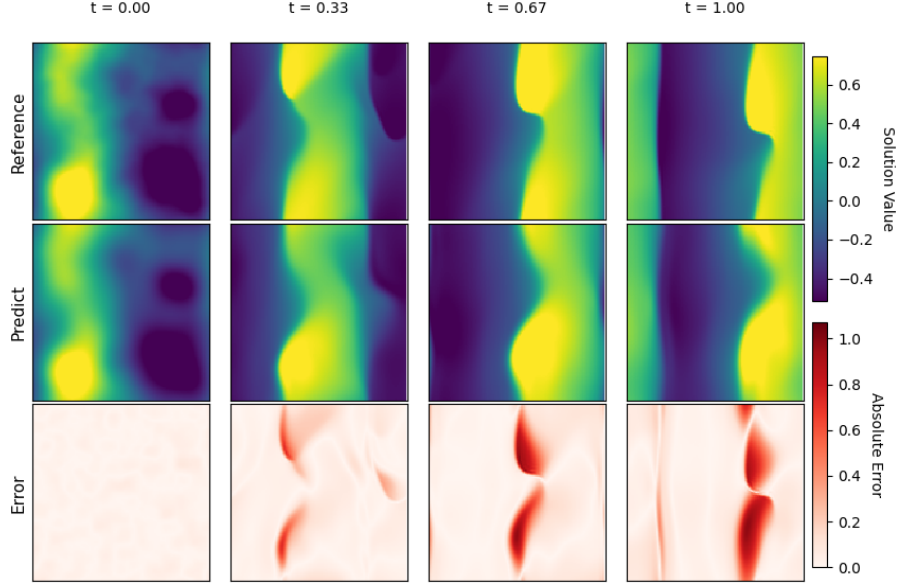
Fig. 7: Prediction of PDEformer-2-base on a case that Dedalus fails. We employ FEniCSx to prepare the reference solution. Note that this is a selected successful example rather than a representative case.

and can make reasonable predictions according to the other “correct” samples it has seen. The model outperforms its teacher solver in this specific sense.

Performance on Failure Cases of the Teacher Solver. In addition to producing non-physical patterns, Dedalus may also fail to solve some PDEs, terminating with NaN values. PDEformer-2 learns to solve DCR equations only from the samples that Dedalus successfully generates, and we examine its predictions on those failure cases after pretraining. Taking FEniCSx solutions for reference again, PDEformer-2-base can make reasonable predictions in some cases, with an example shown in Figure 7. However, the superiority over the teacher solver is relatively limited in this setting, as the accuracy is in fact unsatisfactory in most cases (see Figure 24 in the Supplementary Information). Figure 8 illustrates a representative example.

2.2 Adaptation to Specific PDEs

This subsection focuses on the forward problems, in which we need to predict the solutions of some specific PDEs. The baseline models involve several specialized neural operators, which are trained from-scratch and tested separately on different datasets. These include two DeepONet [3] variants with different branch network architectures, U-Net [27] and FNO [2] designed for Cartesian grids, and Geo-FNO [28]



$$u_t - a \nabla \cdot (a \nabla u) + s(r) + c_{01}u + c_{02}u^2 + u^3 + (c_{11}u + c_{12}u^2 + c_{13}u^3)_x + (u^2 + c_{23}u^3)_y = 0$$

Fig. 8: Prediction of PDEformer-2-base when Dedalus fails, showing a representative case. We employ FEniCSx to prepare the reference solution. While our model successfully captures the overall physical phenomena, its imperfect handling of shock evolution leads to observable prediction errors."

applicable to non-Cartesian grids. We let these models predict the full space-time solution like PDEformer-2, which avoids error accumulation of the autoregressive models. The time axis can be treated either as extended channels (marked as 2D) or an additional spatial axis (marked as 3D). In addition to these specialized models, we also introduce two existing PDE foundation models using Cartesian grids, including MPP [17] that executes rollout predictions, and Poseidon [23] that predicts each time step independently. Details of the models and datasets can be found in Supplementary Information A.3 and C.2.

Zero-Shot Predictions and Few-Shot Adaptation

PDEformer-2 can make accurate predictions directly if the target PDE lies in the distribution of the pretraining dataset. The zero-shot accuracy may not be satisfactory for out-of-distribution PDEs, and we need to finetune our model. Intuitively, with the good initialization containing prior knowledge from pretraining, PDEformer-2 has the potential of outperforming specialized models that are trained from-scratch, especially when the number of accessible training samples is limited. If the target PDE is similar to those in the pretraining dataset, we would expect more efficient knowledge transfer,

and PDEformer-2 could exhibit significant superiority. The advantage may be less obvious in the opposite case.

Such intuition is validated through experiments, involving three customized datasets and two publicly available datasets. We finetune pretrained PDE foundation models, or train specialized neural operator models from-scratch, for a maximum of one thousand epochs, with potential early-stopping to mitigate overfitting. Accuracy (measured as nRMSE) on the test set is recorded, and we shall study how it varies with the number of training samples for different models and datasets.

The *Sine-Gordon* equation dataset lies in the pretraining data distribution. From Figure 9a, we can see that the two PDEformer-2 models already achieves high accuracy without any adaptation, outperforming all the baseline models trained specifically on this dataset. Further finetuning of PDEformer-2 does not lead to a significant improvement in performance, at least for the training sizes examined in our experiments.

The *INS-Tracer* dataset exhibits a slight distribution shift from the pretraining data, featuring a new combination of physical laws. The complete PDE form is not included in pretraining, but the constituting physical mechanisms, including incompressible Navier-Stokes (INS) equation and the interaction between variables (fluid velocity and tracer particle density in our setting), have appeared in different pretraining datasets. From Figure 9b, we see the zero-shot prediction accuracy of PDEformer-2 is inferior to that of the in-distribution Sine-Gordon dataset, but still in a reasonable range. Finetuning appears fruitless with limited samples, and improves model performance gradually as the data size increases. The baseline models seem to improve faster with more training data. FNOs finally surpasses PDEformer-2 using sufficiently many data samples, while Poseidon achieves this with only 80 such samples. We conjecture that Poseidon also benefits a lot from its prior knowledge, as it is pretrained on fluid-type datasets that resembles the current equation.

The *INS-Pipe* dataset also slightly deviates from the pretraining distribution. All multi-variable PDEs in the pretraining data, including DC-DCR that covers the INS equation, are periodic along both axes. No-slip boundaries at the top and bottom edges indeed exist, but only come with single-variable equations. According to Figure 9c, PDEformer-2 cannot make satisfactory zero-shot predictions. However, with the prior knowledge from pretraining, the models learn efficiently from the finetuning samples, and maintain superiority for all data sizes examined.

The *Wave-Gauss* dataset from PDEGYM [23] would require a relatively far transfer from pretraining. The initial conditions and wave velocity fields are generated as a summation of Gaussian modes, which is different from the Gaussian random fields (GRFs) in the pretraining data. Moreover, all evolutionary equations on square domains in pretraining are periodic in at least one axis, but Wave-Gauss absorbs waves in its four edges. As shown in Figure 9d, PDEformer-2 exhibits marginal advantage over the other models in the low-data regime, and loses its lead with more training samples.

The *Wave-C-Sines* dataset released by Mousavi et al. [29] considers the wave equation on a disk-shaped domain. Thanks to the mesh-free nature of the INR decoder, PDEformer-2 can be utilized to predict the solutions discretized on irregular mesh points. However, the performance does not seem satisfactory, especially when compared with the Geo-FNO model. Indeed, the data distribution deviates from the pretraining

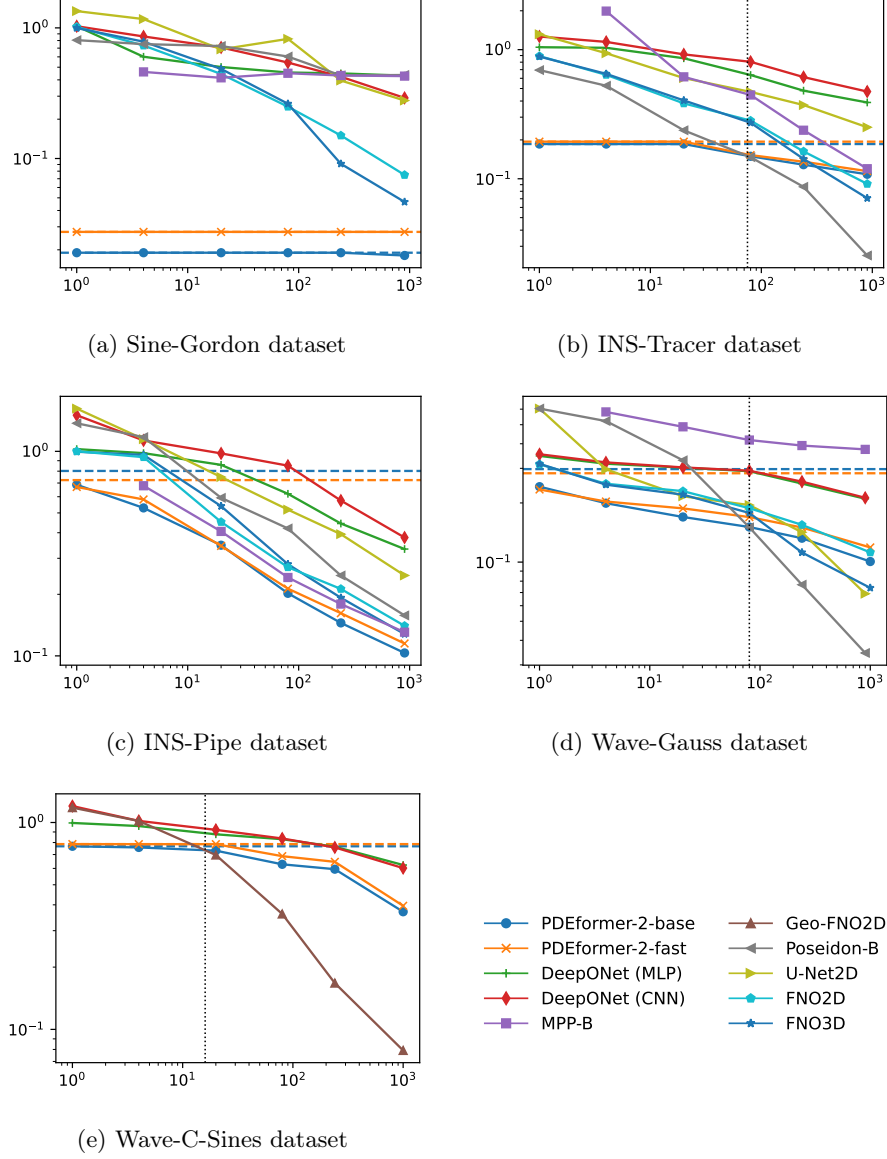


Fig. 9: Variation of solution accuracy with data size for different models, with the horizontal axis representing the data size used in training (finetuning) and the vertical axis representing the nRMSE on the test set. The horizontal dashed lines represent zero-shot predictions of PDEformer-2, and the vertical dotted lines mark the data size at which PDEformer-2 no longer prevails. Note that most of the baseline models are designed for Cartesian grids, and cannot be directly applied to the Wave-C-Sines dataset discretized on scatter points inside the disk domain, unless we interpolate the PDE solutions.

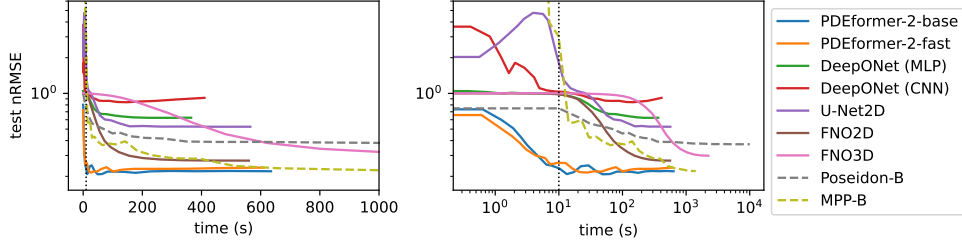


Fig. 10: Training or finetuning speed of different models, running for one thousand epochs with 80 INS-Pipe data samples. Poseidon-B and MPP-B run on a different software and hardware platform, and their time consumptions are not directly comparable to the others. We thus deliver the results using dashed lines.

dataset, with the initial condition taken as a superposition of sinusoidal modes, whose frequency is much higher than the pretraining GRFs. Some other factors may also contribute to the results, including the architectural capabilities of processing high-frequency input, and the insufficient amount of non-square domain data in pretraining. More detailed investigation could be useful to identify the causes, and is left for future work.

Adaptation Speed

In addition to the data size, model prior knowledge can also reduce the computational resources required during adaptation. Figure 10 illustrates the training or finetuning process of different models, in which 80 samples from the INS-Pipe dataset is used. The PDEformer-2 models converge in merely ten seconds, while others are more than a magnitude slower.

Prediction Speed

A fast solver is demanded for scenarios that require real-time or repeated querying of PDE solutions. While the mesh-free design of PDEformer-2 sacrifices some inference speed compared with grid-based alternatives, it gains the capability to tackle with irregular discretization and domain shapes, which is also desired in many applications. Further sacrifice originates from the network size required for concurrently learning a variety of PDEs. Despite of these, our model remains faster than traditional methods. Table 3 compares the prediction time of various neural solvers, as well as Dedalus⁵, the traditional numerical solver based on spectral methods that we employ to generate the datasets. The comparison evaluates the number of parameters, per-sample prediction time, and solution accuracy (measured as nRMSE) across the Sine-Gordon and the INS-Pipe datasets. We note that the solutions may be used in different ways in different downstream applications. Some tasks require a full space-time prediction (Full), with

⁵When we reduce the grid resolution for Dedalus, the error is computed against the resolution 128 results in consistency with the neural solvers. If we use solutions with a higher resolution for training and testing, we speculate that the computed errors would become larger for low-resolution traditional solvers, and do not change significantly for neural solvers.

Table 3: Comparison of the number of trainable parameters and per-sample inference time of different solvers. Neural network models are tested on a single NPU by default with batch size 1 and Dedalus is executed on a CPU. The base and fast variants of PDEformer-2 share the same model size in the Encoder-Only setting, and we merge the results.

*The results are tested on a single GPU with a different software platform, hence not directly comparable with the other network models.

Model	Sine-Gordon			INS-Pipe		
	Param.	Time (s)	Error	Param.	Time (s)	Error
Full						
DeepONet (CNN)	2.56M	0.085	0.291	3.09M	0.136	0.379
DeepONet (MLP)	3.68M	0.086	0.431	6.30M	0.138	0.333
FNO2D	0.94M	0.015	0.075	0.95M	0.014	0.140
FNO3D	22.12M	0.062	0.047	22.12M	0.062	0.128
U-Net2D	13.40M	0.013	0.278	13.41M	0.012	0.247
PDEformer-2-base	82.65M	0.631	0.018	82.65M	1.262	0.103
PDEformer-2-fast	71.07M	0.202	0.027	71.07M	0.406	0.115
MPP-B	115.6M	5.612*	0.427	115.6M	4.666*	0.131
Poseidon-B	158M	15.60*	0.436	158M	11.79*	0.158
Last Timestep						
DeepONet (MLP)	3.68M	0.005	—	6.30M	0.006	—
PDEformer-2-base	82.65M	0.033	—	82.65M	0.052	—
PDEformer-2-fast	71.07M	0.033	—	71.07M	0.050	—
Poseidon-B	158M	0.126*	—	158M	0.124*	—
INR as Output						
PDEformer-2	—	0.020	—	—	0.022	—
Reference						
Dedalus	—	2.398	—	—	24.300	—
Dedalus (resolution 64)	—	0.936	0.029	—	10.131	0.026
Dedalus (resolution 32)	—	0.436	0.085	—	5.222	0.079
Dedalus (resolution 16)	—	0.207	0.197	—	2.569	0.216
Dedalus (resolution 8)	—	0.092	0.396	—	1.058	0.459

resolution $128^2 \times 101$ in our setting. Others may show interest mainly in the final state (Last Timestep). Sometimes we only need to make queries at a very limited number of spatio-temporal locations—such as the inverse problem observations—and the majority of the prediction time can be attributed to preparing an implicit neural representation for the solution (INR as Output). We thus distinguish the three prediction times if they are valid and differ from the others for each model. Prediction errors are recorded only for the Full predictions.

Dealing with Imperfect PDE Specifications

In some real scientific and engineering scenarios, the underlying physical mechanisms may not be completely clear to us. PDEformer-2 requires taking the explicit PDE form as network input (unlike conventional neural operators), and is expected to maintain adaptability to deal with such imperfect specifications while still leveraging available physical knowledge. We conduct an ablation study to evaluate the model performance in such scenarios. In the regular case, the INS-Tracer equation is formulated in

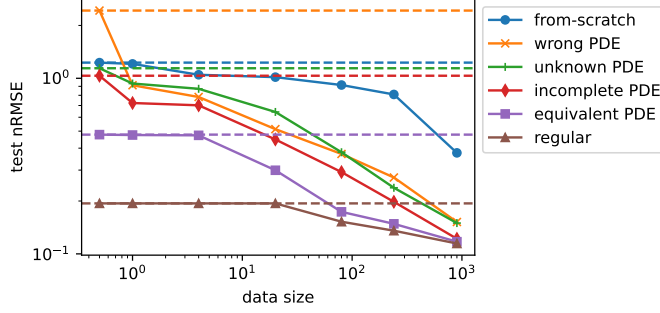


Fig. 11: Ablation study of PDEformer-2-fast adaptation performance on the INS-Tracer dataset, in which the model takes different PDE forms as input, or is trained from-scratch. Horizontal dashed lines along with the endpoints on the left represent zero-shot predictions.

conservation form to better match the pretraining data. We introduce a series of new cases with decreasing quality of the PDE input, generated by (1) switching to the convection form (equivalent PDE), (2) removing the viscosity, pressure, and the divergence-free condition (incomplete PDE), (3) marking the PDE as completely unknown as explained in Supplementary Information B.2 (unknown PDE), and (4) taking the Lorenz ODE system as model input (wrong PDE). As can be seen in Figure 11, the zero-shot prediction accuracies deteriorate accordingly. However, this can be compensated by utilizing more training data, as the model preserves the capability of adaptation. The differences narrow as the data size increases, and nearly vanish with sufficiently many finetuning samples.

In addition to the PDE input, we also investigate the case in which the model is trained from-scratch. Without the good initialization, the model struggles to learn from data even with the “correct” PDE as input, highlighting the importance of prior knowledge obtained from pretraining. We note that when scientists want to make predictions of systems with incomplete physical knowledge, they may need to combine information of the known part of physics, scarce observed data, and previous knowledge about other systems. PDEformer-2 has primarily demonstrated such capability, as the results with incomplete PDE possess improvement over that of unknown PDE, zero-shot incomplete PDE, and from-scratch, respectively.

2.3 Application to Inverse Problems

To demonstrate the applicability of our pretrained model to downstream tasks, we conduct experiments on inverse problems as a case study, with PDEformer-2-base serving as the surrogate solver. The tasks involve recovering unknown scalar coefficients or source fields in DCR equations, as well as velocity fields in Wave equations. In these scenarios, multiple solutions of a PDE are obtained with different initial conditions. Instead of providing the exact complete solution fields, we only assume access to the noisy observations at a limited number of spatio-temporal points, and the available

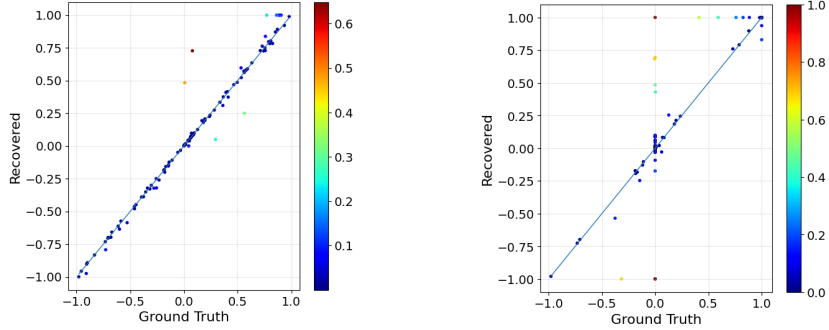
initial conditions also include noise. The input to PDEformer-2 includes the equation form, noisy initial conditions, and the current estimation of coefficient scalars or fields. We compare the predicted solutions against observations to compute the nRMSE, and solve an optimization problem to obtain the best estimation.

Recovering Scalar Coefficients

In this study, we assume the form of the PDEs are known, and aim to recover the unknown coefficient values in each equation using noisy observations taken at random spatio-temporal locations. The PDEs are generated as the pretraining DCR dataset. For instance, if the PDE takes the form

$$u_t - a\Delta u + s(\mathbf{r}) + c_{01}u + c_{02}u^2 + c_{03}u^3 + (c_{12}u^2 + u^3)_x + (u + c_{23}u^3)_y = 0, \quad (1)$$

we shall recover the scalar coefficients $a, c_{01}, c_{02}, c_{03}, c_{12}, c_{23}$ based on observations and known initial conditions. For each PDE, we have access to solutions under 25 different initial conditions. Observable data points are restricted to 128 random spatial locations, and the accessible timesteps at these locations are randomly selected, with an average of 20 observations per spatial point. Observational data includes 1% noise, and initial values serving as the model input also include 1% additive noise. Since the loss function contains a lot of local minima, we use the Particle Swarm Optimization (PSO) algorithm [30] to address the optimization problem. Figure 12a compares the recovered coefficients with their ground-truth values for 40 PDEs, showing that most coefficients are successfully recovered. Note that the number of coefficients to be recovered varies for different PDEs (ranging from 1 to 10), and the number of points displayed in the figure exceeds the number of PDEs.



(a) Results of scalar coefficient recovery.

(b) Results of system identification.

Fig. 12: Results for scalar coefficients recovery and system identification. Each coefficient is depicted as a point in the figure, with the x -axis representing the ground-truth value and y -axis the recovered value. The recovery is considered successful when the points are closely aligned with the diagonal line $y = x$.

We also perform experiments with varying noise levels, number of spatio-temporal locations, and number of initial conditions for the recovery. The results are presented in Supplementary Information [D.3.1](#).

System Identification

System identification is a structured approach used in control engineering and signal processing to develop mathematical models of dynamic systems by analyzing observed data. By assuming knowledge about the complete set of all possible terms that may appear in the PDE, the system identification task can be treated as a particular instance of coefficient recovery, and we need to identify which coefficients in the complete PDE are zero. In our experiment, the complete PDE takes the form

$$\begin{aligned} u_t - a\Delta u + s(\mathbf{r}) + c_{01}u + c_{02}u^2 + c_{03}u^3 \\ + (c_{11}u + c_{12}u^2 + c_{13}u^3)_x \\ + (c_{21}u + c_{22}u^2 + c_{23}u^3)_y = 0, \end{aligned}$$

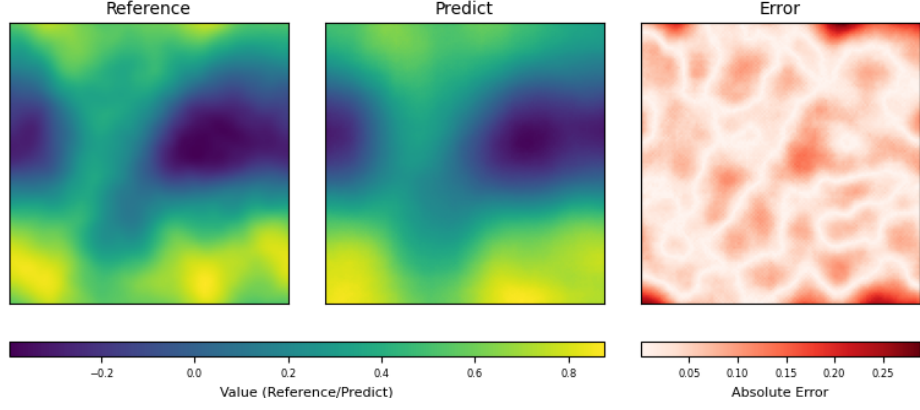
and we recover the coefficients a, c_{ij} for $i \in \{0, 1, 2\}, j \in \{1, 2, 3\}$ to determine the dynamic system behind the measured data. We assume that solutions can be obtained under 25 different initial conditions, with observable samples limited to 128 spatial locations and an average of 20 observation samples per location. Noise is added with a relative amplitude of 1% to the observed values and 1% to the initial values used as inputs for PDEformer-2. The system identification is performed on ten DCR cases, and Figure [12b](#) presents the outcomes. Although we do not impose constraints or penalties to encourage sparsity of the recovered coefficients, most of the zero coefficients are approximately identified, with only 6 out of the 29 recovered values have an absolute value that exceeds 0.1. Detailed results are presented in Table [6](#) in the Supplementary Information.

Recovering Source Fields

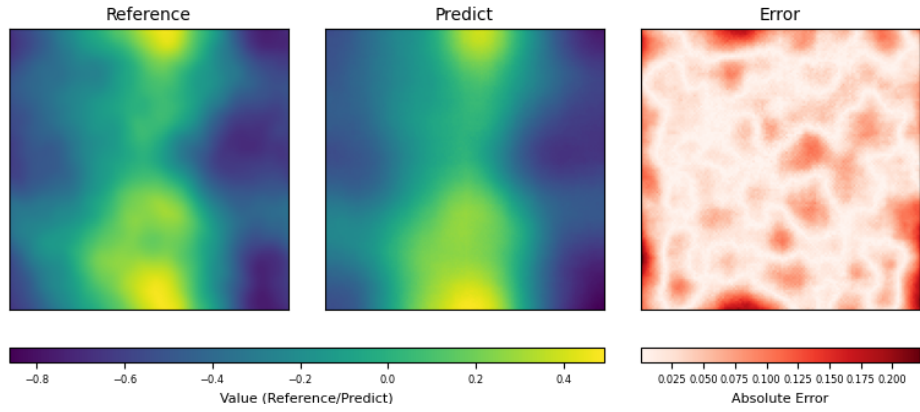
In this study, we still consider the DCR equations ((1) is still a valid instance), but the current goal is to recover the coefficient field $s(\mathbf{r})$ that serves as the source term. For each PDE, we assume 25 solutions under different initial conditions are available, with observable sample points constrained to 128 random spatial locations, each having an average of 20 observation samples. Observational data at these points include noise with a relative amplitude of 1%, while the initial values are subject to 1% noise. We denote the forward operator mapping sources to PDE solutions as \mathcal{F} (with PDEformer-2-base backbone), the subset of observed spatio-temporal locations as S^{obs} , and the observed solution values as u_{obs} . The Adam optimizer [\[31\]](#) is employed to solve the optimization problem formulated as

$$\arg \min_s \mathcal{L}(s) = \left\| u_{\text{obs}} - \mathcal{F}(s)|_{S^{\text{obs}}} \right\|_2^2 + \lambda \mathcal{R}(s), \quad (2)$$

where \mathcal{R} represents certain regularization against over-oscillatory patterns. Details of regularization and hyperparameters can be found in Supplementary Information [D.3.3](#).



$$u_t - a\Delta u + s(\mathbf{r}) + u + (c_{11}u + c_{13}u^3)_x + (u + c_{22}u^2)_y = 0$$



$$u_t - a\nabla \cdot (a\nabla u) + s(\mathbf{r}) + u + c_{02}u^2 + c_{03}u^3 + (c_{12}u^2 + u^3)_x + (c_{21}u + u^2)_y = 0$$

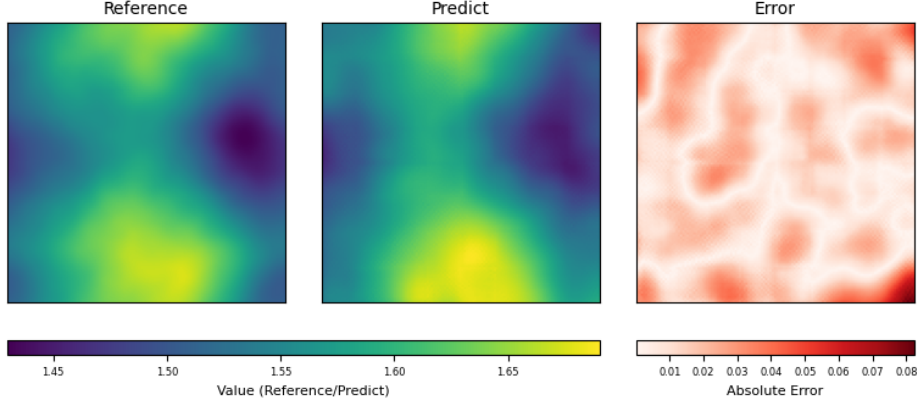
Fig. 13: Two recovered source fields, with the corresponding PDEs shown below the results. Ground-truth, recovery and error are plotted from left to right.

We perform experiments on 40 different source fields and achieve an average nRMSE of 0.159 for the recovered source fields. Two examples are shown in Figure 13.

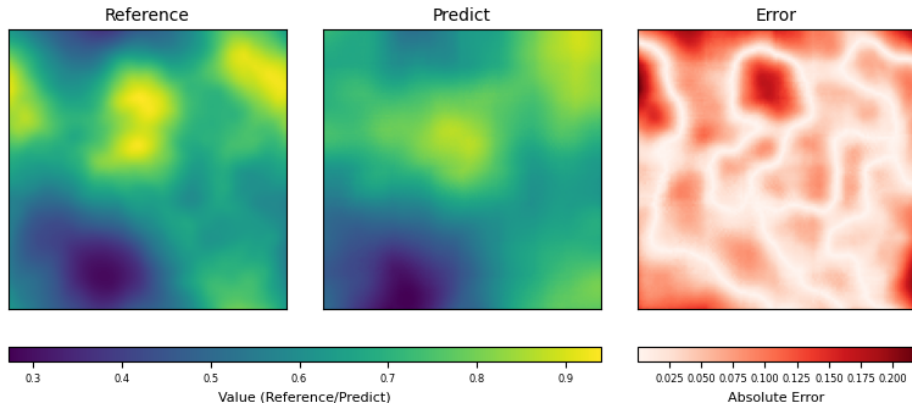
Recovering Wave Velocity Fields

This is a simplified version of full waveform inversion in geophysics, in which the velocity field $c(\mathbf{r})$ or its square $a(\mathbf{r}) = c(\mathbf{r})^2$ needs to be estimated according to observed wave propagation. The PDEs are generated as the pretraining Wave dataset with inhomogeneous (i.e., non-constant) velocities. For instance, if the PDE takes the form

$$u_{tt} + \mu(\mathbf{r})u_t - \nabla \cdot (a(\mathbf{r})\nabla u) + s(\mathbf{r}) + c_{02}u^2 + (u + u^2)_x + (c_{21}u + u^3)_y = 0,$$



$$u_{tt} - c(\mathbf{r})\nabla \cdot (c(\mathbf{r})\nabla u) + s(\mathbf{r}) + c_{03}u^3 + (c_{11}u + c_{13}u^3)_x + (c_{22}u^2)_y = 0$$



$$u_{tt} + \mu(\mathbf{r})u_t - \nabla \cdot (a(\mathbf{r})\nabla u) + s(\mathbf{r}) + c_{01}u + c_{02}u^2 + c_{03}u^3 + (u + c_{12}u^2 + u^3)_x + (u + c_{23}u^3)_y = 0$$

Fig. 14: Recovered velocity field $c(\mathbf{r})$ (first example) or its square $a(\mathbf{r}) = c(\mathbf{r})^2$ (second example), with the corresponding PDEs shown below the recovered results. Ground-truth, recovery and error are plotted from left to right.

we shall recover $a(\mathbf{r})$ based on observations and known initial conditions. For each $c(\mathbf{r})$ or $a(\mathbf{r})$ to be reconstructed, we assume that solutions are available for 100 different sets of initial conditions $u(0, \mathbf{r})$, $u_t(0, \mathbf{r})$ and source fields $s(\mathbf{r})$, with observable sample points constrained to 128 random spatial locations, each having an average of 20 observation samples. Observational data at these points include noise with a relative amplitude of 1%, and the initial values are subject to 1% noise. The optimization problem is similar to (2). Due to the existence of local minima, we solve each optimization problem by applying Adam for multiple times with different initial guesses, and the details

are explained in Supplementary Information C.3.2 and D.3.4. Figure 14 shows two examples of the reconstructed results.

3 Discussion

In this paper, we introduce PDEformer-2, a foundation model for 2D PDEs. The flexible model architecture takes both the symbolic expression and the numerical information (initial conditions, coefficient values, etc.) of PDEs as input, making it applicable to a wide range of PDEs. Its outputs (i.e., predicted PDE solutions) are not restricted to any fixed set of discrete grid points. After pretraining on a large diverse dataset, PDEformer-2 demonstrates capability of simultaneously addressing PDEs with different symbolic forms, domain shapes, boundary conditions, number of equations and unknown variables, as well as time-dependency.

We note that PDEformer-2 may have developed preliminary understanding of the PDE structure, since it can make reasonable zero-shot predictions on PDEs unseen during pretraining, which have more unknown variables (Figure 5) or involve a new combination of known physical mechanisms (Figure 9b). Artifacts in the dataset generated by the traditional solver are not inherited by the pretrained model (Figure 6). Indeed, such generalizable understanding is still limited, as the model does not perform well when the PDE deviates further from the pretraining data (e.g., zero-shot results of Figure 9e), or cannot be tackled by the traditional solver employed in data preparation (Figure 8). We therefore suggest that future foundation models should be pretrained on datasets synthesized from multiple traditional solvers, rather than relying on generalization from a single solver. Different traditional solvers are adept at solving different types of PDEs, and a foundation model can integrate the capabilities of these solvers, eliminating the hassle of solver switching and parameter tuning for engineers. As our current PDEformer-2 has primarily demonstrated generalization across various PDEs, it could seem promising to develop such a model in the future.

In terms of downstream task support, PDEformer-2 can be applied to both forward and inverse problems. For PDEs that are different from the pretraining ones, PDEformer-2 can adapt quickly to learn to solve these equations. Compared with other baseline specialized models, PDEformer-2 achieves better accuracy when the number of training data is small, indicating that it is a competitive candidate for real-world applications where data availability is limited. Additionally, PDEformer-2 can serve as a surrogate model for various inverse problems, including coefficient recovery, system identification, source field inversion, and full waveform inversion.

Although PDEformer-2 demonstrates advantages in the experiments, it still falls short of some ideal properties discussed in Section 1 in several aspects, requiring further improvements in the future. First, as shown in Table 3, the prediction speed for the full space-time solution is inferior to some baseline models, which can be partly attributed to the mesh-free design for better flexibility, as well as the model capacity required for concurrently learning a variety of PDEs. This can be potentially remedied by utilizing more efficient INR architectures, and distilling the knowledge into a smaller model that supports faster inference. Second, the solution accuracy may not meet the requirements of some real applications, and does not outperform

baseline models given sufficient data on some dataset tested in Section 2.2. To achieve better scaling properties of the model, it could be beneficial to design a more diverse pretraining dataset, adopt more advanced architectures that are suitable for high-frequency and multi-scale physical fields, and explore more finetuning strategies to enable sustainable improvements. Third, the solution capability is still limited. Future advancements may include supporting PDEs with more complicated domain shapes, time-dependent coefficients and domains, integro-differential equations, and so on. Extension to three-dimensional PDEs could be a challenging task that requires further research. Furthermore, the capabilities of PDEformer-2 has not been validated on real-world data and tasks. Application to more downstream scenarios like design and control is also left for future work.

4 Method

Problem Settings

We hope to develop a foundation surrogate model for solving two-dimensional PDEs with the highest generality, capable of handling any such PDE in the ideal case. The input of such a model includes the conditions for a definite solution, which may involve the symbolic formulation of the PDE and boundary conditions (BCs), the computational domain shape, the coefficient scalars or fields, the initial values, etc. The output of the model would be the complete solution of the PDE, which can be queried at any spatio-temporal point. Note that the number of equations, BCs, coefficients, and solution components may differ across PDEs, without a pre-selected upper bound.

Specifically, we consider two-dimensional PDEs defined on $(t, \mathbf{r}) \in [0, 1] \times \Omega$ of the general form

$$\begin{aligned}\mathcal{F}(u_1, u_2, \dots, c_1, c_2, \dots, s_1(\mathbf{r}), s_2(\mathbf{r}), \dots) &= 0 \quad \text{in } \Omega, \\ \mathcal{B}_i(u_1, u_2, \dots, c_{i1}, c_{i2}, \dots, s_{i1}(\mathbf{r}), s_{i2}(\mathbf{r}), \dots) &= 0 \quad \text{on } \Gamma_i,\end{aligned}\tag{3}$$

where $\mathbf{r} = (x, y) \in \Omega \subseteq [0, 1]^2$ is the spatial coordinate, $c_1, c_2, \dots, c_{11}, c_{12}, \dots \in \mathbb{R}$ are real-valued scalar coefficients, $s_1(\mathbf{r}), s_2(\mathbf{r}), \dots, s_{11}(\mathbf{r}), \dots$ are scalar-valued functions (which may serve as initial conditions, boundary values or coefficient fields in the equation), and $u_1, u_2, \dots : [0, 1] \times \Omega \rightarrow \mathbb{R}$ are unknown field variables to be solved in the equation. The boundary conditions are indexed by $i = 1, 2, \dots$. Here, we assume that each of the operators $\mathcal{F}, \mathcal{B}_1, \mathcal{B}_2, \dots$ admits a symbolic expression, which may involve differential and algebraic operations. The goal of PDEformer-2 is to construct a surrogate model of the solution mapping

$$(\Omega, \mathcal{F}, c_1, \dots, s_1(\mathbf{r}), \dots, \Gamma_1, \mathcal{B}_1, c_{11}, \dots, s_{11}(\mathbf{r}), \dots) \mapsto (u_1, u_2, \dots).$$

The input of this solution mapping includes the location of the computational domain Ω and the boundaries $\Gamma_1, \Gamma_2, \dots$, the symbolic expressions of the interior operator \mathcal{F} and boundary operators $\mathcal{B}_1, \mathcal{B}_2, \dots$, as well as the numeric information $c_1, \dots, c_{11}, \dots, s_1(\mathbf{r}), \dots, s_{11}(\mathbf{r}), \dots$ involved. The output includes all components of

the predicted solution, i.e., $u_1, u_2, \dots : [0, 1] \times \Omega \rightarrow \mathbb{R}$. For time-independent steady-state equations, we restrict the problem to $t = 0$ for simplicity, which requires only the prediction of $u_1, u_2, \dots : \{0\} \times \Omega \rightarrow \mathbb{R}$.

Model Overview

Figure 1 illustrates the overall network architecture of PDEformer-2, which is based on our previous PDEformer-1 [24] model. As shown in the figure, PDEformer-2 first formulates the symbolic expression of the PDE as a computational graph, and employs a scalar encoder and a function encoder to embed the numeric information of the PDE into the graph node features. PDEformer-2 then encodes this computational graph using a graph Transformer. The resulting latent vectors are fed into an INR decoder, allowing us to obtain the predicted values of each solution component of the PDE at specific spatio-temporal coordinates. In our implementation, the scalar encoder is a multi-layer perceptron (MLP), the function encoder is a convolutional neural network (CNN), the graph Transformer is based on the Graphormer architecture [32], and the INR decoder is an adapted version of Poly-INR [33]. More details about the network architecture can be found in Supplementary Information A.

Domain Shapes and Boundary Conditions

In terms of the complex domain shapes and boundary locations that may appear in two-dimensional equations, PDEformer-2 represents them as signed distance functions (SDFs), and embeds this information into the computational graph using the function encoder. If S is a subset of the square $[0, 1]^2$, its SDF is defined as

$$\text{SDF}_S(\mathbf{r}) = \begin{cases} \inf_{\mathbf{r}' \in S} d(\mathbf{r}, \mathbf{r}'), & \mathbf{r} \notin S, \\ -\inf_{\mathbf{r}' \notin S} d(\mathbf{r}, \mathbf{r}'), & \mathbf{r} \in S. \end{cases}$$

To feed a function $f : S \rightarrow \mathbb{R}$ into the function encoder, we first extend it to $f^{\text{ext}} : [0, 1]^2 \rightarrow \mathbb{R}$ by “nearest neighbor”, according to the formula⁶

$$f^{\text{ext}}(\mathbf{r}) = f\left(\arg \min_{\mathbf{r}' \in S} d(\mathbf{r}, \mathbf{r}')\right). \quad (4)$$

The example shown in Figure 15 demonstrates the way of using computational graphs to represent Dirichlet boundary conditions on the square domain. More examples can be found in Supplementary Information B.1.

Data Availability

The pretraining dataset, three customized adaptation datasets (Sine-Gordon, INS-Tracer, INS-Pipe), and the inverse problem datasets can be accessed via <https://github.com>.

⁶For simplicity of interpretation, we omit the technical discussions to make this formula theoretically valid. This would not cause troubles in practice, since the domain is typically discretized in real computation.

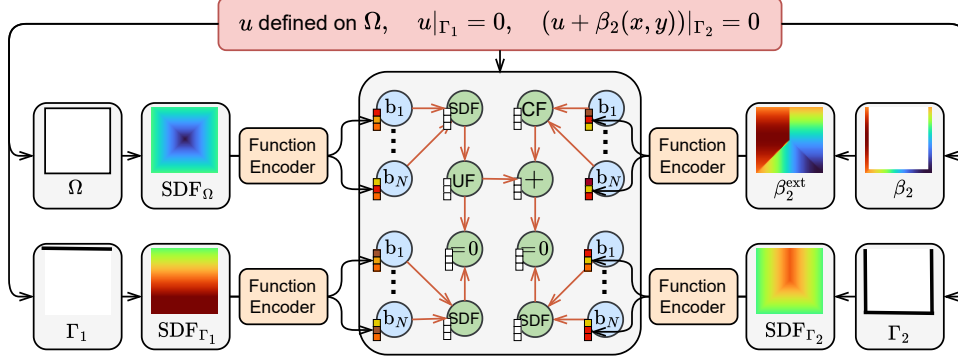


Fig. 15: An example of computational graph representation of non-periodic boundary conditions in a PDE, including a homogeneous Dirichlet boundary and an inhomogeneous one. The function $\beta_2(\mathbf{r})$ originally defined on Γ_2 is extended to the whole $[0, 1]^2$ before being fed into the function encoder.

[com/functoreality/pdefoundry-2](https://github.com/functoreality/pdefoundry-2). The two publicly available datasets include Wave-Gauss at <https://huggingface.co/datasets/camlab-ethz/Wave-Gauss> and Wave-C-Sines at <https://zenodo.org/records/14765453/files/Wave-C-Sines.nc>.

Code Availability

The source code of this paper is available in the GitHub repository at <https://github.com/functoreality/pdeformer-2>. The pretrained model weights for PDEformer-2-base are available at <https://gitee.com/functoreality/PDEformer2-L>, and PDEformer-2-fast at <https://gitee.com/functoreality/PDEformer2-M>.

Acknowledgements

Z.Y.’s contribution to this work includes two phases, in which the latter phase is completed during an internship at Huawei Technologies Co. Ltd. We thank Wendao Wu for his early-stage analysis of the non-physical Dedalus solutions with constructive discussions.

Author Contributions

Z.Y.: computational graph representation design & implementation, data generation—Dedalus, exploration for architecture & pretraining & finetuning, mainstream pretraining, adaptation—major, writing—major

Z.L.: exploration for architecture & pretraining & finetuning, inverse problems, prediction speed evaluation, solution visualization, writing—major

B.W.: data generation—FEniCSx, exploration for architecture & pretraining & finetuning, analysis related to Dedalus artifacts & failure cases, adaptation and speed evaluation of Poseidon & Geo-FNO, writing—related sections

H.J.: data generation—Dedalus MV-Wave, exploration for architecture & pretraining & finetuning, baseline investigation, adaptation and speed evaluation of MPP, writing—related sections

L.C.: early-stage exploration for architecture & training, investigation for dataset design

M.Z.: data generation—solver investigation & supporting early-stage exploration & improving implementation, baseline investigation, software & hardware infrastructure maintainance

X.H.: early-stage exploration for architecture & training, early-stage implementation

Q.M.: baseline investigation, improving implementation for parallel training, software & hardware infrastructure maintainance

J.Z.: assisting results analysis, software & hardware infrastructure maintainance

H.L.: project administration, design of code & data repository structure

B.D.: project administration, writing—overall structure & improving text logic & review

Competing Interests

The authors declare no competing interests.

References

- [1] Quarteroni, A., Manzoni, A., Negri, F.: Reduced Basis Methods for Partial Differential Equations: An Introduction, pp. 1–263. Springer, ??? (2015). <https://doi.org/10.1007/978-3-319-15431-2>
- [2] Li, Z., Kovachki, N., Azizzadenesheli, K., Liu, B., Bhattacharya, K., Stuart, A., Anandkumar, A.: Fourier Neural Operator for Parametric Partial Differential Equations (2021)
- [3] Lu, L., Jin, P., Pang, G., Zhang, Z., Karniadakis, G.E.: Learning nonlinear operators via deeponet based on the universal approximation theorem of operators. *Nature Machine Intelligence* **3**(3), 218–229 (2021) <https://doi.org/10.1038/s42256-021-00302-5>
- [4] Lorsung, C., Li, Z., Farimani, A.B.: Physics Informed Token Transformer (2023)
- [5] Yang, L., Liu, S., Osher, S.J.: Fine-Tune Language Models as Multi-Modal Differential Equation Solvers (2024)
- [6] Zhou, H., Ma, Y., Wu, H., Wang, H., Long, M.: Unisolver: Pde-conditional transformers are universal pde solvers. *CoRR* **abs/2405.17527** (2024)
- [7] Shen, J., Marwah, T., Talwalkar, A.: UPS: Efficiently building foundation models for PDE solving via cross-modal adaptation. *Transactions on Machine Learning Research* (2024)

- [8] Negrini, E., Liu, Y., Yang, L., Osher, S.J., Schaeffer, H.: A multimodal pde foundation model for prediction and scientific text descriptions. arXiv preprint arXiv:2502.06026 (2025)
- [9] Lorsung, C., Farimani, A.B.: Explain like i’m five: Using llms to improve pde surrogate models with text. arXiv preprint arXiv:2410.01137 (2024)
- [10] Liu, Y., Zhang, Z., Schaeffer, H.: PROSE: Predicting Operators and Symbolic Expressions using Multimodal Transformers (2023)
- [11] Sun, J., Liu, Y., Zhang, Z., Schaeffer, H.: Towards a foundation model for partial differential equations: Multioperator learning and extrapolation. *Physical Review E* **111**(3), 035304 (2025)
- [12] Sun, J., Zhang, Z., Schaeffer, H.: Lemon: Learning to learn multi-operator networks. arXiv preprint arXiv:2408.16168 (2024)
- [13] Liu, Y., Sun, J., He, X., Pinney, G., Zhang, Z., Schaeffer, H.: Prose-fd: A multimodal pde foundation model for learning multiple operators for forecasting fluid dynamics. arXiv preprint arXiv:2409.09811 (2024)
- [14] Yang, L., Liu, S., Meng, T., Osher, S.J.: In-context operator learning with data prompts for differential equation problems. *Proceedings of the National Academy of Sciences* **120**(39), 2310142120 (2023)
- [15] Yang, L., Osher, S.J.: Pde generalization of in-context operator networks: A study on 1d scalar nonlinear conservation laws. *Journal of Computational Physics* **519**, 113379 (2024) <https://doi.org/10.1016/j.jcp.2024.113379>
- [16] Cao, Y., Liu, Y., Yang, L., Yu, R., Schaeffer, H., Osher, S.: VICON: A Foundation Model for Multi-Physics Fluid Dynamics via Vision In-Context Operator Networks (2025). <https://arxiv.org/abs/2411.16063>
- [17] McCabe, M., Blancard, B.R.-S., Parker, L.H., Ohana, R., Cranmer, M., Bietti, A., Eickenberg, M., Golkar, S., Krawezik, G., Lanusse, F., Pettee, M., Tesileanu, T., Cho, K., Ho, S.: Multiple Physics Pretraining for Physical Surrogate Models (2023)
- [18] Hao, Z., Su, C., Liu, S., Berner, J., Ying, C., Su, H., Anandkumar, A., Song, J., Zhu, J.: DPOT: Auto-regressive denoising operator transformer for large-scale PDE pre-training. In: Salakhutdinov, R., Kolter, Z., Heller, K., Weller, A., Oliver, N., Scarlett, J., Berkenkamp, F. (eds.) *Proceedings of the 41st International Conference on Machine Learning*. *Proceedings of Machine Learning Research*, vol. 235, pp. 17616–17635. PMLR, ??? (2024). <https://proceedings.mlr.press/v235/hao24d.html>
- [19] Chen, T., Zhou, H., Li, Y., Wang, H., Gao, C., Zhang, S., Li, J.: Building flexible machine learning models for scientific computing at scale. *CoRR* **abs/2402.16014**

(2024)

- [20] Liu, Y., Sun, J., Schaeffer, H.: Bcat: A block causal transformer for pde foundation models for fluid dynamics. arXiv preprint arXiv:2501.18972 (2025)
- [21] Subramanian, S., Harrington, P., Keutzer, K., Bhimji, W., Morozov, D., Mahoney, M.W., Gholami, A.: Towards foundation models for scientific machine learning: Characterizing scaling and transfer behavior. *Advances in Neural Information Processing Systems* **36**, 71242–71262 (2023)
- [22] Rahman, M.A., George, R.J., Elleithy, M., Leibovici, D., Li, Z., Bonev, B., White, C., Berner, J., Yeh, R.A., Kossai, J., *et al.*: Pretraining codomain attention neural operators for solving multiphysics pdes. *Advances in Neural Information Processing Systems* **37**, 104035–104064 (2024)
- [23] Herde, M., Raonić, B., Rohner, T., Käppeli, R., Molinaro, R., Bézenac, E., Mishra, S.: Poseidon: Efficient foundation models for pdes. In: *Advances in Neural Information Processing Systems*, vol. 37 (2024). https://proceedings.neurips.cc/paper_files/paper/2024/hash/84e1b1ec17bb11c57234e96433022a9a-Abstract-Conference.html
- [24] Ye, Z., Huang, X., Chen, L., Liu, Z., Wu, B., Liu, H., Wang, Z., Dong, B.: Pdeformer-1: A foundation model for one-dimensional partial differential equations. arXiv preprint arXiv:2407.06664 (2024)
- [25] Burns, K.J., Vasil, G.M., Oishi, J.S., Lecoanet, D., Brown, B.P.: Dedalus: A flexible framework for numerical simulations with spectral methods. *Physical Review Research* **2**(2), 023068 (2020) <https://doi.org/10.1103/PhysRevResearch.2.023068> [arXiv:1905.10388](https://arxiv.org/abs/1905.10388) [astro-ph.IM]
- [26] Baratta, I.A., Dean, J.P., Dokken, J.S., Habera, M., Hale, J.S., Richardson, C.N., Rognes, M.E., Scroggs, M.W., Sime, N., Wells, G.N.: DOLFINx: the next generation FEniCS problem solving environment. preprint (2023). <https://doi.org/10.5281/zenodo.10447666>
- [27] Ronneberger, O., Fischer, P., Brox, T.: U-net: Convolutional networks for biomedical image segmentation. In: *Medical Image Computing and Computer-Assisted Intervention—MICCAI 2015: 18th International Conference, Munich, Germany, October 5–9, 2015, Proceedings, Part III* 18, pp. 234–241 (2015). Springer
- [28] Li, Z., Huang, D.Z., Liu, B., Anandkumar, A.: Fourier neural operator with learned deformations for pdes on general geometries. *Journal of Machine Learning Research* **24**(388), 1–26 (2023)
- [29] Mousavi, S., Wen, S., Lingsch, L., Herde, M., Raonić, B., Mishra, S.: Rigno: A graph-based framework for robust and accurate operator learning for pdes on arbitrary domains. arXiv preprint arXiv:2501.19205 (2025)

- [30] Kennedy, J., Eberhart, R.: Particle swarm optimization. In: Proceedings of ICNN'95 - International Conference on Neural Networks, vol. 4, pp. 1942–19484 (1995). <https://doi.org/10.1109/ICNN.1995.488968> . <https://ieeexplore.ieee.org/abstract/document/488968> Accessed 2024-04-03
- [31] Kingma, D.P.: Adam: A method for stochastic optimization. arXiv preprint arXiv:1412.6980 (2014)
- [32] Ying, C., Cai, T., Luo, S., Zheng, S., Ke, G., He, D., Shen, Y., Liu, T.-Y.: Do transformers really perform badly for graph representation? Advances in neural information processing systems **34**, 28877–28888 (2021)
- [33] Singh, R., Shukla, A., Turaga, P.: Polynomial implicit neural representations for large diverse datasets. In: Proceedings of the IEEE/CVF Conference on Computer Vision and Pattern Recognition, pp. 2041–2051 (2023)
- [34] Singh, R., Shukla, A., Turaga, P.: Polynomial implicit neural representations for large diverse datasets. In: 2023 IEEE/CVF Conference on Computer Vision and Pattern Recognition (CVPR), pp. 2041–2051 (2023). <https://doi.org/10.1109/CVPR52729.2023.00203>
- [35] Lu, L., Meng, X., Cai, S., Mao, Z., Goswami, S., Zhang, Z., Karniadakis, G.E.: A comprehensive and fair comparison of two neural operators (with practical extensions) based on fair data. Computer Methods in Applied Mechanics and Engineering **393**, 114778 (2022) <https://doi.org/10.1016/j.cma.2022.114778>

Supplementary Information

This supplementary information provides additional details on several key aspects of our work. Section A outlines the architecture of PDEformer-2 and the baseline models used in our experiments. Section B describes the construction of DAGs used as inputs to PDEformer-2, derived from various PDE forms. Section C presents all datasets employed in the experiments, including the pretraining dataset and those used for finetuning. Section D details the training settings, including procedures, hyperparameters, and further results on inverse problems. Finally, Section E offers additional visualizations comparing the predictions of PDEformer-2 with those of other baseline models on the PDEs discussed in the main text.

A Detailed Model Architecture

We shall present the detailed model architectures in this section, including PDEformer-2 and the baseline models. PDEformer-2 retains the overall architecture of PDEformer-1 [24], with modifications made only to the input dimension, the function encoder architecture, the activation function in INR, as well as some network hyperparameters (width and depth). However, for the convenience of readers, we provide the complete model architecture of PDEformer-2 here.

A.1 Overall Pipeline of PDEformer-2

A.1.1 Construct Graph

We first represent $\mathcal{F}, \mathcal{B}_1, \mathcal{B}_2, \dots$ in (3), i.e., the symbolic information specifying the form of the PDE and BCs, as a computational graph. In such a computational graph, a node may stand for a mathematical object or an operation, and a directed edge can be used to specify the operands involved in an operation. These nodes and edges constitute a directed acyclic graph (DAG) with heterogeneous nodes and homogeneous edges. Supplementary Information B provides more details and examples of such a computational graph.

Then, in order to include the numeric information, we endow each graph node with an input feature embedding vector $\xi \in \mathbb{R}^{d_e}$. This would involve three cases as follows: (1) For a scalar coefficient c , we input this numeric value into a scalar encoder, and use the d_e -dimensional output as the input features for the corresponding SC node. (2) In terms of a function $s(\mathbf{r})$ that typically contains more information, we shall introduce N new “branch” nodes, with types denoted as $\mathbf{b}_1, \mathbf{b}_2, \dots, \mathbf{b}_N$, respectively. These new nodes are then connected to the CF, IC, or SDF node corresponding to $s(\mathbf{r})$. We feed $s(\mathbf{r})$ into a function encoder, and use the output to generate the N input features of these branch nodes. (3) As for the remaining nodes, zero input features can be assigned conceptually, as they have no numeric information attached. To simplify implementation, we actually feed zero into the scalar encoder, and take its output as the input features of these nodes.

To improve model efficiency, the function $s(\mathbf{r})$ is not represented as scattered points as in PDEformer-1. Instead, we assume it is discretized on the 128×128 uniform grid of the entire domain $[0, 1]^2$, and this may require function extension (according to (4)) and interpolation in practise. The grid values are fed into a function encoder with a convolutional neural network (CNN) backbone, generating a single output vector with dimension $d_e N$. We then split this output vector into N parts, which form all the d_e -dimensional input features of the branch nodes. The value $N = 4$ is found to be sufficient in experiments, and is used in our PDEformer-2-base and PDEformer-2-fast models.

Moreover, for each unknown field variable to be solved, we introduce L additional nodes with types $\mathbf{m}_1, \mathbf{m}_2, \dots, \mathbf{m}_L$, respectively, and connect them to the corresponding UF node. These nodes will be used to decode the predicted solution, as will be explained in the following text. The specific value of L , being determined by the depth of the INR decoder, equals 11 for the PDEformer-2-base and PDEformer-2-fast models.

A.1.2 Encode Graph Data

The graph data obtained in the previous step contains both symbolic and numeric information inherent in the PDE. We shall integrate the information from the graph data, and generate a latent code that represents the solution for each field variable u_j to be solved. Each latent code takes the form

$$\boldsymbol{\mu}_j = [\mu_j^1, \dots, \mu_j^L]^T \in \mathbb{R}^{L \times d_e}.$$

The fusion process leverages a graph Transformer, a powerful type of graph neural network based on the Transformer architecture, which is skilled at capturing and expressing complex graph structural information. In practice, we adopt the Graphormer architecture [32], and make some adjustments to adapt it specifically for encoding PDEs. For each variable index j and INR layer index ℓ , the **UF** node representing u_j is connected with another node with type \mathbf{m}_ℓ . We let $\mu_j^\ell \in \mathbb{R}^{d_e}$ be the embedding vector assigned to this \mathbf{m}_ℓ node in the output layer of the graph Transformer.

A.1.3 Decode PDE Solution

We employ an INR that takes the spatio-temporal coordinate (t, x, y) as input, and produces the mesh-free prediction $\hat{u}_j(t, x, y)$ according to μ_j for each field variable. In consistency with PDEformer-1 [24], we utilize an adapted version of Poly-INR [34] with $L = 11$ hidden layers, and the modulations of the ℓ -th hidden layer is generated according to μ_j^ℓ .

A.2 Detailed PDEformer-2 Architecture

A.2.1 Scalar and Function Encoder

The scalar encoder is a multi-layer perceptron (MLP) that has two hidden layers with 256 neurons each. The input has dimension one (i.e., a scalar input), and the output dimension equals $d_e = 768$, the embedding dimension of the graph Transformer.

To encode functions defined on 2D uniform grids, we employ a lightweight convolutional neural network (CNN). The input has a single channel and a resolution of 128×128 . Our CNN consists of the following layers:

1. 2D convolution with 32 output channels, stride 4, kernel size 4×4 , with bias included.
2. Rectified linear unit (ReLU) activation function.
3. 2D convolution with 128 output channels, stride 4, kernel size 4×4 , with bias included.
4. ReLU activation function.
5. 2D convolution with 768 output channels, stride 4, kernel size 4×4 , with bias included.
6. Flattening operation, applied to the 2×2 feature map with 768 channels.
7. Vector splitting into $N = 4$ feature embeddings assigned to the branch nodes.

A.2.2 Graph Transformer

Initial Embedding Vector

In the graph Transformer, the initial embedding of node i is given as

$$h_i^{(0)} = x_{\text{type}(i)} + \xi_i + z_{\deg^-(i)}^- + z_{\deg^+(i)}^+,$$

where $\xi_i \in \mathbb{R}^{d_e}$ is the input feature embedding vector of node i , and $x, z^-, z^+ \in \mathbb{R}^{d_e}$ are learnable vectors specified by node type $\text{type}(i)$, in-degree $\deg^-(i)$ and out-degree $\deg^+(i)$, respectively.

Attention Bias

We denote $\phi(i, j)$ to be the shortest path length from node i to node j . If such a path does not exist or has a length greater than 14, we set $\phi(i, j) = 14$. For each attention head involved in the graph Transformer, the attention bias according to the node pair (i, j) is given as

$$B_{ij} = b_{\phi(i,j)}^+ + b_{\phi(j,i)}^- + d_{ij}. \quad (5)$$

Here, $b_{\phi(i,j)}^+, b_{\phi(j,i)}^-$ are learnable scalars indexed by $\phi(i, j)$ and $\phi(j, i)$, respectively, and is shared across all layers. The additional term d_{ij} , which does not appear in the original Graphormer, is introduced to mask out attention between disconnected node pairs. More specifically, when node i and node j are connected in the graph, i.e., there exists a path either from i to j or from j to i , we take $d_{ij} = 0$, and set $d_{ij} = -\infty$ otherwise. Moreover, since our graph has homogeneous edges, we do not include the edge encoding term that appears in the original Graphormer.

Graph Transformer Layer

The structure of the graph transformer layer is the same as the original Graphormer, and we include it here for convenience to the readers. Each layer takes the form

$$\bar{h}^{(l)} = \text{Attn}(\text{LN}(h^{(l-1)})) + h^{(l-1)} \quad (6)$$

$$h^{(l)} = \text{FFN}(\text{LN}(\bar{h}^{(l)})) + \bar{h}^{(l)}, \quad (7)$$

where FFN represents a position-wise feed-forward network with a single hidden layer and GeLU activation function, and LN stands for layer normalization. In terms of the self-attention block Attn, we shall follow the convention in the original Graphormer paper and only present the single-head case for simplicity. Let $H = [h'_1, \dots, h'_n]^T \in \mathbb{R}^{n \times d_e}$ denote the input of the self-attention module involving n graph nodes, the self-attention is computed as

$$\begin{aligned} Q &= HW_Q, \quad K = HW_K, \quad V = HW_V, \\ A &= \frac{QK^T}{\sqrt{d_e}} + B, \quad \text{Attn}(H) = \text{softmax}(A)V, \end{aligned}$$

where $W_Q, W_K, W_V \in \mathbb{R}^{d_e \times d_e}$ are the projection matrices, and B is the attention bias given in (5). The extension to the multi-head attention is standard and straightforward.

Hyperparameters

PDEformer-2, including base and fast variants, uses 12 graph Transformer layers with embedding dimension $d_e = 768$, FFN embedding dimension 1536, and 32 attention heads. This configuration is selected based on our previous experience of PDEformer-1 [24].

A.2.3 INR

In the realm of implicit neural representation (INR), data objects are interpreted as coordinate-based functions, where each function accepts a coordinate (t, x, y) as input

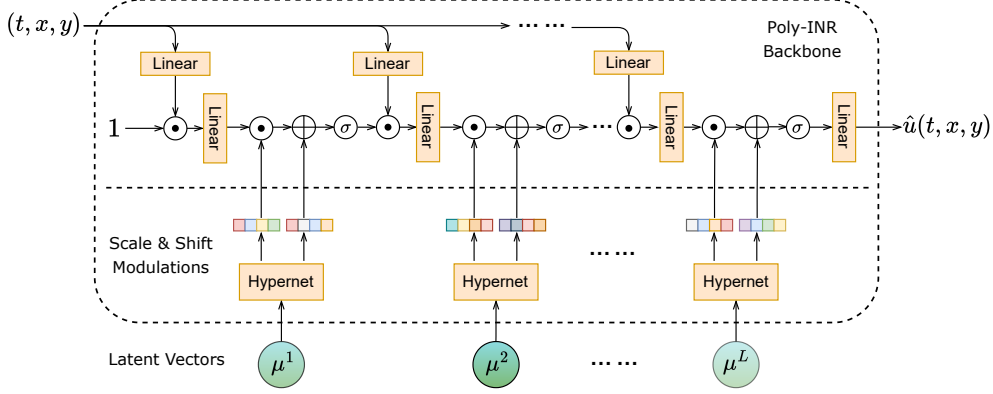


Fig. 16: INR decoder architecture of PDEformer-2.

and yields an approximated function value $\hat{u}(t, x, y)$ at that specific coordinate point. Among various INR architectures proposed in the literature, PDEformer-2 employs an adapted version of Poly-INR [34]. We make a modification to the L hypernets in the Poly-INR structure, in which the ℓ -th hypernet takes $\mu^\ell \in \mathbb{R}^{d_e}$ as its input, and generates the scale- and shift-modulations for the ℓ -th hidden layer of our Poly-INR.

The architecture of our INR decoder is illustrated in figure 16, with the mathematical framework detailed below. We take $h_0 = \mathbf{1}$ to be the vector with all entries being equal to one. For $\ell = 1, 2, \dots, L$, we compute

$$g_\ell = W_\ell^{\text{in}} \begin{bmatrix} t \\ x \\ y \end{bmatrix} + b_\ell^{\text{in}}, \quad s_\ell^{\text{scale}} = \text{MLP}_\ell^{\text{scale}}(\mu^\ell), \quad s_\ell^{\text{shift}} = \text{MLP}_\ell^{\text{shift}}(\mu^\ell),$$

$$q_\ell = s_\ell^{\text{scale}} \odot (W_\ell^{\text{h}}(h_{\ell-1} \odot g_\ell) + b_\ell^{\text{h}}) + s_\ell^{\text{shift}}, \quad h_\ell = \sigma(q_\ell),$$

and the network output is given as $\hat{u}(t, x, y) = W^{\text{Last}} h_L + b^{\text{Last}}$. Here, the activation function $\sigma(\cdot)$ is a sine function with output scaled by $\sqrt{2}$, which performs slightly better than the clipped leaky-ReLU operation used in PDEformer-1. The hypernets correspond to $\text{MLP}_\ell^{\text{scale}}$ and $\text{MLP}_\ell^{\text{shift}}$. Note that in the original Poly-INR, the hypernets are utilized to generate W_ℓ^{in} and b_ℓ^{in} . Compared with our practice of generating s_ℓ^{scale} and s_ℓ^{shift} , this method makes training slower, and is not adopted in our implementation.

PDEformer-2-base uses an INR containing $L = 11$ hidden layers with 768 neurons each. Discretization of 2D time-dependent PDEs often involve many grid points (typically $101 \times 128 \times 128$ in our pretraining dataset). The INR deals with each grid point independently, which may be computational intensive to make an inference. This can be seen in the difference of the inference time between full prediction and Encoder-Only in Table 3. To accelerate model inference, PDEformer-2-fast employs a relatively smaller INR, with the width reduced to 256 from 768. This is the only difference between the base and the fast variants. We keep the number of hidden layers L so as not to affect the computational graph structures.

We focus on 2D PDEs in this work, and the coordinates should only involve (t, x, y) . However, to make our code compatible for future extension to 3D PDEs, the z coordinate is also included in the INR input. This coordinate remains zero in all the experiments, and does not affect the results. The same convention applies to the baseline DeepONet trunk networks in the experiments.

A.3 Baseline Models

DeepONet

We implement two variants of DeepONet [3], each comprising a trunk network and a branch network. The trunk network is a six-layer MLP of width 256, and accepts spatio-temporal coordinates as network input. The branch network accepts the coefficient scalars and fields in PDE as network input, and generates a vector of dimension $n_o = 2048$. In consideration of the multi-output case with $n_v > 1$ variables to predict, we adopt approach 4 mentioned in Section 3.1.6 of Lu et al. [35], and split the trunk network output into n_v groups, each with n_o neurons. For $k = 1, 2, \dots, n_v$, we select the k -th group of the trunk network output, and take inner product with the entire branch network output to get the prediction of the k -th variable. The case of $n_v = 1$ would degenerate to the vanilla DeepONet initially proposed in Lu et al. [3].

The direct variant, designated as “DeepONet (MLP)”, employs a six-layer MLP branch network of width 256. The input of the MLP contains the variable coefficient scalars, as well as the grid values of all coefficient fields involved. The coefficient fields in the datasets are typically discretized on a uniform grid with resolution 128×128 . Such a fine resolution may introduce too many grid points, leading to a high input dimension of the branch MLP. This can make our NPU run out of memory in the experiments, especially when a number of (for example, four for the INS-Pipe dataset) such coefficient fields are involved. Therefore, we downsample the coefficient fields to a resolution of 64×64 before feeding them into the MLP branch network.

When DeepONet was initially proposed in Lu et al. [3], the authors have emphasized that the architectures of the branch and trunk networks can be arbitrary. To better account for the nature of 2D PDEs, we introduce another DeepONet variant with the branch network replaced by a CNN, referred to as “DeepONet (CNN)”. The CNN possesses six convolutional layers followed by two fully connected layers. Each PDE coefficient scalar is treated as a constant coefficient field, and form an independent channel of the CNN input.

U-Net

The U-Net [27] model features a symmetric design with five downsampling and five upsampling stages. The number of channels along the downsampling pathway equals 64, 128, 256, 512, and 512, respectively, while upsampling utilizes 1024, 512, 256, 128, and 64. A linear projection then applies to the feature map with 64 channels to get the final output. All layers employ ReLU activation functions. The network input is arranged in the same way as the branch network of DeepONet (CNN). As a 2D neural operator, U-Net treats the n_t temporal steps as extended channels, leading to a total of $n_t n_v$ output channels.

FNO

Our implementation includes both two-dimensional and three-dimensional variants of the Fourier Neural Operator (FNO) [2]. The input and output of the 2D variant is formulated in the same way as U-Net. The 3D variant treats the temporal axis as an additional spatial dimension with resolution n_t . The network input, containing both scalar and field channels, is replicated along this new dimension to fit into the network. Both variants employ four Fourier layers with 20 hidden channels, and retain 12 Fourier modes in each spatial dimension. The final output is generated by a MLP with a single hidden layer of width 128. The Wave-Gauss dataset provided by PDEGYM [23] has only $n_t = 16$ timesteps, and we reduce the number of Fourier modes to 6 along the temporal axis when applying FNO3D to this dataset.

Geo-FNO

The Geometry-aware Fourier Neural Operator (Geo-FNO) [28] extends the standard FNO framework to handle irregular geometries by deforming physical domains into a uniform latent space compatible with FFT operations. Our implementation replicates the official Geo-FNO architecture, which consists of a deformation mapping network and a FNO backbone, which are jointly optimized in an end-to-end manner.

The FNO component employs five Fourier layers with 32 hidden channels and 12 Fourier modes per spatial dimension. The deformation mapping network is a MLP consisting of four hidden layers, with 32, 128, 128, and 128 neurons, respectively.

The model takes two input tensors: (i) the input function values of size (n_{xy}, c_{in}) , where c_{in} is the number of input variables, and (ii) the coordinates of mesh points in the physical domain of size $(n_{xy}, 2)$. The output tensors are of size (n_{xy}, c_{out}) , with $c_{out} = n_t \times n_v$ accounting for n_t temporal steps and n_v target variables.

Poseidon

Poseidon [23] is a foundation model for learning the solution operators of PDEs, leveraging a transformer-based architecture to capture complex spatio-temporal dynamics. The model is designed to approximate the underlying solution operator $\mathcal{S} : [0, T] \times \mathcal{X} \rightarrow \mathcal{X}$, such that $u(t) = \mathcal{S}(t, u_0)$ is the solution of the PDE at any time $t \in [0, T]$ given the initial condition u_0 . Additional coefficient scalars and fields (such as variable viscosity and source terms) are treated as additional components (channels) of u , and excluded in the computation of finetuning loss. We use the pretrained Poseidon-B model in our experiments, since its number of parameters (158M) is close to our PDEformer-2-base and PDEformer-2-fast models.

Multiple Physics Pretraining (MPP)

Multiple Physics Pretraining (MPP) [17] is a pretraining strategy designed for learning from multiple physical systems simultaneously. It embeds data from different dynamics into a shared representation space while maintaining separation between systems at certain network layers. This allows the model to learn transferable representations across equations, while still preserving task-specific information. Similar to Poseidon-B, we choose the MPP-AViT-B model provided by the official MPP repository in our experiments.

During inference, MPP predicts the solution at the next time step only. To obtain a full trajectory from the initial conditions, predictions must be generated sequentially in an autoregressive manner. This is very different from PDEFormer-2, which can make direct predictions at arbitrary spatio-temporal coordinates, without relying on step-by-step recursive evaluation.

A total of 16 consequent time snapshots were taken as the model input when MPP was pretrained. Since the prediction task in our experiments requires to generate the whole solution according to the initial state, we only take a single time snapshot as the model input during our finetuning process.

MPP distinguishes between different physical equations by assigning distinct channels in specific intermediate layers for each equation. The number of such channels is fixed, which limits the total number of variables that can be accommodated in the pretrained model, unless we introduce additional network parameters with random initialization. To enable direct finetuning on additional equation types beyond those in the public model weights, we selectively enable channel sharing between new equations and those with similar physical characteristics in its original pretraining dataset.

MPP is not designed to handle equations with varying input coefficient fields. To address this, we treat the coefficient fields as additional components (channels) of the PDE solution. During prediction, the coefficient field is included in the model output but ignored during the autoregressive updating process. Its prediction errors are also excluded from the evaluation metrics.

B Computational Graph Representation of PDEs

The overall idea of representing PDEs as a computational graph is mainly consistent with our previous PDEformer-1 [24]. We shall explain the differences in detail in this section.

B.1 Domain Shape and Boundary Conditions

In order to inform the model of the domain shape Ω , we first convert it to a function $\text{SDF}_{\Omega}(\mathbf{r})$. Another possible method for such conversion would be using characteristic functions, which takes value one inside Ω and zero outside Ω . However, we believe that SDFs have the following advantages:

- SDFs contains richer information. Even when it is discretized on a grid with relatively low resolution, we can still recover the approximate boundary of Ω .
- SDFs are more sensitive to topological changes. For example, if we dig a very small hole inside Ω , its SDF changes a lot, but the characteristic function does not change as much, especially in the L^2 sense. We want to inform model of the change, since the corresponding solution may change significantly in this case.
- Besides domains, edges and line segments with zero area can also be described by SDFs. If characteristic functions are used, we may have to first expand the lines to a certain level of thickness, especially when the characteristic function is discretized on a relatively low-resolution grid. Specifying boundary conditions

requires declaration of the boundary location that are typically lines, and SDF provides a unified representation of these domains and boundaries.

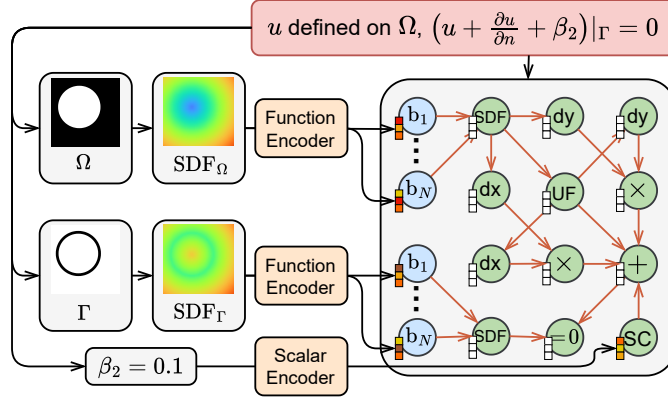


Fig. 17: Computational graph example of non-periodic boundary conditions in a PDE. The domain Ω is a disk, and inhomogeneous Robin boundary condition is imposed on its boundary circle.

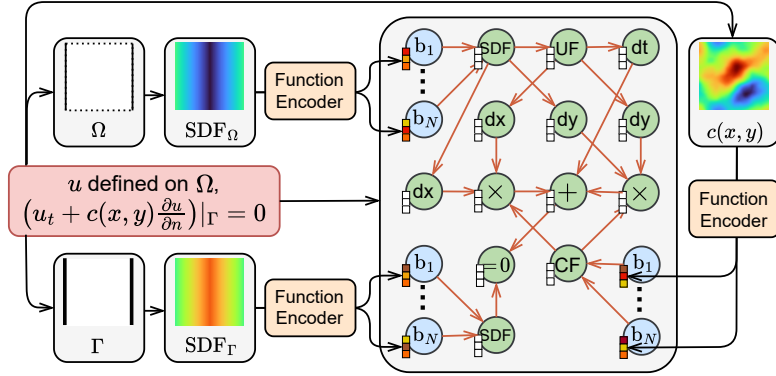


Fig. 18: Computational graph example of non-periodic boundary conditions in a PDE. The square domain Ω is assumed to be periodic along the y -axis, and the wave-absorbing Mur boundary condition is imposed on the left and right edges.

In addition to Figure 15 in the main text, Figure 17 and 18 give two additional examples of how domain shapes and boundary conditions can be represented as computational graphs. We also have the following remarks on the representation:

- When the domain $\Omega = [0, 1] \times [0, 1]$ is periodic along both axes, it is deemed equivalent to the two-dimensional torus $S^1 \times S^1$, and the SDF cannot be defined. The UF

nodes do not have a SDF predecessor in the computational graph. An example is the advection equation in Figure 1 in the main text.

- If Ω is periodic along one axis, say x without loss of generality, we shall require⁷ $\Omega = [0, 1] \times [a, b]$ for some $0 \leq a < b \leq 1$. By identifying Ω with $S^1 \times [a, b]$ as a metric space, the definition of SDF only takes into account the distance along the y -axis.
- Only non-periodic boundary conditions need to be specified in the computational graph. Periodic BCs are assumed by default, and introduce no additional graph nodes.
- For $\partial_{\mathbf{n}} = \frac{\partial}{\partial \mathbf{n}}$, i.e., derivative along the outward normal direction on the boundary of Ω , we shall use the fact $\mathbf{n}(\mathbf{r}) = \nabla \text{SDF}_{\Omega}(\mathbf{r})$ for $\mathbf{r} \in \partial\Omega$. This indicates

$$\partial_{\mathbf{n}} u = \mathbf{n} \cdot \nabla u = \nabla \text{SDF}_{\Omega}(\mathbf{r}) \cdot \nabla u = u_x \cdot \partial_x \text{SDF}_{\Omega}(\mathbf{r}) + u_y \cdot \partial_y \text{SDF}_{\Omega}(\mathbf{r}),$$

and the corresponding computational graph representation follows.

B.2 Terms with Unknown Formulations

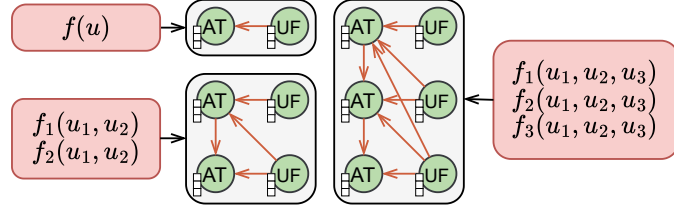


Fig. 19: Computational graph examples of an arbitrary transformation $\mathbf{f} : \mathbb{R}^m \rightarrow \mathbb{R}^n$ that may occur in some PDEs, showing $n = 1, 2, 3$.

In some specific physical scenarios encountered in real applications, the underlying physical mechanism might not be completely clear, and the corresponding PDE may contain interaction terms without a known symbolic expression. When we finetune PDEformer to adapt to such scenarios using collected sensor data, it would seem better to inform the model of these extra interactions. Such interaction terms would typically involve an arbitrary transformation $\mathbf{f} : \mathbb{R}^m \rightarrow \mathbb{R}^n$ with input values u_1, u_2, \dots, u_m and output values f_1, f_2, \dots, f_n . This subsection interprets the conventions we made to represent this transformation using computational graphs.

We first consider the case $m = n$. The input values u_i should already have their corresponding nodes in the computational graph, and we create a node with type AT for each output value f_i . The f_1 node receives edges from all input nodes u_1, \dots, u_n . For $i = 2, 3, \dots, n$, the f_i node receives edges from f_{i-1} and u_i, u_{i+1}, \dots, u_n . Such an edge convention is introduced only to indicate the non-equivalence of the input and the output nodes. Figure 19 illustrates the cases of $m = n = 1, 2, 3$.

For the case $m < n$, we include $(n - m)$ additional scalar coefficients c_{m+1}, \dots, c_n to the input values, and the augmented transformation $\tilde{\mathbf{f}} : (u_1, \dots, u_m, c_{m+1}, \dots, c_n) \mapsto$

⁷All datasets in our experiments in this work satisfy $a = 0, b = 1$ for simplicity.

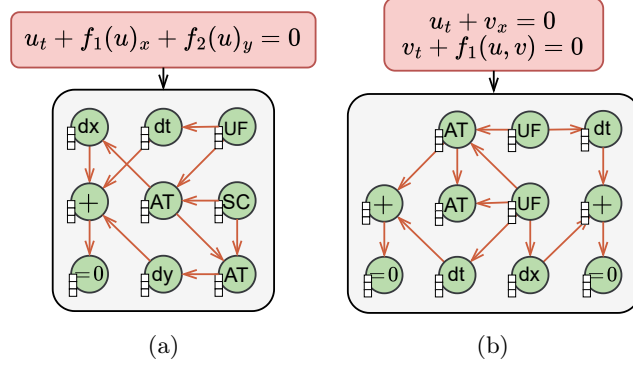


Fig. 20: Two computational graph examples of PDEs involving terms without known formulations. An extra scalar coefficient (SC) node is introduced to complete the computational graph in (a).

(f_1, \dots, f_n) can be represented as discussed earlier. The specific values of these coefficients can be any fixed real numbers, and zeros are typically used if only one such transformation is included in the PDE. Figure 20a illustrates the computational graph of the PDE $u_t + f_1(u)_x + f_2(u)_y = 0$, which includes a transformation with $m = 1$ and $n = 2$ that represents the unknown flux functions in the conservation law.

For the case $m > n$, we include instead $(m - n)$ additional output values f_{n+1}, \dots, f_m , resulting in an augmented transformation $\tilde{f} : (u_1, \dots, u_m) \mapsto (f_1, \dots, f_m)$ represented as before. The AT nodes corresponding to these additional outputs will be created, but will not be used, i.e., they emit no edges towards the other nodes in the graph. Figure 20b illustrates the computational graph of the PDE $u_t + v_x = 0, v_t + f_1(u, v) = 0$, which includes a transformation with $m = 2$ and $n = 1$.

Note that such a convention is only designed for the task of solving forward problems, in which we want to make predictions according to collected data. Some scientific and engineering scenarios may also require system identification, which should recover the explicit mathematical formulation of the additional term. If the additional term can be represented as a linear combination of a preselected set of candidate terms, this could be accomplished in a way similar to Section D.3.2. The more general case is left for future work.

B.3 Summary of Node Types

Only a small number of node types are involved in the computational graph. We list them as follows:

Mathematical objects: UF (unknown field variable), SC (scalar coefficient), CF (coefficient field), VC (varying coefficient), IC (initial condition), SDF (signed distance function).

Differential operations: dt, dx, dy.

Algebraic operations: $+$ (sum), \times (product), $-$ (negation), $(\cdot)^2$ (square), $= 0$ (being equal to zero).

Special functions: `sin`, `cos` (trigonometric functions), `exp10`, `log10` (exponential and logarithm of base 10), `AT` (arbitrary transformation).

Auxiliary nodes: $\mathbf{b}_1, \mathbf{b}_2, \dots, \mathbf{b}_N$ (branch nodes to receive input from function encoder), $\mathbf{m}_1, \mathbf{m}_2, \dots, \mathbf{m}_L$ (modulation nodes to generate output into INR decoder), `pad` (padding nodes to enable batch training).

Note that the exponential and logarithm operations are of base 10 instead of e . We adopt such a convention to suppress the magnitude of the input into scalar and function encoders, since typical neural networks work better for $O(1)$ inputs and outputs. For example, $\log_{10} 10^{-3}$ has a smaller absolute value than $\log_e 10^{-3}$.

C Datasets

C.1 Pretraining

To generate random PDEs that constitute our dataset, we randomly set the coefficients in a generic PDE form to obtain randomized specific forms of PDEs. In the specific form, zero terms (including terms with zero coefficients) are removed. If a term has coefficient one, this coefficient no longer appears in the specific form, for example “ $+1u$ ” would degenerate to “ $+u$ ”. Coefficient fields that has a constant value are treated as scalar coefficients. Such a specific form simplifies the mathematical expression of the PDE as well as the corresponding computational graph.

Indeed, not all such specific PDEs admits a valid solution on the whole time interval $t \in [0, 1]$. Even if it does, the traditional solver may also fail if the solver parameters are incompatible with the current PDE. Lacking a practical criterion to automatically identify these case and tune solver parameters, we choose the naïve method to discard the sampled PDEs that our traditional solvers failed to solve, and only record the successful results in our datasets. The rate of a successful solution differs across different datasets, ranging from 10% to 90%.

A total of 8 generic PDE forms are included in our pretraining dataset, and will be introduced in detail in the following text.

C.1.1 Diffusion-Convection-Reaction (DCR) Equation

The PDE takes the form

$$u_t + Lu + f_0(u) + s(\mathbf{r}) + f_1(u)_x + f_2(u)_y = 0,$$

$$u(0, \mathbf{r}) = g(\mathbf{r})$$

for $t \in [0, 1]$, $\mathbf{r} = (x, y) \in \Omega \subseteq [0, 1]^2$. On each edge Γ_i , the boundary condition imposed is either periodic or of the general form $B_i u(\mathbf{r}) = 0$ for $\mathbf{r} \in \Gamma_i$.

The initial value is generated as a Gaussian random field (GRF) according to

$$g(\mathbf{r}) \sim \mathcal{N}(0, 50^2(-\Delta + 5^2 I)^{-3}). \quad (8)$$

Table 4: Summary of the pretraining datasets. The number of testing samples is fixed to 1k for all datasets, and not shown in the table.

PDE Type	Dataset Name	Training Samples	Recorded Variables
DCR	dcr_base	110k	u
	dcr_npX	105k	u
	dcr_npY	105k	u
	dcr_disk	200k	u
	dcr_sJ3	125k	u
	dcr_inhom	100k	u
Wave	wave_base	125k	u
	wave_npX	90k	u
	wave_npY	90k	u
	wave_disk	200k	u
	wave_inhom	100k	u
MV-DCR	mvdcr_2	160k	u_0, u_1
	mvdcr_2_0	100k	u_0, u_1
	mvdcr_3_1	200k	u_0, u_1, u_2
	mvdcr_4_0	200k	u_0, u_1, u_2, u_3
DC-DCR	dcocr_icA	100k	u_0, u_1, p
	dcocr_icV	100k	u_0, u_1, p
MV-Wave	mvwave_2	120k	u_0, u_1
	mvwave_3	100k	u_0, u_1, u_2
	mvwave_4	100k	u_0, u_1, u_2, u_3
DC-Wave	dcwave_icA	100k	u_0, u_1
	dcwave_icV	100k	u_0, u_1
G-SWE	swe	100k	h, u, v
Elasticity	elasticity	255k	u, v

The source term $s(\mathbf{r})$ is taken to be zero, one, a random scalar from $U([-1, 1])$, or a GRF as in (8), with probability 5 : 1 : 5 : 5. For the convection flux and reaction term, we take $f_i(u) = \sum_{k=1}^3 c_{i0k} u^k + \sum_{j=1}^{J_i} c_{ij0} h_{ij}(c_{ij1} u + c_{ij2} u^2)$ for $i = 0, 1, 2$, where the non-negative integers $J_0 + J_1 + J_2 \leq J$ are randomly generated. Each scalar coefficient c_{ijk} involved is taken to be zero, one, or a random scalar drawn from $U([-1, 1])$.

The spatial second-order term (diffusion for DCR) Lu is randomly selected from the non-divergence form $Lu = -a(\mathbf{r})\Delta u$, the factored form $Lu = -\sqrt{a(\mathbf{r})}\nabla \cdot (\sqrt{a(\mathbf{r})}\nabla u)$, and the divergence form $Lu = -\nabla \cdot (a(\mathbf{r})\nabla u)$ with equal probability. For the homogeneous case, $\log_{10} a(\mathbf{r}) \sim U([-3, -2])$ is a random scalar. If the flux functions $f_1(u), f_2(u)$ are both linear, we set $a(\mathbf{r})$ to zero with probability 0.2. For the inhomogeneous case, we generate a GRF as in (8), rescale and shift to make its range span a random subinterval of $[-3, -1]$, and then take exponential with base 10 to get $a(\mathbf{r})$.

Each boundary operator $B_i u$ is taken to be Robin with type I $B_i u = u + \beta_i(\mathbf{r})\partial u/\partial n + \gamma_i(\mathbf{r})$, or Robin with type II $B_i u = \alpha_i(\mathbf{r})u + \partial u/\partial n + \gamma_i(\mathbf{r})$, with equal probability. Each of the coefficient field $\alpha_i(\mathbf{r}), \beta_i(\mathbf{r}), \gamma_i(\mathbf{r})$ is taken to be zero, one, a random scalar from $U([-1, 1])$, or a GRF in (8), with probability 5 : 1 : 5 : 5. Note that when $\alpha_i(\mathbf{r})$ or $\beta_i(\mathbf{r})$ equals zero, the boundary condition would degenerate to the

Dirichlet type or the Neumann type. We may also set $\gamma_i(\mathbf{r})$ to be compatible with the initial condition with certain probability.

As part of our PDE, the generic boundary condition reduces to specific forms after these coefficients are selected. If the boundary conditions share the same specific form across multiple edges Γ_i , we merge them into a single edge, and the computational graph is further simplified.

We have prepared several datasets for DCR equation, each containing at least 100k training samples. The datasets are listed as follows:

- **dcr_base**: Basic DCR dataset, being periodic along both axes (involving no boundary operators) on $\Omega = [0, 1]^2$, with $J = 0$ (no sinusoidal terms). Diffusion is homogeneous, i.e., $a(\mathbf{r})$ is a constant field, degenerating to a random scalar.
- **dcr_npX**: Non-periodic along the x -axis of $\Omega = [0, 1]^2$, and the boundary conditions at the left and right edges need to be generated. (We only mark the difference from **dcr_base**. This applies to the other datasets.)
- **dcr_npY**: Non-periodic along the y -axis.
- **dcr_disk**: The domain is a random disk $\Omega = D(\mathbf{r}_0; R) \subseteq [0, 1]^2$, with $R \sim U([0.3, 0.5])$, $\mathbf{r}_0 \sim U([R, 1 - R]^2)$. The boundary condition on the outer boundary circle needs to be generated.
- **dcr_sJ3**: The PDE contains up to $J = 3$ sinusoidal terms.
- **dcr_inhom**: Diffusion is inhomogeneous, and $a(\mathbf{r})$ has spatial dependency.

C.1.2 Wave Equation

The PDE takes the form

$$u_{tt} + \mu(\mathbf{r})u_t + Lu + f_0(u) + s(\mathbf{r}) + f_1(u)_x + f_2(u)_y = 0,$$

$$u(0, \mathbf{r}) = g(\mathbf{r}), \quad u_t(0, \mathbf{r}) = h(\mathbf{r})$$

for $t \in [0, 1]$, $\mathbf{r} = (x, y) \in \Omega \subseteq [0, 1]^2$. On each edge Γ_i , the boundary condition imposed is either periodic or of the general form $B_i u(\mathbf{r}) = 0$ for $\mathbf{r} \in \Gamma_i$.

The initial values $g(\mathbf{r}), h(\mathbf{r})$ are generated as independent GRFs given in (8). The source term $s(\mathbf{r})$ is the same as in DCR equation, and the damping coefficient $\mu(\mathbf{r})$ is generated similarly and independently. For the homogeneous case, the squared velocity field $a(\mathbf{r})$ in the spatial second-order term Lu is taken to be zero, one, or a random positive scalar satisfying $\log_{10} a(\mathbf{r}) \sim U([-2, \log_{10} 4])$. The probability for the three cases is 5 : 2 : 18 if $f_1(u), f_2(u)$ are both zeros, and 0 : 1 : 9 otherwise. The inhomogeneous case is similar to that of DCR equation, in which we let $\log_{10} a(\mathbf{r})$ span a subinterval of $[-2, \log_{10} 4]$.

Each boundary operator $B_i u$ is taken to be Robin with type I $B_i u = u + \beta_i(\mathbf{r})\partial u/\partial n + \gamma_i(\mathbf{r})$, Robin with type II $B_i u = \alpha_i(\mathbf{r})u + \partial u/\partial n + \gamma_i(\mathbf{r})$, or generalized Mur type $B_i u = u_t + \alpha_i(\mathbf{r})u + \beta_i(\mathbf{r})\partial u/\partial n + \gamma_i(\mathbf{r})$, with equal probability. Note that when $\alpha_i(\mathbf{r}) = 0, \beta_i(\mathbf{r}) = c(\mathbf{r})$ is the wave velocity, and $\gamma_i(\mathbf{r}) = 0$, the generalized Mur boundary condition becomes the ordinary Mur boundary condition that can absorb waves.

The remaining settings are the same as the DCR equation.

List of datasets:

- **wave_base**: Basic wave dataset, being periodic along both axes of $\Omega = [0, 1]^2$, with $J = 3$ (up to 3 sinusoidal terms). Wave velocity is homogeneous.
- **wave_npX**: Non-periodic along the x -axis of $\Omega = [0, 1]^2$. (We only mark the difference from **wave_base**.)
- **wave_npY**: Non-periodic along the y -axis.
- **wave_disk**: The domain is a random disk $\Omega = D(\mathbf{r}_0; R) \subseteq [0, 1]^2$ like **dcr_disk**. We do not introduce any sinusoidal terms ($J = 0$) for simplicity.
- **wave_inhom**: Wave velocity is inhomogeneous, and has spatial dependency.

C.1.3 Multi-Variable DCR Equation (MV-DCR)

The PDE system includes d_u equations and initial conditions, in which the one indexed by $i \in \{0, \dots, d_u - 1\}$ takes the form

$$\partial_t u_i + L_i u_i + \mathbf{f}_0(\mathbf{u})_i + s_i(\mathbf{r}) + \partial_x \mathbf{f}_1(\mathbf{u})_i + \partial_y \mathbf{f}_2(\mathbf{u})_i = 0,$$

$$u_i(0, \mathbf{r}) = g_i(\mathbf{r})$$

for $t \in [0, 1]$, $\mathbf{r} = (x, y) \in [0, 1]^2$. Periodic boundary conditions along both axes are employed for simplicity.

For the reaction and convection flux functions, we take

$$\mathbf{f}_l(\mathbf{u})_i = \sum_{0 \leq j \leq d_u - 1} a_{lij} u_j + \sum_{0 \leq j \leq k \leq d_u - 1} b_{lij} u_j u_k \quad (9)$$

for $l = 0, 1, 2$, $i = 0, \dots, d_u - 1$. The coefficient tensors $\mathbf{a}_l, \mathbf{b}_l$ are sparse, allowing a total of at most $3d_u$ non-zero entries. Each non-zero entry is set to be one with probability 0.5, and drawn from $U([-1, 1])$ otherwise.

The initial value $g_i(\mathbf{r})$, the homogeneous spatial second-order term $L_i u_i$, and the source term $s_i(\mathbf{r})$ are generated in the same way as DCR equations, independently for different i 's. Each homogeneous diffusion $L_i u_i$ is allowed to vanish (i.e., $a_i(\mathbf{r}) = 0$) if $b_{1iii} = b_{2iii} = 0$ holds, in which case the two flux functions affecting u_i are linear with respect to u_i itself.

We note that for the case of $d_u = 3$, the two-dimensional Maxwell's equations with homogeneous media and periodic boundaries are included within the distribution of this dataset, including both Transverse Electric (TE) and Transverse Magnetic (TM) forms. That is, for a specific choice of the random coefficients, the specific PDE form becomes the TE form of Maxwell's equations:

$$\begin{aligned} \partial_t E_x &+ \partial_y((-1)H_z) = 0, \\ \partial_t E_y + \partial_x(H_z) &= 0, \\ \partial_t H_z + \partial_x((-1)E_y) &+ \partial_y E_x = 0, \end{aligned}$$

where E_x and E_y are the electric field components, and H_z is the magnetic field component perpendicular to the 2D plane. In this setting, we make the identification $u_0 = E_x$, $u_1 = E_y$, and $u_2 = H_z$.

Similarly, for the TM form, the equations take the specific form:

$$\begin{aligned} \partial_t H_x &+ \partial_y (E_z) = 0, \\ \partial_t H_y + \partial_x ((-1)E_z) &= 0, \\ \partial_t E_z + \partial_x (H_y) &+ \partial_y ((-1)H_x) = 0, \end{aligned}$$

where H_x and H_y are the magnetic field components in the 2D plane, and E_z is the electric field component perpendicular to the plane. In this case, we make the identification $u_0 = H_x$, $u_1 = H_y$, and $u_2 = E_z$.

List of datasets:

- **mvdc_r_2**: The vector \mathbf{u} has dimension $d_u = 2$.
- **mvdc_r_2_0**: Dimension $d_u = 2$. The tensors \mathbf{b}_1 and \mathbf{b}_2 have no non-zero entry, leading to linear flux functions. This makes the dataset easier to learn in pretraining.
- **mvdc_r_3_1**: Dimension $d_u = 3$. The tensor \mathbf{b}_1 has at most one non-zero entry, and same for \mathbf{b}_2 , which increases the probability for Dedalus to successfully generate a solution.
- **mvdc_r_4_0**: Dimension $d_u = 4$. The tensors \mathbf{b}_1 and \mathbf{b}_2 have no non-zero entry.

C.1.4 Divergence-Constrained DCR Equation (DC-DCR)

The PDE system includes $d_u = 2$ equations

$$\begin{aligned} \partial_t u_0 + L_0 u_0 + \mathbf{f}_0(\mathbf{u})_0 + s_0(\mathbf{r}) + \partial_x \mathbf{f}_1(\mathbf{u})_0 + \partial_y \mathbf{f}_2(\mathbf{u})_0 + (-c_0)p + \partial_x p &= 0, \\ \partial_t u_1 + L_1 u_1 + \mathbf{f}_0(\mathbf{u})_1 + s_1(\mathbf{r}) + \partial_x \mathbf{f}_1(\mathbf{u})_1 + \partial_y \mathbf{f}_2(\mathbf{u})_1 + (-c_1)p + \partial_y p &= 0, \end{aligned}$$

and an additional equation

$$\partial_x u_0 + \partial_y u_1 + c_0 u_0 + c_1 u_1 + c_2 = 0$$

that imposes a constraint on the divergence $\nabla \cdot \mathbf{u} = \partial_x u_0 + \partial_y u_1$. The coefficients c_0, c_1 , and c_2 are randomly and independently chosen to be zero, one, or a number from $U([-1, 1])$ with equal probability. If $c_0 = c_1 = 0$ holds, we set $c_2 = 0$ to make it compatible with the periodic domain, leading to the divergence-free condition. In this case, an additional pressure gauge condition $\int_{\Omega} p(t, \mathbf{r}) d\mathbf{r} = 0$ is included during data preparation to ensure uniqueness of solution. Such a pressure gauge is adopted as a convention for all similar PDEs (including INS), and not included in the input of the PDEformer-2 model.

The other settings are shared with MV-DCR equations, including the initial conditions on u_0 and u_1 , the functions $\mathbf{f}_l(\mathbf{u})$, the spatio-temporal domain, and the periodic boundaries. Note that the initial condition of the “pressure” variable p does not need to be specified.

We note that the two-dimensional incompressible Navier-Stokes (INS) equation in conservation form are included within the distribution of this dataset. That is, for a specific choice of the random coefficients, the specific PDE form becomes the INS

equation:

$$\begin{aligned}\partial_t u_0 - a\Delta u_0 + \partial_x(u_0^2) + \partial_y(u_0 u_1) + \partial_x p &= 0, \\ \partial_t u_1 - a\Delta u_1 + \partial_x(u_0 u_1) + \partial_y(u_1^2) + \partial_y p &= 0, \\ \partial_x u_0 + \partial_y u_1 &= 0.\end{aligned}\tag{10}$$

If readers are more familiar with the convection form involving $\mathbf{u} \cdot \nabla \mathbf{u}$, its mathematical equivalence⁸ to the conservation form can be shown using the identity $\nabla \cdot (\mathbf{u}\mathbf{u}^T) = \mathbf{u} \cdot \nabla \mathbf{u} + (\nabla \cdot \mathbf{u})\mathbf{u} = \mathbf{u} \cdot \nabla \mathbf{u}$ when $\nabla \cdot \mathbf{u} = 0$ holds.

List of datasets:

- **dcdcr_icA**: Basic DC-DCR dataset. The initial values $g_0(\mathbf{r}), g_1(\mathbf{r})$ are generated as independent GRFs (8), and are not guaranteed to satisfy the divergence constraint. The initial condition is thus called **arbitrary** (icA) in this sense. The Dedalus solver we utilize will make the solution comply with the divergence constraint automatically.
- **dcdcr_icV**: The initial condition is **valid** (icV), being compatible with the divergence constraint. To achieve this, we first draw a GRF $\psi(\mathbf{r})$ according to (8), and set $\tilde{g}_0(\mathbf{r}) = c_1\psi + \psi_y$, $\tilde{g}_1(\mathbf{r}) = -(c_0\psi + \psi_x)$, in which the differentiation is computed using finite-difference. We then adjust the mean and variance randomly to obtain the ultimate initial values, and reset c_2 to ensure compatibility with them.

C.1.5 Multi-Variable Wave Equation (MV-Wave)

Similar to MV-DCR, the PDE system includes d_u equations and initial conditions, in which the one indexed by $i \in \{0, \dots, d_u - 1\}$ takes the form

$$\partial_{tt} u_i + \mu_i(\mathbf{r}) \partial_t u_i + L_i u_i + \mathbf{f}_0(\mathbf{u})_i + s_i(\mathbf{r}) + \partial_x \mathbf{f}_1(\mathbf{u})_i + \partial_y \mathbf{f}_2(\mathbf{u})_i = 0,$$

$$u_i(0, \mathbf{r}) = g_i(\mathbf{r}), \quad \partial_t u_i(0, \mathbf{r}) = h_i(\mathbf{r})$$

for $t \in [0, 1]$, $\mathbf{r} = (x, y) \in [0, 1]^2$. Each homogeneous spatial second-order term $L_i u_i$ is allowed to vanish (i.e., $a_i(\mathbf{r}) = 0$) if $a_{1ii} = a_{2ii} = b_{1iik} = b_{2iik} = b_{1iki} = b_{2iki} = 0$ holds for all k 's, in which case the two flux functions affecting u_i do not depend on u_i itself. The coefficients are generated as in the Wave equation C.1.2.

List of datasets:

- **mvwave_2**: The vector \mathbf{u} has dimension $d_u = 2$.
- **mvwave_3**: Dimension $d_u = 3$.
- **mvwave_4**: Dimension $d_u = 4$.

C.1.6 Divergence-Constrained Wave Equation (DC-Wave)

Similar to DC-DCR, the PDE system includes $d_u = 2$ equations

$$\begin{aligned}\partial_{tt} u_0 + \mu_0(\mathbf{r}) \partial_t u_0 + L_0 u_0 + \mathbf{f}_0(\mathbf{u})_0 + s_0(\mathbf{r}) + \partial_x \mathbf{f}_1(\mathbf{u})_0 + \partial_y \mathbf{f}_2(\mathbf{u})_0 + (-c_0)p + \partial_x p &= 0, \\ \partial_{tt} u_1 + \mu_1(\mathbf{r}) \partial_t u_1 + L_1 u_1 + \mathbf{f}_0(\mathbf{u})_1 + s_1(\mathbf{r}) + \partial_x \mathbf{f}_1(\mathbf{u})_1 + \partial_y \mathbf{f}_2(\mathbf{u})_1 + (-c_1)p + \partial_y p &= 0,\end{aligned}$$

⁸Here we only consider classical solutions of PDEs, in which case $\mathbf{u}(t, \mathbf{r})$ is sufficiently smooth.

and an additional divergence constraint condition

$$\partial_x u_0 + \partial_y u_1 + c_0 u_0 + c_1 u_1 + c_2 = 0.$$

The other settings are shared with MV-Wave. As the pressure value often exceeds the range $[-10, 10]$, we do not record it in the final dataset as in DC-DCR, so as to make learning easier for our model.

List of datasets:

- **dcwave_icA**: Basic DC-Wave dataset like **dcdcr_icA**. The initial values $g_0(\mathbf{r}), g_1(\mathbf{r}), h_0(\mathbf{r}), h_1(\mathbf{r})$ are generated as independent GRFs (8), and are not guaranteed to satisfy the divergence constraint.
- **dcwave_icV**: The initial values $g_0(\mathbf{r}), g_1(\mathbf{r})$ as well as $h_0(\mathbf{r}), h_1(\mathbf{r})$ are generated as in **dcdcr_icV** to be compatible with the divergence constraint.

C.1.7 Generalized Shallow-Water Equation (G-SWE)

The PDE takes the form

$$\begin{aligned} h_t + L_0 h + \mathbf{f}_0([h; u; v])_0 + s_0(\mathbf{r}) + ((h + H(\mathbf{r}))u)_x + ((h + H(\mathbf{r}))v)_y &= 0, \\ u_t + L_1 u + \mathbf{f}_0([h; u; v])_1 + s_1(\mathbf{r}) + uu_x + vu_y + G_1 h_x &= 0, \\ v_t + L_2 v + \mathbf{f}_0([h; u; v])_2 + s_2(\mathbf{r}) + uv_x + vv_y + G_2 h_y &= 0, \end{aligned}$$

$$h(0, \mathbf{r}) = g_h(\mathbf{r}), \quad u(0, \mathbf{r}) = g_u(\mathbf{r}), \quad v(0, \mathbf{r}) = g_v(\mathbf{r})$$

for $t \in [0, 1]$, $\mathbf{r} = (x, y) \in [0, 1]^2$. Periodic boundary conditions are employed for simplicity.

The initial water height $g_h(\mathbf{r})$ is taken to be a positive random field like the inhomogeneous $a(\mathbf{r})$ of DCR equation, with lower-bound 0.1 and upper-bound 4. The initial velocity $g_u(\mathbf{r}), g_v(\mathbf{r})$ are independent GRFs according to (8). The homogeneous diffusion operator L_i (allowed to vanish) and the source term $s_i(\mathbf{r})$ are generated in the same way as DCR equations, independently for different i 's. The interaction term \mathbf{f}_0 is given in (9), which also appears in the multi-variable equations.

The base water height $H(\mathbf{r})$ can be (1) zero, (2) one, (3) a random positive scalar satisfying $\log_{10} H(\mathbf{r}) \sim U([-3, \log_{10} 4])$. or (4) a positive random field with lower-bound 10^{-3} and upper-bound 4. The probability for the four cases is 5 : 1 : 1 : 5. For $i = 1, 2$, G_i is a random positive scalar that equals one with probability 0.1, and sampled according to $\log_{10} G_i \sim U([-1, 0])$ otherwise.

We note that for a specific choice of the random coefficients, the specific PDE form becomes the regular shallow-water equations:

$$\begin{aligned} h_t + ((h + H(\mathbf{r}))u)_x + ((h + H(\mathbf{r}))v)_y &= 0, \\ u_t - \nu \Delta u + ku + (-F)v + uu_x + vu_y + Gh_x &= 0, \\ v_t - \nu \Delta v + kv + Fu + uv_x + vv_y + Gh_y &= 0, \end{aligned}$$

with kinematic viscosity ν , gravitational acceleration G , viscous drag coefficient k , and Coriolis force coefficient F .

The only dataset is named `swe`.

C.1.8 Steady-State Elasticity Equation

The PDE takes the form

$$\begin{aligned} (\lambda^*(\mathbf{r})(u_x + v_y) + 2\mu(\mathbf{r})u_x)_x + (\mu(\mathbf{r})(u_y + v_x))_y + f_1(\mathbf{r}) &= 0, \\ (\mu(\mathbf{r})(u_y + v_x))_x + (\lambda^*(\mathbf{r})(u_x + v_y) + 2\mu(\mathbf{r})v_y)_y + f_2(\mathbf{r}) &= 0 \end{aligned}$$

for $\mathbf{r} = (x, y) \in [0, 1]^2$. Boundary condition types are randomly chosen from Dirichlet and Neumann, independently for the two variables u, v and the four edges of the square domain. The boundary values are randomly chosen from zero, a random scalar, and a one-dimensional random field.

The plain stress assumption is employed to reduce the 3D elasticity equation to a 2D PDE. Here, $\lambda^*(\mathbf{r})$ and $\mu(\mathbf{r})$ are the Lamé parameters in the 2D plane stress case. These Lamé parameters are related to the Young’s modulus E and the Poisson’s ratio ν by

$$\begin{aligned} \lambda^*(\mathbf{r}) &= \frac{E(\mathbf{r})\nu(\mathbf{r})}{(1 + \nu(\mathbf{r}))(1 - \nu(\mathbf{r}))}, \\ \mu(\mathbf{r}) &= \frac{E(\mathbf{r})}{2(1 + \nu(\mathbf{r}))}. \end{aligned}$$

Each of Young’s modulus $E(\mathbf{r})$ and Poisson’s ratio $\nu(\mathbf{r})$ is randomly chosen from a random positive and a 2D random field. Here, the Poisson’s ratio $\nu(\mathbf{r})$ is constrained to be in the range $[0.01, 1.0]$.

The external force $f_i(\mathbf{r})$ is randomly chosen from zero, a random constant, and a 2D random field.

The only dataset is named `elasticsteady`.

C.2 Specific PDEs

PDEformer-2 is finetuned to solve several specific PDEs as described in Section 2.2. A detailed description of the datasets will be presented in this subsection, including three customized datasets generated by Dedalus [25] and two publicly available datasets.

C.2.1 Sine-Gordon Equation

The PDE takes the form

$$u_{tt} - a\Delta u + (-1)\sin(u) = 0,$$

$$u(0, \mathbf{r}) = g(\mathbf{r}), \quad u_t(0, \mathbf{r}) = h(\mathbf{r})$$

for $t \in [0, 1]$, $\mathbf{r} = (x, y) \in [0, 1]^2$. Periodic boundary conditions along both axes are employed. The initial values $g(\mathbf{r}), h(\mathbf{r})$ are generated as independent GRFs given in (8). The squared velocity $a = c^2$ satisfies $\log_{10} a \sim U([-2, \log_{10} 4])$. We note that this dataset lies within the distribution of the Wave dataset in pretraining (to be more specific, `wave_base`).

Table 5: Summary of the downstream specific PDE datasets, including (1) dataset names, (2) data source, (3) number of time steps used in training (i.e., n_t), (4) input coefficient scalars that may differ across samples (“/” means no such scalars), (5) input coefficient fields, (6) output variables for the model to make predictions, and (7) boundary conditions. The number of testing samples is fixed to 100 for all datasets.

Name	Sine-Gordon	INS-Tracer	INS-Pipe	Wave-Gauss	Wave-C-Sines
Source	by Dedalus	by Dedalus	by Dedalus	PDEGYM [23]	[29]
T-Steps	100	100	100	16	20
Scalars	ν	/	ν	/	/
Fields	g, h	g_u, g_v, g_s	g_u, g_v, s_0, s_1	g, c^2, c	g
Outputs	u	u, v, s	u, v	u	u
BCs	periodic	periodic	no-slip at top & bottom	absorbing at four square edges	Dirichlet at boundary circle

C.2.2 Incompressible Navier-Stokes Equation with Tracer (INS-Tracer)

The PDE takes the form

$$\begin{aligned}
u_t - \nu \Delta u + (u^2)_x + (uv)_y + p_x &= 0, \\
v_t - \nu \Delta v + (uv)_x + (v^2)_y + p_y &= 0, \\
s_t - D \Delta s + (us)_x + (vs)_y &= 0, \\
u_x + v_y &= 0,
\end{aligned}$$

$$u(0, \mathbf{r}) = g_u(\mathbf{r}), v(0, \mathbf{r}) = g_v(\mathbf{r}), s(0, \mathbf{r}) = g_s(\mathbf{r})$$

for $t \in [0, 1]$, $\mathbf{r} = (x, y) \in [0, 1]^2$. Periodic boundary conditions along both axes are employed. The initial values $g_u(\mathbf{r})$, $g_v(\mathbf{r})$, and $g_s(\mathbf{r})$ are generated as independent GRFs given in (8). The fluid viscosity is fixed as $\nu = 10^{-3}$, and the particle diffusivity is fixed as $D = 10^{-2}$. Like DC-Wave equations, we do not record the pressure variable p in the dataset.

Compared with the INS equation (10), an additional variable s representing the tracer particle density is included. This specific PDE therefore lies outside the distribution of the pretraining dataset. However, the interaction between the tracer density s and the fluid velocity u, v is very similar to those appeared in the MV-DCR equations in Section C.1.3, and the PDE can thus be viewed as a new combination of physical mechanisms encountered during pretraining.

Input PDE Forms in Ablation

In the ablation study shown in Figure 11, we use the INS-Tracer data samples to finetune PDEformer-2-fast, but feed PDEs of different forms into the model. For the

equivalent PDE case, the model input is the convection form of the INS-Tracer equation:

$$\begin{aligned} u_t - \nu \Delta u + uu_x + vv_y + p_x &= 0, \\ v_t - \nu \Delta v + uv_x + vv_y + p_y &= 0, \\ s_t - D \Delta s + us_x + vs_y &= 0, \\ u_x + v_y &= 0, \end{aligned}$$

$$u(0, \mathbf{r}) = g_u(\mathbf{r}), v(0, \mathbf{r}) = g_v(\mathbf{r}), s(0, \mathbf{r}) = g_s(\mathbf{r}).$$

For the *incomplete PDE* case, the model input takes the form

$$\begin{aligned} u_t + (u^2)_x + (uv)_y &= 0, \\ v_t + (uv)_x + (v^2)_y &= 0, \\ s_t + (us)_x + (vs)_y &= 0, \end{aligned}$$

$$u(0, \mathbf{r}) = g_u(\mathbf{r}), v(0, \mathbf{r}) = g_v(\mathbf{r}), s(0, \mathbf{r}) = g_s(\mathbf{r}),$$

in which the viscosity and particle diffusivity terms, the pressure variable, and the divergence-free condition are removed. For the *unknown PDE* case, the model input takes the form

$$\begin{aligned} u_t + f_1(u, v, s) &= 0, \\ v_t + f_2(u, v, s) &= 0, \\ s_t + f_3(u, v, s) &= 0, \\ u(0, \mathbf{r}) = g_u(\mathbf{r}), v(0, \mathbf{r}) = g_v(\mathbf{r}), s(0, \mathbf{r}) = g_s(\mathbf{r}), \end{aligned}$$

in which the functions f_1, f_2, f_3 are assumed not to have known mathematical formulations, and the corresponding computational graph is constructed according to Section B.2. For the *wrong PDE* case, the model input is the Lorenz system

$$\begin{aligned} u_t + \sigma v + (-\sigma)u &= 0, \\ v_t + \rho u + (-1)v + (-1)us &= 0, \\ s_t + uv + (-\beta)s &= 0, \end{aligned}$$

$$u(0, \mathbf{r}) = g_u(\mathbf{r}), v(0, \mathbf{r}) = g_v(\mathbf{r}), s(0, \mathbf{r}) = g_s(\mathbf{r}),$$

with coefficients $\sigma = 10$, $\rho = 8/3$, $\beta = 0.8$. Involving no spatial differentiaions, this system actually degenerates to independent ODE systems for different spatial points. Note that all these PDEs are merely inputs of the PDEformer-2 model, and we do not need to obtain their numerical solutions.

C.2.3 Incompressible Navier-Stokes Equation in a Pipe (INS-Pipe)

The PDE takes the form

$$\begin{aligned} u_t - \nu \Delta u + s_0(\mathbf{r}) + (u^2)_x + (uv)_y + p_x &= 0, \\ v_t - \nu \Delta v + s_1(\mathbf{r}) + (uv)_x + (v^2)_y + p_y &= 0, \\ u_x + v_y &= 0, \end{aligned}$$

$$u(0, \mathbf{r}) = g_u(\mathbf{r}), \quad v(0, \mathbf{r}) = g_v(\mathbf{r}).$$

The initial values $g_u(\mathbf{r}), g_v(\mathbf{r})$ and the source terms $s_0(\mathbf{r}), s_1(\mathbf{r})$ are generated as independent GRFs given in (8). The fluid viscosity ν is a random scalar satisfying $\log_{10} \nu \sim U([-3, -2])$. We do not record the pressure variable p in the dataset.

Different from the INS equation (10), the domain $\Omega = [0, 1]^2$ is a periodic pipe along the x -axis, and we impose no-slip boundary conditions $u|_{\Gamma} = v|_{\Gamma} = 0$ on the boundary walls $\Gamma = [0, 1] \times \{0, 1\}$. This specific PDE therefore lies outside the distribution of the pretraining dataset. As homogeneous Dirichlet boundary conditions can appear in the single-variable DCR and wave equations, this can be viewed as a new combination of the interior PDE and boundary conditions.

C.2.4 Wave-Gauss

The *Wave-Gauss* dataset is part of the publicly available PDEGYM [23] dataset series, and we give a brief description of it for convenience to the readers. The PDE is a wave equation of the form

$$u_{tt} - c(\mathbf{r})^2 \Delta u = 0, \\ u(0, \mathbf{r}) = g(\mathbf{r}), \quad u_t(0, \mathbf{r}) = 0$$

for $\mathbf{r} = (x, y) \in \Omega = [0, 1]^2$. The original time interval is different from $[0, 1]$ used in the other datasets. We rescale the time variable t to resolve this, and the wave velocity values $c(\mathbf{r})$ are scaled accordingly.

The domain Ω has absorbing boundaries. To inform PDEformer-2 of this, we add the Mur boundary condition

$$(u_t + c(\mathbf{r}) \partial_n u)|_{\partial\Omega} = 0,$$

into the PDE input for the model during finetuning.

Both the initial value $g(\mathbf{r})$ and the wave velocity field $c(\mathbf{r})$ are generated as linear combinations of Gaussian densities of the form $\exp(-\|\mathbf{r} - \mathbf{r}_i\|_2^2 / 2\sigma_i^2)$. This is very different from the GRF and its variants employed in the pretraining dataset.

The solutions are recorded on 16 equispaced timesteps (including the initial value at $t = 0$) within the temporal domain. This differs from the 101 timesteps used in the previous datasets we generated ourselves. Following the convention of the authors, we train the models with normalized data, making the entire dataset have zero mean and unit variance. The form of the PDE input does not need to be adapted accordingly, since the wave equation is linear, and the linearly transformed solutions still solve the PDE.

C.2.5 Wave-C-Sines

The *Wave-C-Sines* dataset released by Mousavi et al. [29] considers the wave equation on a disk with radius 1. The wave velocity is 2, and the system evolves to the terminal time 0.2. After a spatio-temporal rescaling operation to fit our domain, the PDE takes the form

$$u_{tt} - 0.01 \Delta u = 0, \\ u(0, \mathbf{r}) = g(\mathbf{r}), \quad u_t(0, \mathbf{r}) = 0$$

for $t \in [0, 1]$, $\mathbf{r} = (x, y) \in \Omega = D((0.5, 0.5); 0.5)$, with Dirichlet boundary condition $u|_{\partial\Omega} = 0$. The initial condition $g(\mathbf{r})$ is generated as a superposition of sinusoidal terms, with coefficients decaying slowly as the frequency increases. This makes it more oscillatory than the GRFs in our pretraining dataset.

The solutions are recorded on 16,431 uniformly sampled points inside the disk, which is different from the polar-coordinate-based grids in the pretraining disk datasets illustrated in Figure 21c. To fit the CNN-based function encoder of PDEformer-2 as well as the branch network of DeepONet (CNN), we interpolate the initial condition to the 128×128 uniform grid before feeding it into the network. Solution interpolation is avoided, since to ensure a fair error metric against the ground-truth labels, we may need to interpolate the Cartesian predictions back to scattered points, which consumes computational resources. Ignoring the initial frame, a total of 20 equispaced time steps are predicted by the models. As the solutions in the original dataset have a small magnitude, they are multiplied by 100 to better fit the neural networks, and the linear PDE preserves its form as in Wave-Gauss.

C.3 Inverse Problems

C.3.1 Inverse Problems on DCR Equations

In inverse problems, including recovering scalar coefficients, system identifications, and recovering source fields, the PDEs have the same form as shown in Section C.1.1 despite some differences in the coefficients. The source term $s(\mathbf{r})$ is set to a GRF (scalar is no longer allowed), the diffusivity coefficient $a(\mathbf{r})$ is set to a scalar with distribution $\log_{10} a(\mathbf{r}) \sim U([-3, -2])$ (i.e., homogeneous case), and the parameter J is set to zero, meaning that no sinusoidal term is included in the PDE. For convenience, we apply periodic boundary conditions along both axes. For each PDE, we fix the PDE form and parameters, and solve it with 25 different initial conditions. The observations of these solutions are used for inverse problems. The initial conditions are generated as independent GRFs given in (8).

C.3.2 Inverse Problems on Wave Equations

The PDEs follow the same form as shown in Section C.1.2 despite some differences in the coefficients. The source term $s(\mathbf{r})$ is set to a GRF (scalars no longer allowed), the squared velocity field $a(\mathbf{r})$ is set as in the inhomogeneous case, and the parameter J is set to zero, meaning that there is no sinusoidal term in the PDE. For convenience, we apply periodic boundary conditions along both axes. For each equation, we fix the PDE structure, scalar coefficients, and the damping term $\mu(\mathbf{r})$, and solve it under 100 different initial conditions and source terms. The resulting solution observations are then used to formulate inverse problems. The initial conditions are generated as independent Gaussian random fields (GRFs) as described in (8).

C.4 Classical Solvers and Data Grids

Wave-Gauss and Wave-C-Sines are publicly available datasets. We generate the steady-state elasticity dataset using the FEniCSx [26] package, a classical solver based

on finite-element method. All the remaining datasets mentioned in this section are generated by Dedalus V3 [25] based on spectral methods. Unless specified otherwise, the spatial solution domain is discretized into 128×128 grid points.

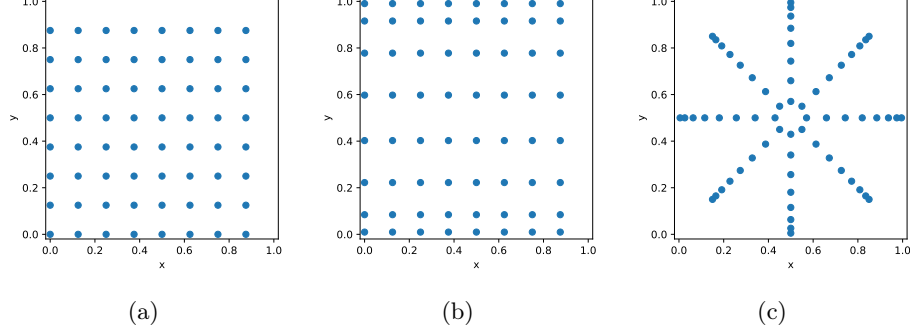


Fig. 21: Dedalus solution grids for different computational domains Ω . For illustrative purposes, the resolution is 8×8 instead of 128×128 in the real datasets. (a) $\Omega = [0, 1]^2$ is periodic along both axes. (b) $\Omega = [0, 1]^2$ is periodic along the x -axis. (c) $\Omega = D((0.5, 0.5); 0.5)$ is a disk, in which the solution grids are based on polar coordinates.

As illustrated in Figure 21, Dedalus uses different solution grids for different computational domains Ω . Based on spectral methods, Dedalus employs a uniform grid along the periodic axis. For the non-periodic axis, the grid points cluster quadratically towards the endpoints of the spatial interval. The FEniCSx solver uses a uniform 128×128 grid with triangular elements for the steady-state elasticity equation.

Since PDEformer-2 employs an INR to decode mesh-free solutions, we can utilize solution samples recorded on different grid points directly during training, and no interpolation is required. Indeed, the input coefficient fields need to be given on uniform grids to fit the CNN function encoder. These fields, based on GRFs, are directly generated and stored on the uniform grids in our datasets, and interpolation is only required in the data preparation stage to specify the discretized initial values. No interpolation is applied in the training stage.

Snapshots of time-dependent PDE solutions are recorded with a time stepsize $\delta t_{\text{data}} = 0.01$, yielding a total of 101 time steps for each data sample. For the three specific PDE datasets generated by Dedalus, we ignore the initial time-step ($t = 0$) in the solution label during model training, since the MindSpore implementation of FNO3D requires an even grid resolution along each axis. Indeed, Dedalus may need to proceed with a smaller time stepsize to ensure numerical stability. If Dedalus fails to provide a solution for the PDE, or if any recorded variable u in the generated solution does not satisfy $\|u\|_{L^\infty} \leq 10$, we shall discard the corresponding data sample, and not include it in the final dataset.

D Training Settings and Further Results

D.1 Pretraining

Dynamic Data Buffer

Pretraining is executed using the deep learning framework MindSpore⁹, on a machine with 8 NPUs, 192 CPU cores, 768GB of RAM, and a local disk with about 3TB storage. The entire pretraining dataset stored on the remote large disk has a size of about 40TB, which does not fit into the capacity of our local disk. In order to resolve this, we maintain a data buffer in the local disk, which contains about 50 data files (with 1k samples in each file). Each pretraining “epoch” only traverses the data samples stored in this buffer. In parallel to training, new data files are downloaded from the remote disk, and will replace the existing files in the local buffer after downloading is completed.

Continual Learning

The large diverse dataset took a relatively long time for us to prepare (including PDE design, coding, and solver execution). We decide not to postpone our pretraining until the entire dataset is ready. Instead, we train the model with all the data available at the moment, and prepare new data in the mean time. When new data is prepared, we load the previous model weights, and improve it using the extended dataset. This procedure is repeated for over ten times, with each incremental training run for about one or two days. We did not keep a detailed track of the pretraining history. However, we conjecture according to our experience that, if the complete pretraining data is prepared at the beginning, we shall only need five to ten days of pretraining to achieve the same level of model performance.

The capability of being continuously improved with more data could be an important feature of a PDE foundation model in practice.

More Settings

Each incremental training stage during pretraining runs from 200 to 500 “epochs” with batch size 80 (10 per device). The Adam optimizer [31] without weight decay is used, clipping the gradient to a maximal norm of 1. The maximum learning rate is selected as 10^{-4} in the early stages and 6×10^{-5} for the rest of stages. Learning rate is linear warmed-up in the first 10 “epochs”, and decays following a cosine schedule afterwards. Before training starts, we preprocess data by constructing the computational graph for the specific PDE forms of the data samples, and storing the information in separate files.

Assuming the reference solution (of a single variable) u^{ref} is recorded on the spatio-temporal points $\{(t_i, \mathbf{r}_i) \mid i \in \mathcal{I}\}$. During evaluation, the model accuracy is measured by the normalized root mean square error (nRMSE)

$$\text{nRMSE}(\hat{u}, u^{\text{ref}}) = \frac{\sqrt{\frac{1}{|\mathcal{I}|} \sum_{i \in \mathcal{I}} (\hat{u}(t_i, \mathbf{r}_i) - u^{\text{ref}}|_i)^2}}{\epsilon + \sqrt{\frac{1}{|\mathcal{I}|} \sum_{i \in \mathcal{I}} (u^{\text{ref}}|_i)^2}}, \quad (11)$$

⁹<https://www.mindspore.cn/>

in which the small constant $\epsilon = 10^{-6}$ is included to prevent division by zero. Two-dimensional PDE solutions often involve a lot of discretization points (typically $101 \times 128 \times 128$ for our pretraining dataset), leading to a considerable computational cost for our INR decoder that deals with each grid point independently. Therefore, to reduce the computational cost, the training loss is taken to be a Monte-Carlo estimate of (11). Specifically, we randomly sample $K = 8192$ independent indices $i_k \sim U(\mathcal{I}), k = 1, \dots, K$, and take

$$\text{nRMSE}(\hat{u}, u^{\text{ref}}; \{i_k\}) = \frac{\sqrt{\frac{1}{K} \sum_{k=1}^K (\hat{u}(t_{i_k}, \mathbf{r}_{i_k}) - u^{\text{ref}}|_{i_k})^2}}{\epsilon + \sqrt{\frac{1}{K} \sum_{k=1}^K (u^{\text{ref}}|_{i_k})^2}} \quad (12)$$

as the training loss. Following our previous PDEformer-1 [24], the small constant is increased to $\epsilon = 0.05$ to stabilize training. For PDEs with n_v variables, the loss is computed for one variable at a time, and a data sample is used n_v times in every training “epoch”.

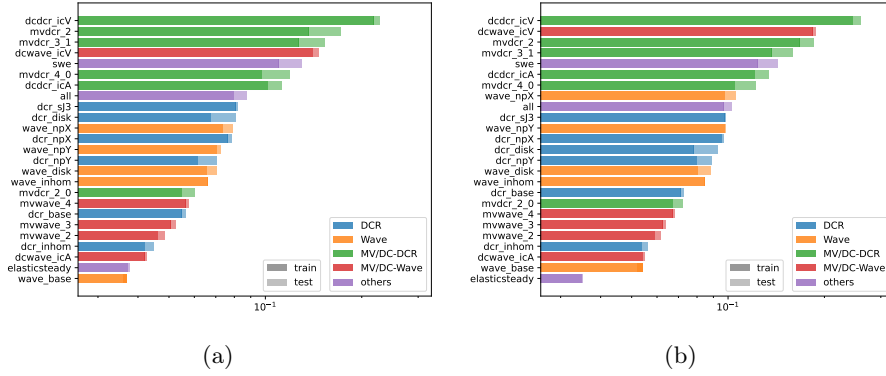


Fig. 22: Detailed model accuracy (nRMSE) on the pretraining dataset, including (a) PDEformer-2-base and (b) PDEformer-2-fast models.

Detailed Dataset Accuracies

Figure 22 shows the detailed model accuracy (measured by (11)) post pretraining. Each test dataset contains 1k samples. Although most of the training datasets contain more than 100k samples, we only use the first 1k samples to compute the mean nRMSE for each dataset, since the entire dataset does not fit into the capacity of our local disk.

Diagnosis of Large Solution Discrepancy

When PDEformer-2 predictions deviate significantly from Dedalus solutions on in-distribution PDEs, we may identify two possible causes: (1) PDEformer-2 does not generalize well to this case, (2) Dedalus itself produces non-physical patterns as

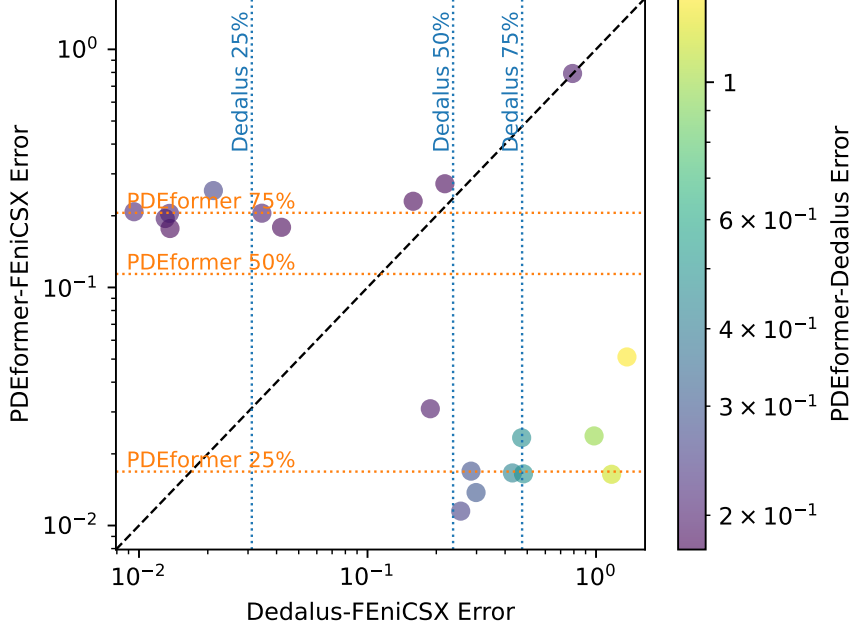


Fig. 23: Scatter plot of nRMSE compared with FEniCSx solutions on the 20 selected cases where Dedalus and PDEformer-2-base predictions deviate significantly. Point color stands for the nRMSE between the Dedalus solution and the PDEformer-2 prediction.

mentioned in Section 2.1. To make an investigation of this, we focus specifically on the DCR (more accurately, `dcr_base`) dataset, and select the 20 samples exhibiting the largest nRMSE (PDEformer-2-base v.s. Dedalus) from the test set (with 1000 samples in total). We regenerate the solutions using the FEniCSx solver, and employ them as the new reference solutions to compute the nRMSE. According to Figure 23, for the 10 samples with the largest solution discrepancies (with point color ranging from yellow to blue), the error is more likely attributed to the unreliable solutions produced by Dedalus (case (2)), since most of the points are located in the lower-right corner of the figure. As for the remaining 10 samples with relatively smaller discrepancies (points in purple), the error tends to originate from the inefficient generalization of PDEformer-2, as most of the points lie in the upper-left part. Our results indicate that, although a neural solver typically exhibits a certain level of generalization error for most cases, the worst-case performance could potentially be superior to its teacher solver, since the model inductive bias can prevent it from producing highly non-physical predictions. Such extreme-case reliability might be crucial in some real scenarios. Indeed, we acknowledge that the above investigation is still limited. More sufficient and rigorous validation of the model would be necessary for future deployment in real applications.

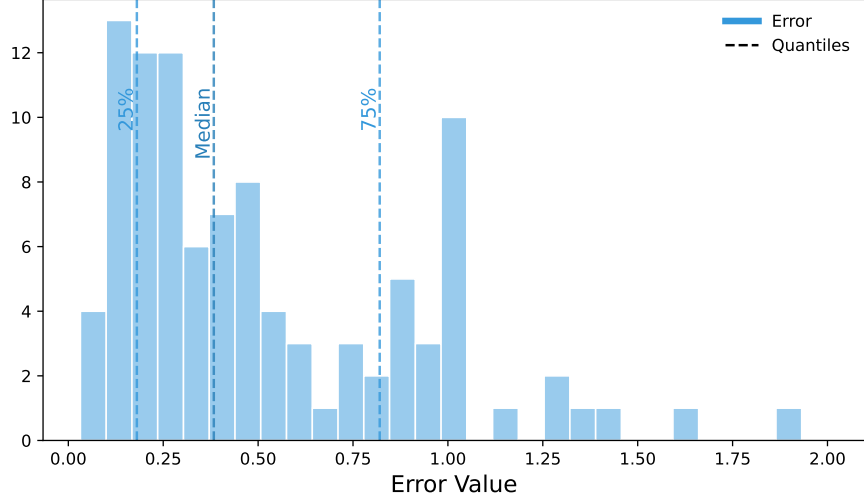


Fig. 24: Histogram of PDEformer-2-base prediction nRMSE compared with FEniCSx solutions on 100 failure cases of Dedalus.

More about Failure Cases of the Teacher Solver. We have mentioned in Section 2.1 that Dedalus fails to solve some PDEs during pretraining data generation. To make a further investigation of these cases, we collect a total of 100 such failure cases when generating the `dcr_base` dataset, and compare PDEformer-2-base predictions against the new reference solution provided by FEniCSx. As can be seen in the histogram in Figure 24, PDEformer-2 can generalize to some of the cases, but the overall performance would seem unsatisfactory.

D.2 Baseline Experiments on Specific PDEs

If not specified otherwise, all experiments on specific PDEs uses MindSpore, with a maximum learning rate of 10^{-4} for the Adam optimizer. We use 8 NPUs with batch size 40 (5 per device) for 80 or more training samples, and a single NPU otherwise, with batch size 5 for 20 samples, 2 for 4 samples. For the baseline models, all solution components are predicted concurrently, so the evaluation nRMSE (11) takes into account the entire solution. This is different from PDEformer-2, which computes (11) independently for different solution components, and then take the average to obtain the final prediction error. The training loss (12) is computed in a similar way, with the grid point sampling applied only to PDEformer-2 and DeepONets. The remaining optimization settings are shared with pretraining.

For the two baseline foundation models, Poseidon and MPP, we use the official PyTorch implementation adapted for GPUs. Finetuning starts from the official pretrained model weights. Note that Poseidon and MPP do not predict the entire spatio-temporal solution directly in a single inference. For Poseidon, we feed the initial

value into the model, and let it predict all the system states afterwards, so a trajectory with n_t time snapshots will be used $n_t - 1$ times in each epoch. Its finetuning is executed on 8 GPUs with batch size 24. For MPP, we randomly select two consequent snapshots from each trajectory to train the model, with the former snapshot serving as model input and the latter as the output label. Each trajectory is used 2.5 times in average in every “epoch”. The finetuning uses a single GPU with batch size 10. As less hardware resources are used to finetune MPP, we divide its time consumption by 8 before preparing Figure 10. The remaining configurations for finetuning are the same as in the original implementation.

Training or finetuning runs for 1k epochs, except for the Poseidon (200 epochs) and MPP (500 “epochs”) results in Figure 9 as their special training strategy leads to a longer epoch time. To avoid showing results with overfitting, we compute the test accuracy (11) for every 50 epochs, and record the best value. Indeed, the more rigorous approach against overfitting would involve an independent validation set. The early-stopping time should be determined using this validation set, and the best model weights is then applied to the test set to obtain the final accuracy. However, it is found empirically that the errors on the validation set and the test set are close, and the two approaches would produce similar results. We thus decided to adopt the simpler approach to complete the experiments, and this applies to all models involved.

Geo-FNO runs on a single GPU using the official PyTorch implementation. For each model, the software and hardware platforms used remain consistent in all the experiments involved, including few-shot adaptation, adaptation speed, and prediction speed. When we assess the prediction speed of PDEformer-2, the *INR as Output* setting only requires to produce the embedding vectors μ_j^ℓ mentioned in Section A.1.2 (i.e., forward propagation of the graph Transformer), without making any spatio-temporal queries for the INR decoder that follows.

D.3 Inverse Problems

D.3.1 Recovering Scalar Coefficients

In this task, we consider diffusion-convection-reaction equations mentioned in Section C.3.1.

We use the PSO algorithm with population size of 100 and a maximum generation of 200 to solve the corresponding optimization problem. Experiments are conducted on a single NPU (same for all experiments on inverse problems). We also conduct experiments with different noise levels, the number of spatio-temporal locations, and the number of initial conditions for the PDE, with the results given in Figure 25–28. From these experiments, we can conclude that PDEformer-2 is robust and adaptable to noise and various settings in inverse problems.

D.3.2 System Identification

As a complement to the main text, we present in Table 6 the complete results of the system identification experiments. All coefficients were initialized to zero, and the identification was performed using the Particle Swarm Optimization (PSO) algorithm with a swarm size of 150 and a maximum of 150 iterations. The table compares the

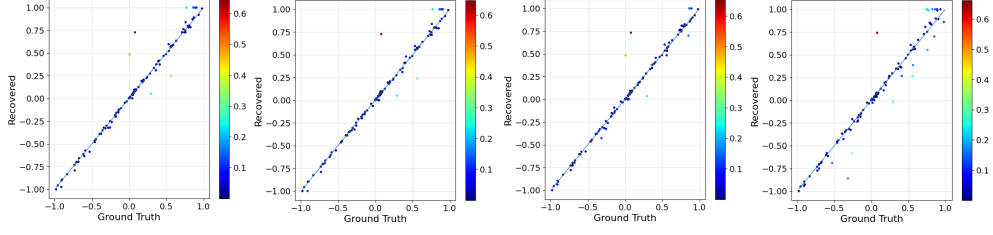


Fig. 25: Results of the scalar coefficient recovery problem under varying noise levels added to the initial conditions. The noise levels are set at 1%, 3%, 10%, and 30%, respectively.

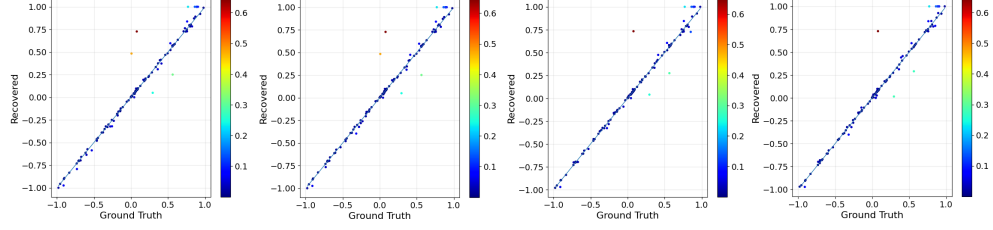


Fig. 26: Results of the scalar coefficient recovery problem under varying noise levels added to the observations. The noise levels are set at 1%, 3%, 10%, and 30%, respectively.

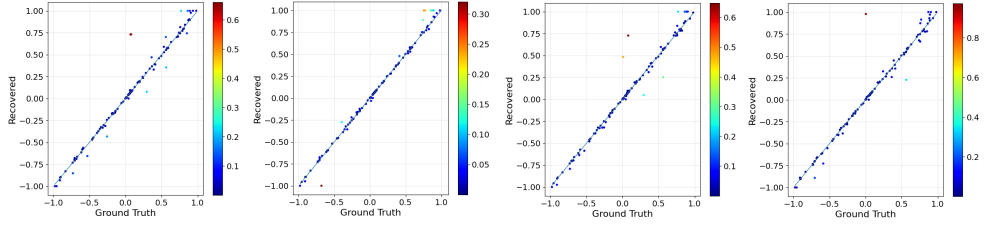


Fig. 27: Results of the scalar coefficient recovery problem with varying numbers of observation points. The spatio-temporal points are set at 32×5 , 64×10 , 128×20 , and 256×40 , respectively.

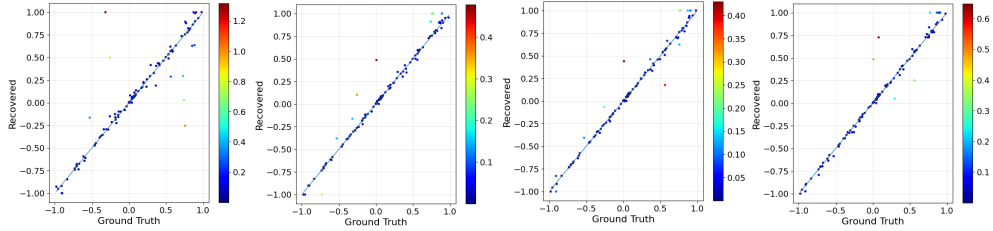


Fig. 28: Results of the scalar coefficient recovery problem with varying numbers of observable solutions. The numbers of solutions are 1, 5, 10, and 25, respectively.

Table 6: Results of system identification, including the ground-truth (GT) and recovered coefficients. We mark the zero coefficients that are mistakenly recovered as non-zero (with absolute value over the threshold 0.1) in bold.

	a	c_{01}	c_{02}	c_{03}	c_{11}	c_{12}	c_{13}	c_{21}	c_{22}	c_{23}
GT	0.007	-0.376	0.000	0.000	1.000	1.000	1.000	-0.732	0.000	0.000
Rec.	0.007	-0.536	0.087	0.484	1.000	1.000	1.000	-0.726	0.012	0.020
GT	0.009	-0.187	1.000	1.000	-0.110	0.000	0.237	1.000	1.000	0.995
Rec.	0.009	-0.172	1.000	1.000	-0.103	0.018	0.245	1.000	1.000	1.000
GT	0.005	0.000	0.884	0.000	0.181	0.000	1.000	0.008	1.000	0.879
Rec.	0.007	0.089	1.000	0.086	0.185	-0.026	1.000	0.016	1.000	0.898
GT	0.002	1.000	0.000	0.412	0.128	0.000	0.000	0.061	1.000	-0.005
Rec.	0.004	1.000	-0.009	1.000	0.254	0.099	-1.000	-0.029	1.000	0.683
GT	0.069	1.000	0.729	-0.317	0.000	0.196	1.000	-0.118	1.000	0.000
Rec.	0.083	1.000	0.760	-1.000	-0.019	0.213	1.000	-0.129	1.000	0.060
GT	0.001	0.000	0.825	0.000	0.000	1.000	1.000	1.000	1.000	0.000
Rec.	0.001	-0.174	1.000	0.694	0.006	1.000	1.000	1.000	1.000	0.001
GT	0.002	1.000	0.000	0.980	1.000	1.000	0.000	0.000	0.000	1.000
Rec.	0.429	1.000	0.090	0.999	1.000	1.000	1.000	0.044	0.061	0.830
GT	0.038	0.592	0.000	0.000	1.000	1.000	0.000	0.000	-0.169	1.000
Rec.	0.020	1.000	-0.092	-1.000	1.000	1.000	-0.033	0.016	-0.183	0.937
GT	0.003	1.000	1.000	0.000	1.000	0.000	0.788	-0.708	1.000	-0.145
Rec.	0.003	1.000	1.000	0.093	1.000	-0.013	0.791	-0.699	1.000	-0.248
GT	0.083	1.000	1.000	0.759	0.000	0.000	-0.978	1.000	-0.183	1.000
Rec.	0.081	1.000	1.000	1.000	-0.002	0.001	-0.980	1.000	-0.193	1.000

ground-truth (GT) coefficients with the recovered values (Rec.), demonstrating the algorithm’s ability to approximate a wide range of coefficient configurations across different PDE instances.

D.3.3 Recovering Source Fields

In this task, we still consider equations mentioned in Section C.3.1, with the goal of recovering the source term $s(\mathbf{r})$. For the optimization problem 2, we set $\lambda = 0.01$, choose the regularization term as $\mathcal{R}(s) = \|\nabla s\|_2$, and use the Adam optimizer [31] with a learning rate of 0.1 for 150 iterations. The initial guess of $s(\mathbf{r})$ is taken to be a zero field. To fit into the CNN function encoder of PDEformer-2, we discretize $s(\mathbf{r})$ on a grid with resolution 128×128 , and treat the grid values as independent variables during the optimization process. Spatial derivatives in the regularization term is computed using finite difference.

D.3.4 Recovering Wave Velocity Fields

In this task, we consider wave equations mentioned in Section C.3.2. Still considering the optimization problem (2), we take $\lambda = 0.001$, $\mathcal{R}(a) = \|\nabla a\|_2$ and use the Adam optimizer with a learning rate of 0.02 for 20000 iterations. In the experiments, it is found that the optimization may converge to local minima in some cases. We resolve this issue by running independent optimizations with different initializations, and take

the best result as the final prediction. Specifically, for $k = 1, 2, \dots, 9$, the velocity field is initialized as $a_k^{\text{init}}(\mathbf{r}) = 0.4k$ (a constant without spatial dependency), and the optimization terminates at \hat{a}_k . The final prediction is taken as $\hat{a} = \hat{a}_K$ with $K = \arg \min_{k=1, \dots, 9} \mathcal{L}(a_k)$.

E Visualizations

In this section, we present additional visualizations of PDEformer-2’s performance across different datasets, including those given in Supplementary Information C and not shown in the main text. These include predicted solutions, ground-truth, and the corresponding error maps. For time-dependent equations, snapshots are shown at $t = 0, 0.33, 0.67$, and 1.0 to capture the temporal evolution. These visualizations highlight PDEformer-2’s ability to accurately model the underlying dynamics of the equations.

E.1 DCR Equation

We consider the DCR equation on different domains, including a square domain periodic along both axes, periodic only along y -axis, periodic only along x -axis, as well as a disk-shaped domain. The visualizations for these cases are shown in Figures 29, 30, 31, and 32 respectively.

E.2 Wave Equation

We consider the wave equation on a square domain with periodic boundary conditions along both axes, periodic along y -axis, periodic along x -axis, and a disk domain with randomly generated boundary conditions. The visualizations for these cases are shown in Figures 33, 34, 35, and 36 respectively.

E.3 Multi-Variable DCR Equation

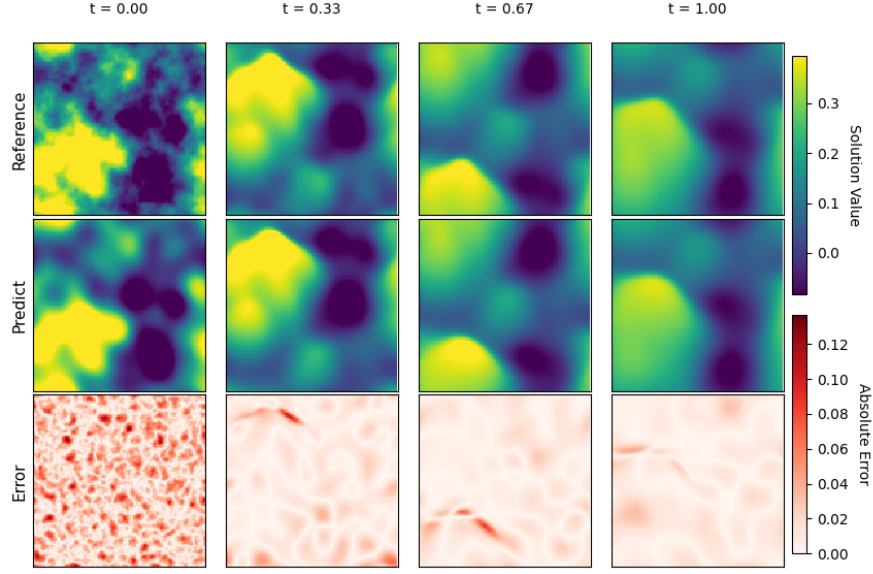
We consider the multi-variable DCR equation on a square domain that is periodic along both axes. Visualization of the variables u_0, u_1 is shown in Figure 37.

E.4 Divergence-Constrained DCR Equation

We consider the divergence-constrained DCR equation on a square domain periodic along both axes, including those with initial conditions satisfying and violating the divergence constraint. Numerical results for valid (satisfying the divergence constraint) initial conditions are shown in Figure 38, while cases with arbitrary (violating the divergence constraint) initial conditions are visualized in Figure 39.

E.5 Multi-Variable Wave Equation

We consider the multi-variable wave equation on a square domain periodic along both axes and only two variables for convenience. Visualization of the solution components u_0, u_1 is shown in Figure 40.



$$u_t - a \nabla \cdot (a \nabla u) + u^3 + (c_{21} u + u^3)_y = 0$$

Fig. 29: Visualization of the DCR Equation on a square domain with periodic boundary conditions along both axes.

E.6 Divergence-Constrained Wave Equation

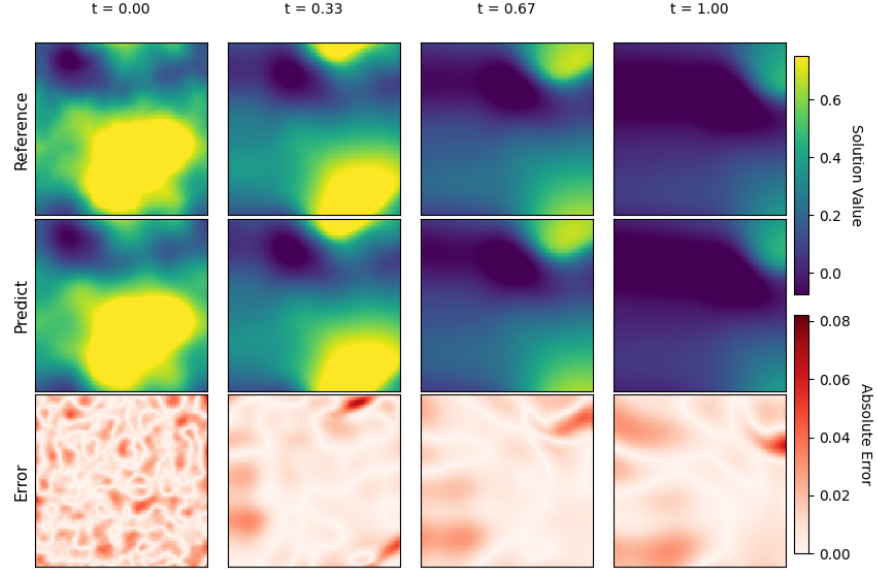
We consider the divergence-constrained wave equation on a square domain periodic along both axes, including those with initial conditions satisfying and violating the divergence constraint. Numerical results for valid initial conditions are shown in Figure 41, while cases with arbitrary initial conditions are visualized in Figure 42.

E.7 Generalized Shallow Water Equation

We consider the generalized shallow water equation on a square domain periodic along both axes. The visualization of the solution components h, u, v is shown in Figure 43.

E.8 Sine-Gordon Equation

We consider the sine-Gordon equation on a square domain periodic along both axes, and train the models using 900 data samples. Visualization of the solution is shown in Figure 44.



$$\begin{cases} u_t - a\Delta u + s + c_{01}u + c_{02}u^2 + (c_{11}u)_x + (c_{21}u + c_{23}u^3)_y = 0, \\ \partial_n u|_{\Gamma_R} = 0, \\ (\partial_n u + a_L(r)u)|_{\Gamma_L} = 0. \end{cases}$$

Fig. 30: Visualization of the DCR equation on a square domain periodic along y -axis.

E.9 INS-Tracer

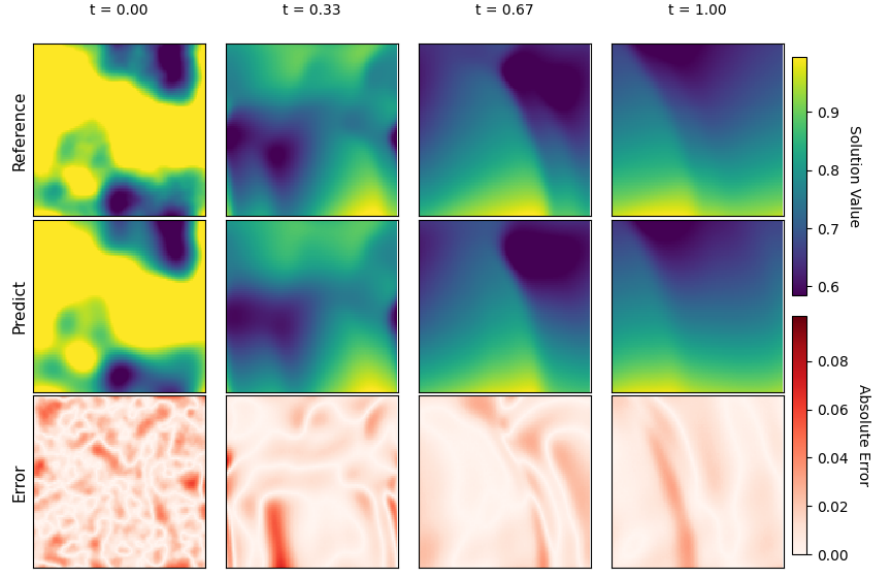
We consider the Incompressible Navier-Stokes Equation with Tracer on a square domain periodic along both axes, and train the models using 80 data samples. Visualization of the variables u, v, p on the last timestep ($t = 1$) is shown in Figure 45.

E.10 INS-Pipe

We consider the Incompressible Navier-Stokes Equation in a pipe on a square domain periodic along x -axis, and train the models using 900 data samples. Visualization of the variables u, v at the last timestep ($t = 1$) is shown in Figure 46.

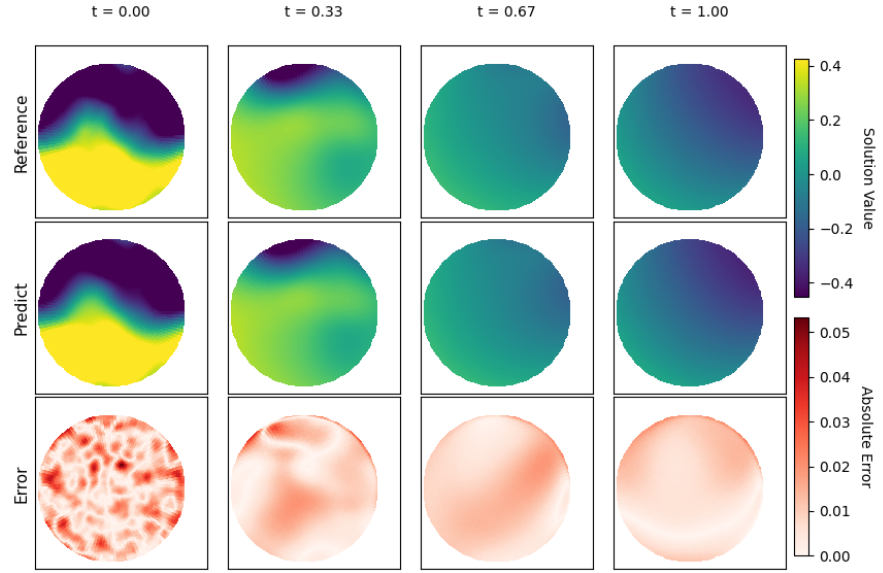
E.11 Wave-Gauss

We consider the wave equation with Gaussian initial conditions on a square domain with absorbing boundaries, and train the models using 80 data samples. Visualization of the solution is shown in Figure 47.



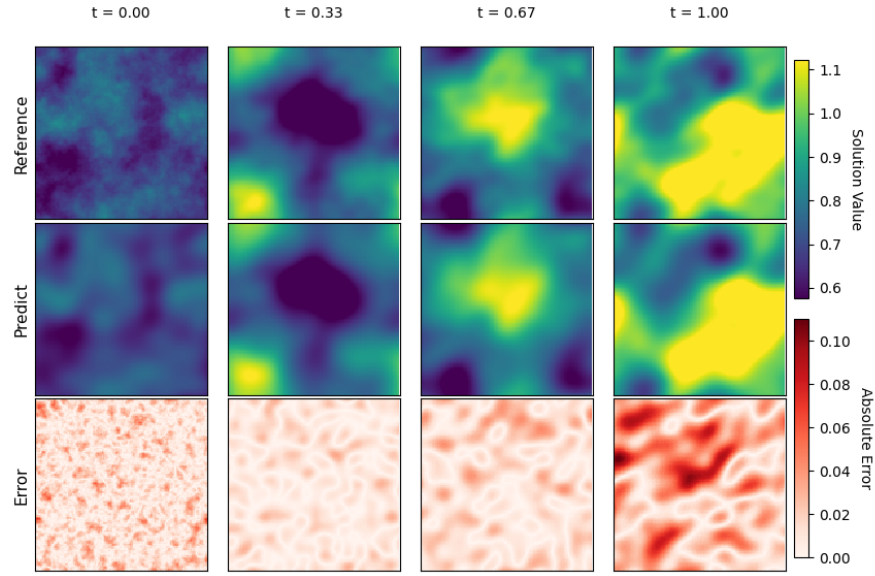
$$\begin{cases} u_t - a \nabla \cdot (a \nabla u) + c_{02} u^2 + u^3 + (u + c_{13} u^3)_x + (c_{21} u + u^2 + c_{23} u^3)_y = 0, \\ \partial_n u|_{\Gamma_U} = 0, \\ (\partial_n u + a_D(r)u + c_D)|_{\Gamma_D} = 0 \end{cases}$$

Fig. 31: Visualization of the DCR equation on a square domain periodic along x -axis.



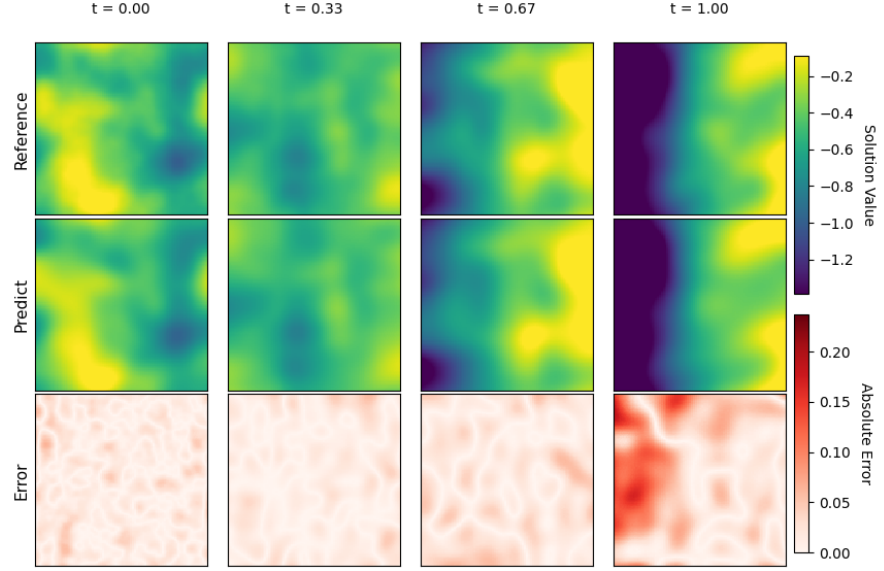
$$\begin{cases} u_t - a \nabla \cdot (a \nabla u) + 1 + c_{01}u + u^2 + u^3 + (u + c_{13}u^3)_x + u_y = 0, \\ (u + \partial_n u + c_O)|_{\Gamma_O} = 0 \end{cases}$$

Fig. 32: Visualization of the DCR equation on a disk domain.



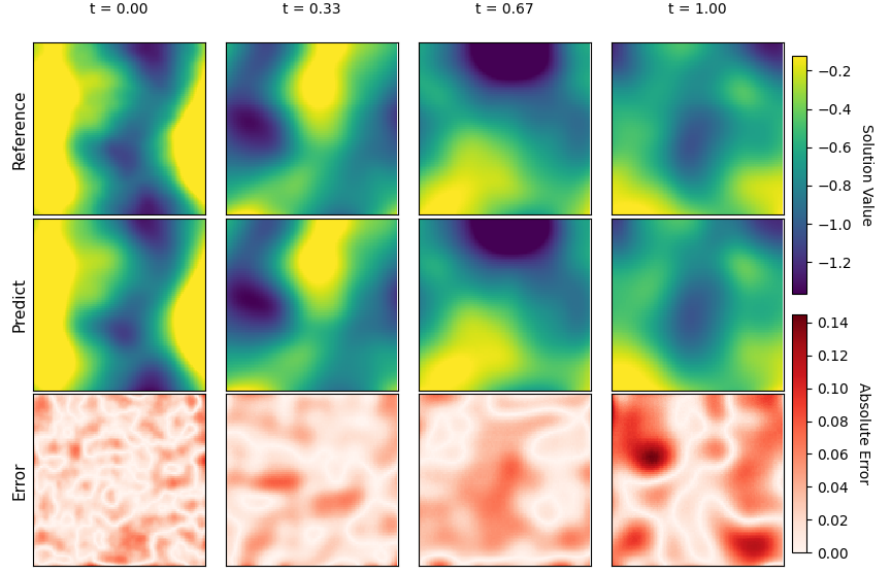
$$u_{tt} - \Delta u + c_{02}u^2 + (c_{11}u + c_{12}u^2 + c_{13}u^3)_x + (c_{22}u^2 + c_{23}u^3)_y = 0$$

Fig. 33: Visualization of the wave equation on a square domain periodic boundary along both axes.



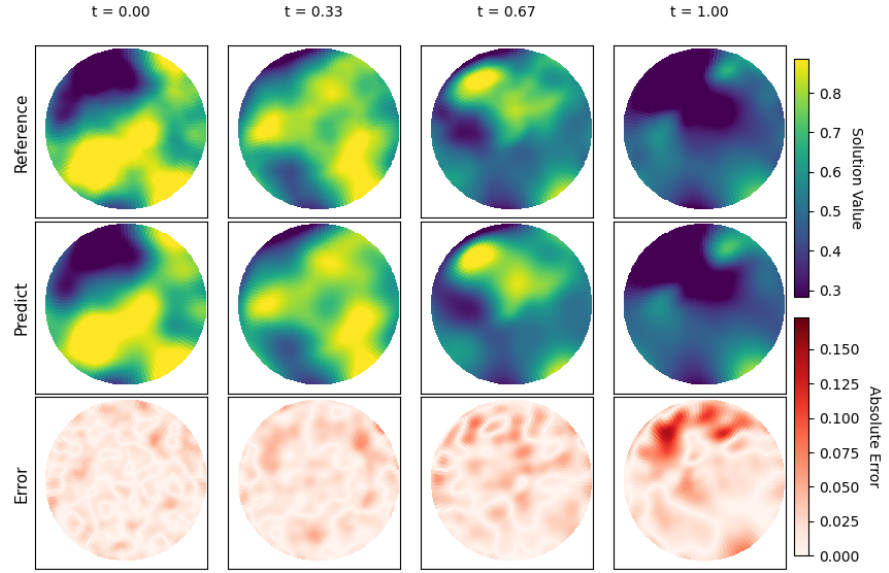
$$\begin{cases} u_{tt} - a\Delta u + c_{001}u + c_{002}u^2 + c_{003}u^3 + (u^3)_x \\ + (c_{201}u + u^2 + c_{210}\cos(c_{211}u + c_{212}u^2))_y = 0 \\ (\partial_n u + u)|_{\Gamma_R} = 0, \\ (u + b_L\partial_n u + c_L)|_{\Gamma_L} = 0 \end{cases}$$

Fig. 34: Visualization of the wave equation on a square domain periodic along y -axis.



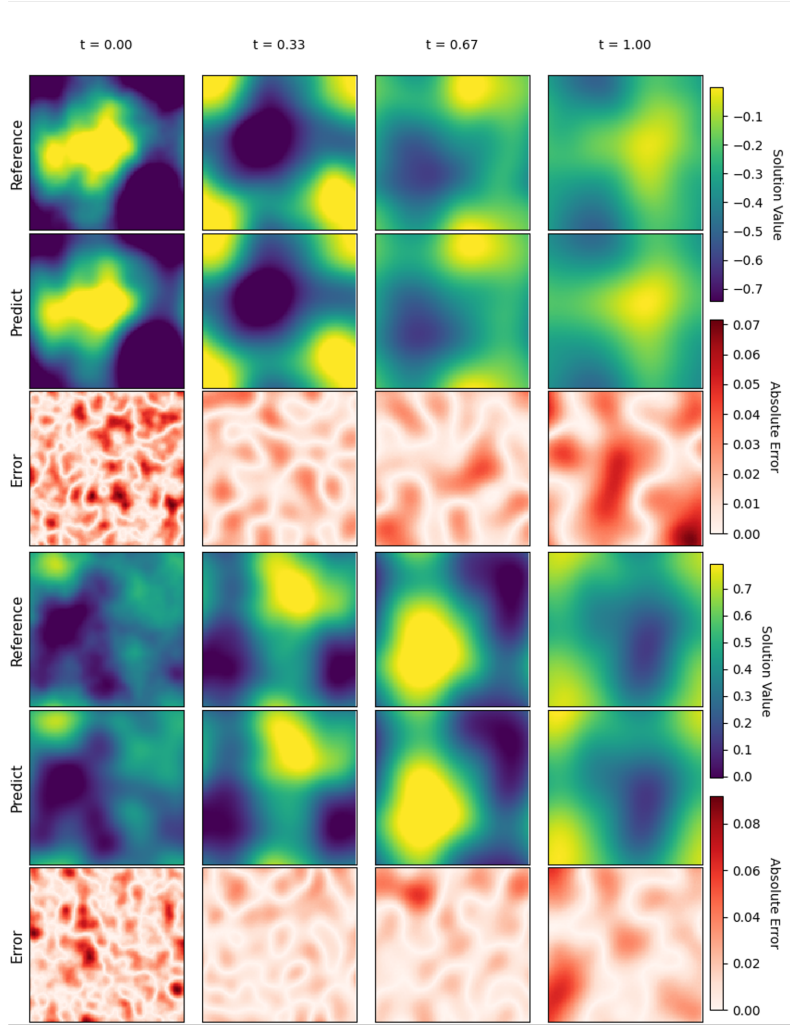
$$\begin{cases} u_{tt} + \mu(r)u_t - a\Delta u + s(r) + c_{001}u + u^2 + (u + c_{102}u^2 + c_{103}u^3)_x \\ + (u^2 + \sin(c_{211}u + c_{212}u^2) + \cos(u^2))_y = 0 \\ (\partial_n u + a_U u + c_U)|_{\Gamma_U} = 0, \\ (\partial_t u + a_D u + b_D \partial_n u)|_{\Gamma_D} = 0 \end{cases}$$

Fig. 35: Visualization of the wave equation on a square domain periodic along x -axis.



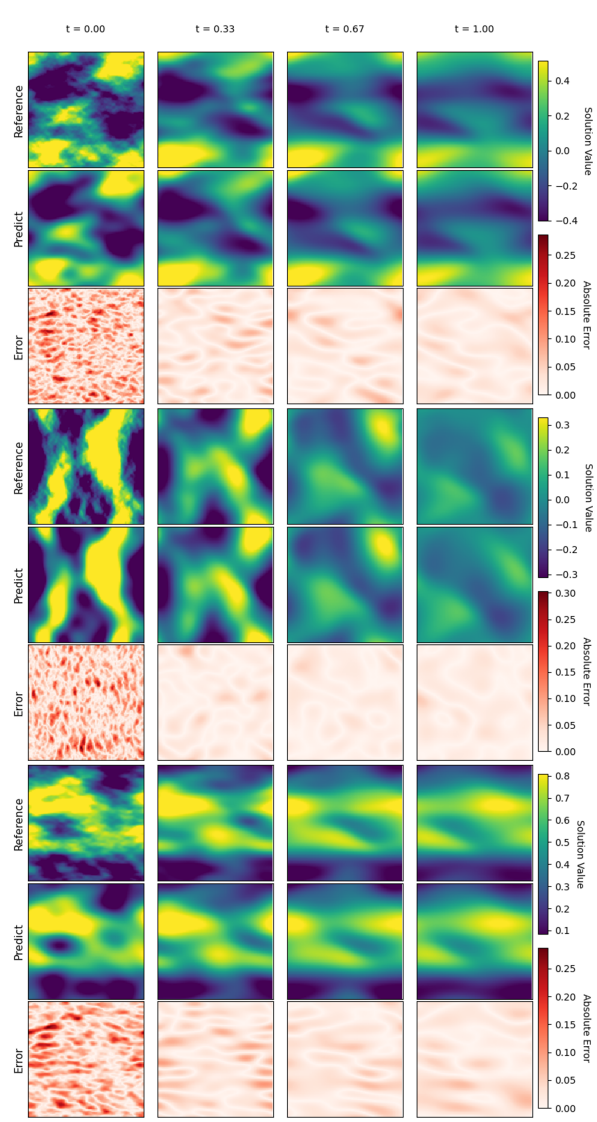
$$\begin{cases} u_{tt} + u_t - a \nabla \cdot (a \nabla u) + u^3 + (c_{11}u + c_{12}u^2 + c_{13}u^3)_x + (c_{22}u^2 + u^3)_y = 0 \\ (\partial_t u + a_O u)|_{\Gamma_O} = 0 \end{cases}$$

Fig. 36: Visualization of the wave equation on a disk domain.



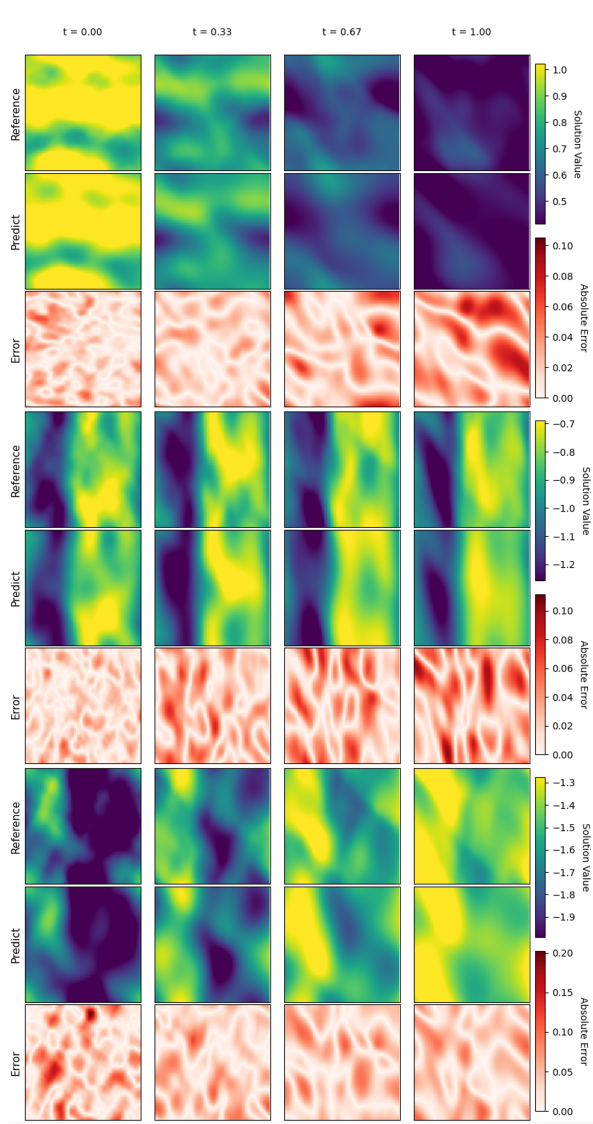
$$\begin{cases} \partial_t u_0 + c_{001} u_1 + u_0 + \partial_x(u_0 + u_1) + \partial_y(u_1) - a_0 \Delta u_0 = 0, \\ \partial_t u_1 + u_1 + u_0 + \partial_x(c_{111} u_1 + u_0) + \partial_y(u_0) + s_1(r) - \nabla \cdot (a_1 \nabla u_1) = 0 \end{cases}$$

Fig. 37: Visualization of the multi-variable DCR equation on a square domain that is periodic along both axes, including all solution components u_0, u_1 .



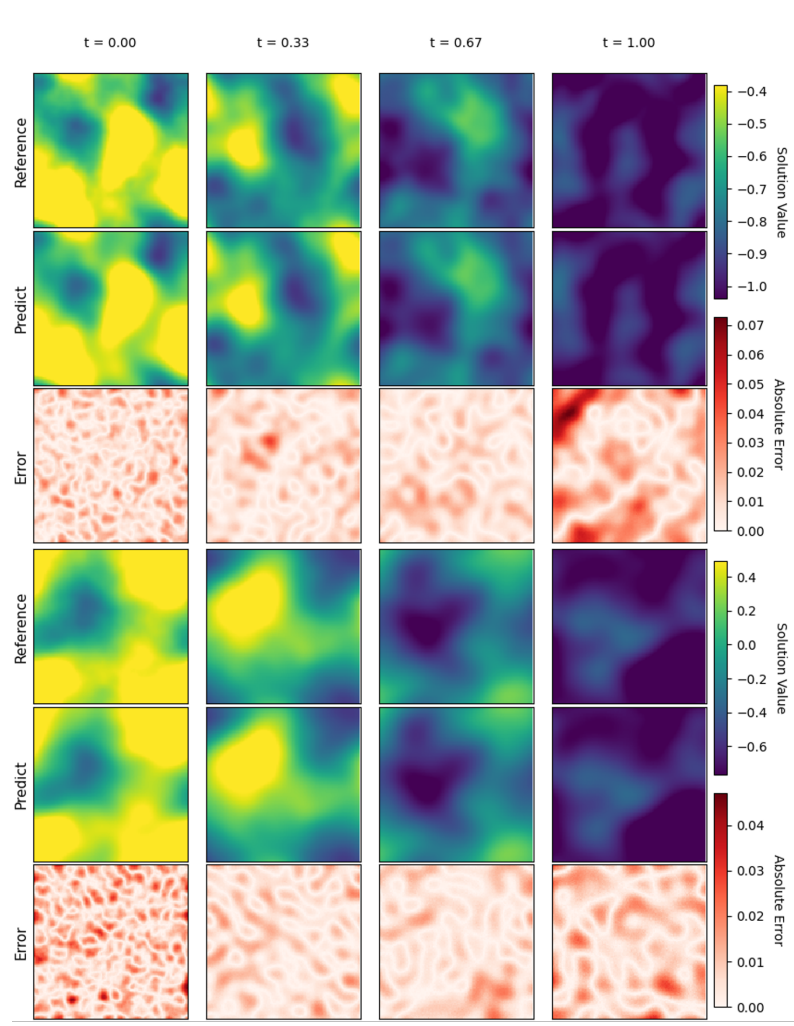
$$\begin{cases} \partial_t u_0 + u_1 + \partial_x(c_{100}u_0 + c_{101}u_1) + \partial_y(c_{201}u_1) \\ -a_0 \nabla \cdot (a_0 \nabla u_0) + \partial_x p = 0, \\ \partial_t u_1 + u_1 + c_{010}u_0 + \partial_x(c_{111}u_1 + c_{110}u_0) + \partial_y(u_0 + b_{2101}u_0u_1) \\ +s_1(r) - \nabla \cdot (a_1 \nabla u_1) + \partial_y p + (-c_1)p = 0, \\ \partial_x u_0 + \partial_y u_1 + c_1 u_1 = 0 \end{cases}$$

Fig. 38: Visualization of the divergence-constrained DCR equation on a square domain periodic along both axes and initial conditions satisfying the divergence constraint.



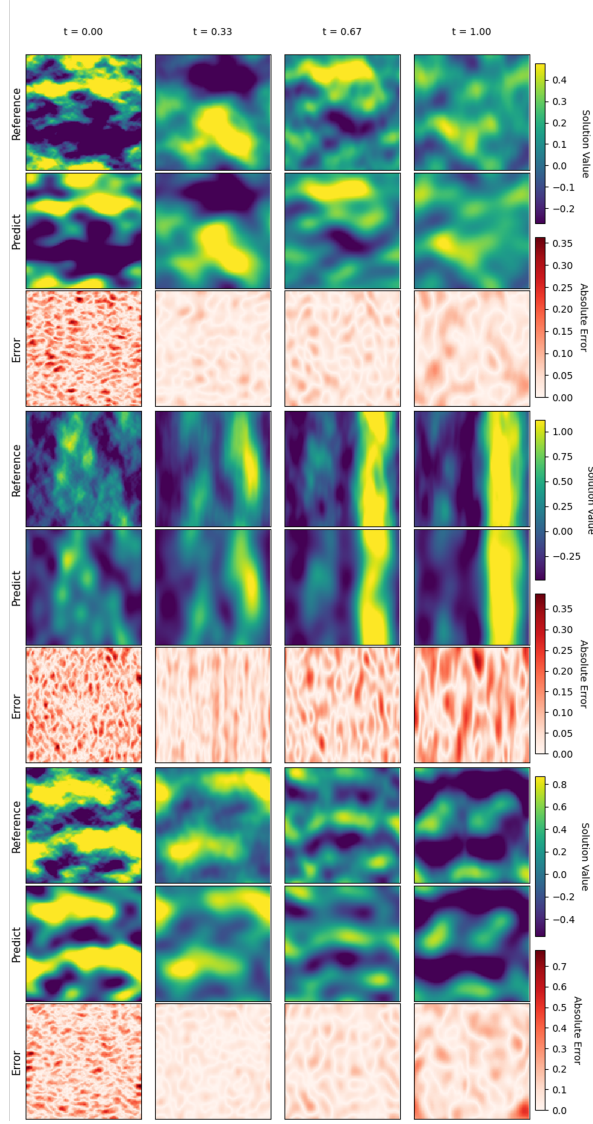
$$\begin{cases} \partial_t u_0 + u_0 + c_{001}u_1 + \partial_x(u_0 + u_0u_1 + u_0^2) + \partial_y(c_{200}u_0 + u_1^2) \\ -a_0 \nabla \cdot (a_0 \nabla u_0) + \partial_x p = 0, \\ \partial_t u_1 + c_{010}u_0 + c_{011}u_1 + \partial_x(u_1^2) + \partial_y(u_0 + u_0u_1) + s_1 + \partial_y p - p = 0, \\ \partial_x u_0 + \partial_y u_1 + u_1 + c_2 = 0 \end{cases}$$

Fig. 39: Visualization of the divergence-constrained DCR equation on a square domain periodic along both axes and initial conditions violating the divergence constraint.



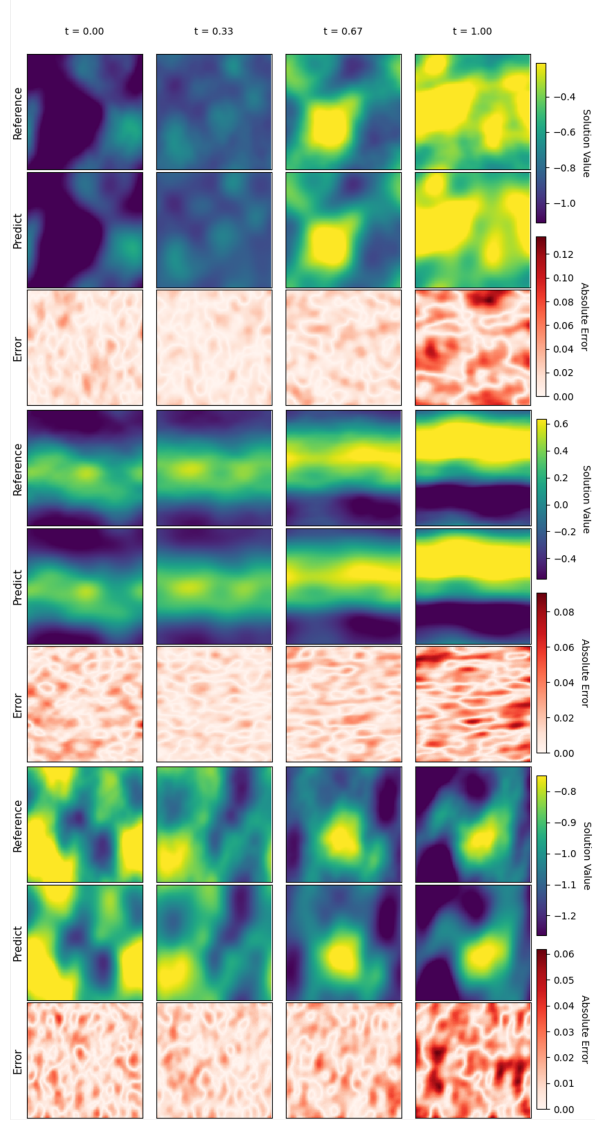
$$\begin{cases} \partial_{tt}u_0 + \mu_0\partial_tu_0 + u_1 + c_{000}u_0 + b_{0001}u_0u_1 + \partial_x(u_0 + u_1) + \partial_y(c_{200}u_0 + u_0u_1) \\ + s_0 - a_0\Delta u_0 = 0, \\ \partial_{tt}u_1 + \mu_1\partial_tu_1 + u_1 + c_{010}u_0 + \partial_y(b_{2100}u_0^2) - a_1\nabla \cdot (a_1\nabla u_1) = 0 \end{cases}$$

Fig. 40: Visualization of the multi-variable wave equation on a square domain periodic along both axes, including all solution components u_0, u_1 .



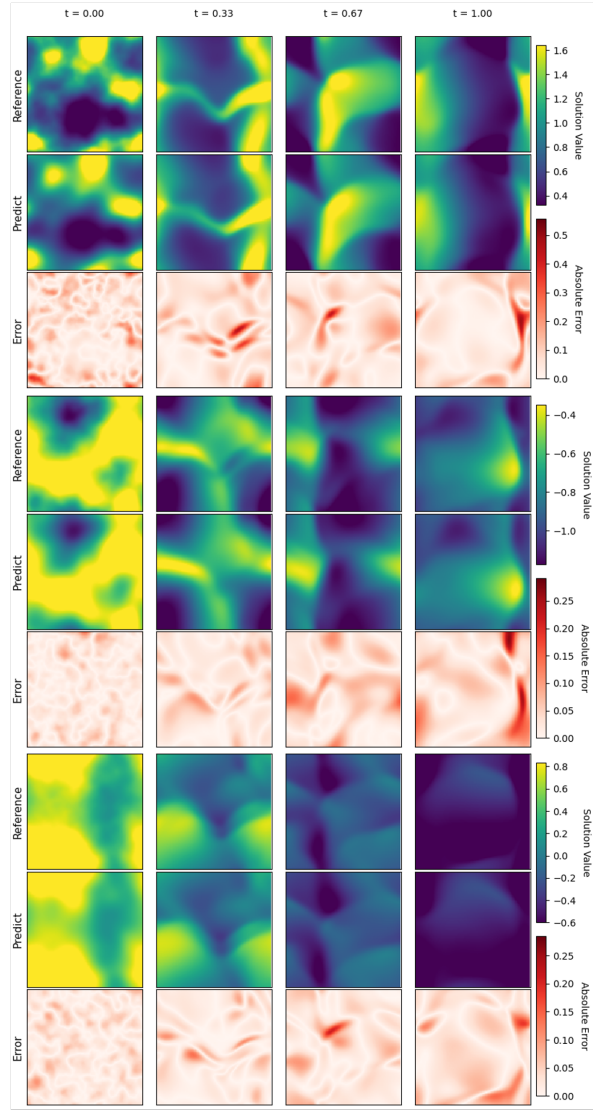
$$\begin{cases} \partial_{tt}u_0 + \mu_0(r)\partial_t u_0 + u_0 + \partial_x(u_0 + u_1^2 + u_0^2) + \partial_y(u_0 + u_1) \\ -a_0 \nabla \cdot (a_0 \nabla u_0) + \partial_x p + (-c_0)p = 0, \\ \partial_{tt}u_1 + \mu_1 \partial_t u_1 + u_1^2 + \partial_x(b_{1101}u_0 u_1 + b_{1100}u_0^2) + \partial_y(u_0 + c_{211}u_1) \\ -a_1 \Delta u_1 + \partial_y p + (-c_1)p = 0, \\ \partial_x u_0 + \partial_y u_1 + c_0 u_0 + c_1 u_1 = 0 \end{cases}$$

Fig. 41: Visualization of the divergence-constrained wave equation on a square domain periodic along both axes and initial conditions satisfying the divergence constraint.



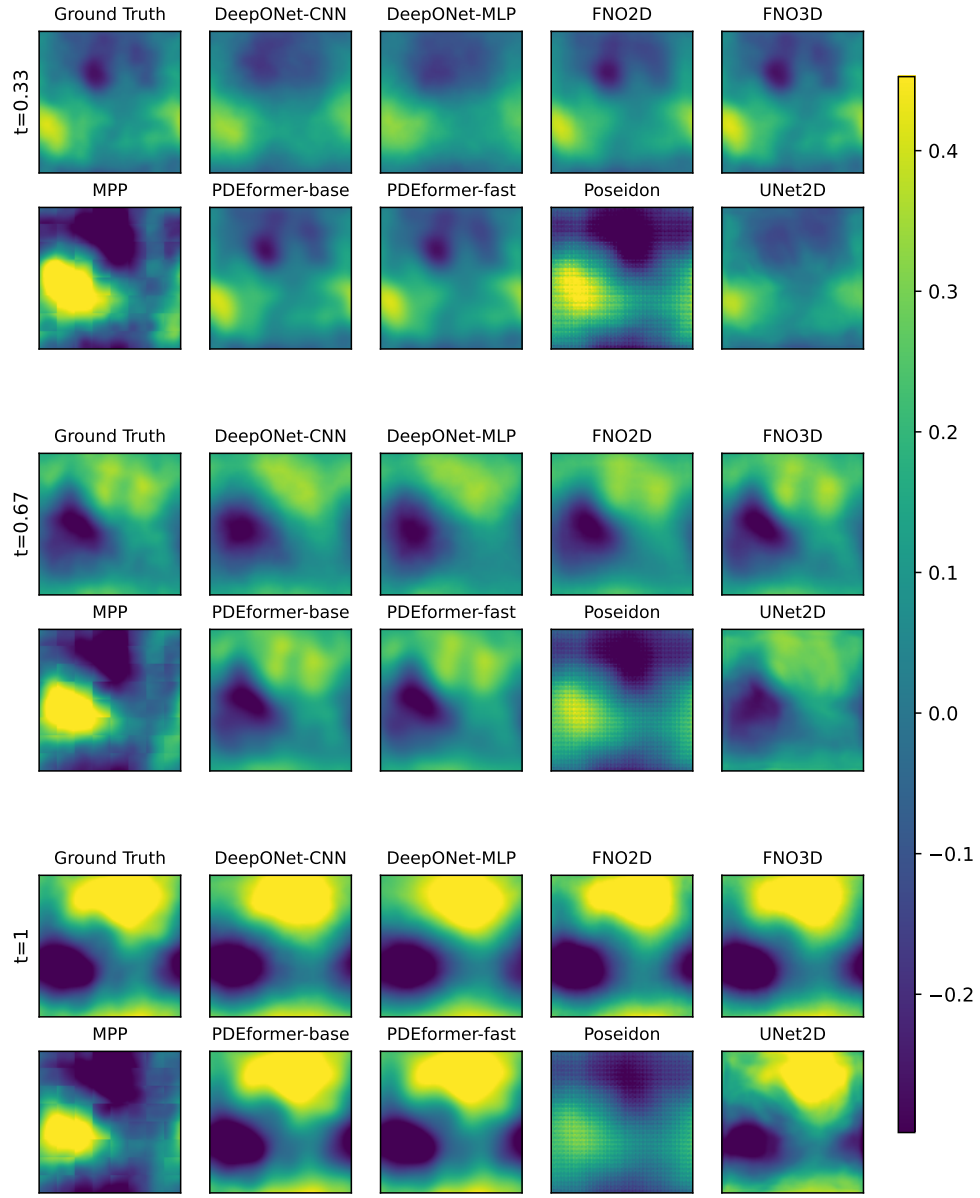
$$\begin{cases} \partial_{tt}u_0 + \mu_0(r)\partial_t u_0 + u_0 + b_{0001}u_0u_1 + b_{0011}u_1^2 + \partial_x(c_{100}u_0 + u_1) \\ + \partial_y(u_0 + c_{201}u_1 + b_{2001}u_0u_1) + s_0 - \nabla \cdot (a_0 \nabla u_0) + \partial_x p + (-c_0)p = 0 \\ \partial_{tt}u_1 + c_{010}u_0 + \partial_x(c_{111}u_1 + c_{110}u_0) + \partial_y(c_{210}u_0 + b_{2101}u_0u_1) \\ - \nabla \cdot (a_1 \nabla u_1) + \partial_y p + (-c_1)p = 0 \\ \partial_x u_0 + \partial_y u_1 + c_0 u_0 + c_1 u_1 + 1 = 0 \end{cases}$$

Fig. 42: Visualization of the divergence-constrained wave equation on a square domain periodic along both axes and initial conditions violating the divergence constraint.



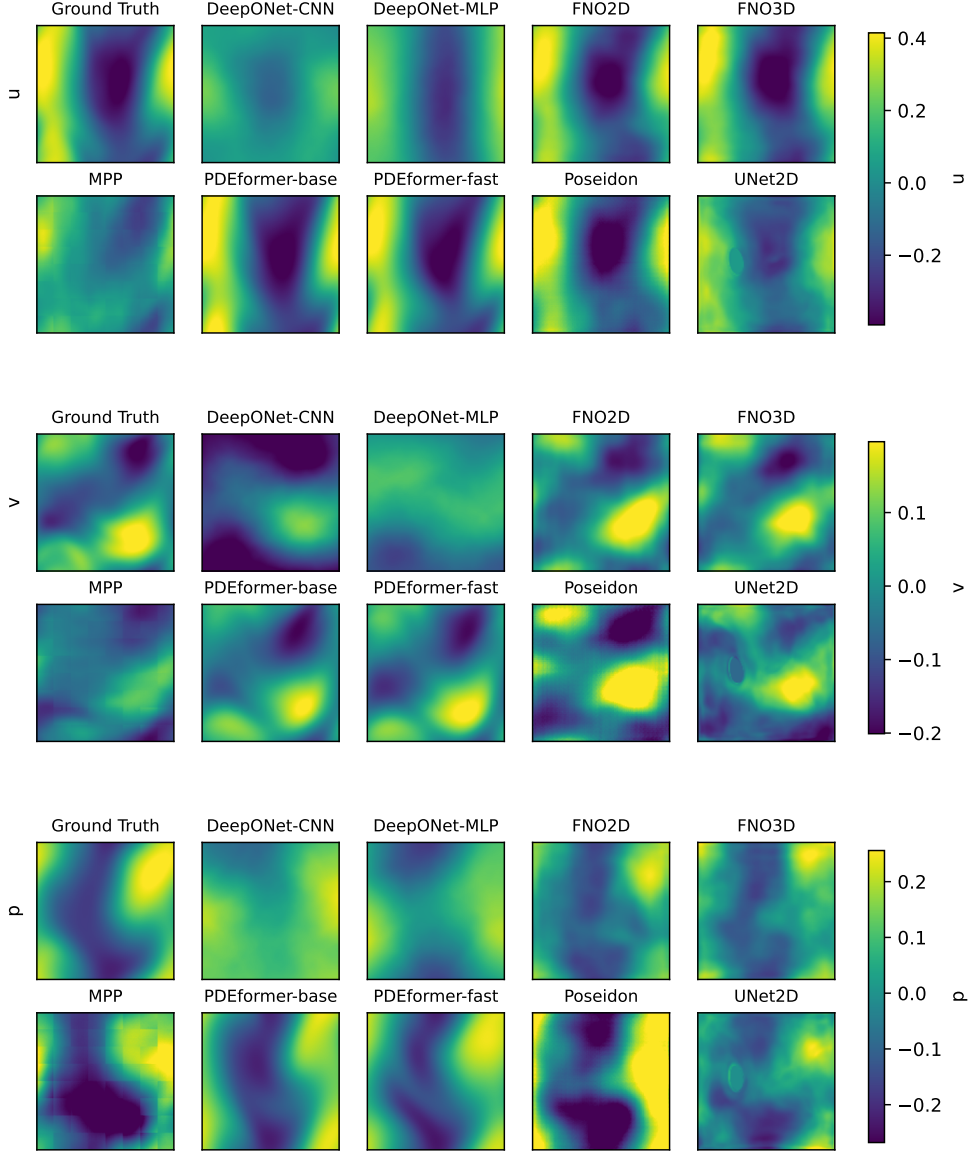
$$\begin{cases} h_t + ((h + H)u)_x + ((h + H)v)_y - a^h \Delta h + s^h(r) + c_{02}v + u = 0, \\ u_t + uu_x + vv_y + g_1 h_x - a^u \Delta u + s^u(r) + v + c_{10}h = 0, \\ v_t + uv_x + vv_y + g_2 h_y - a^v \Delta v + 1 + c_{20}h + c_{22}v + b_{201}hu = 0 \end{cases}$$

Fig. 43: Visualization of the generalized shallow water equation on a square domain periodic along both axes, including all solution components h, u, v .



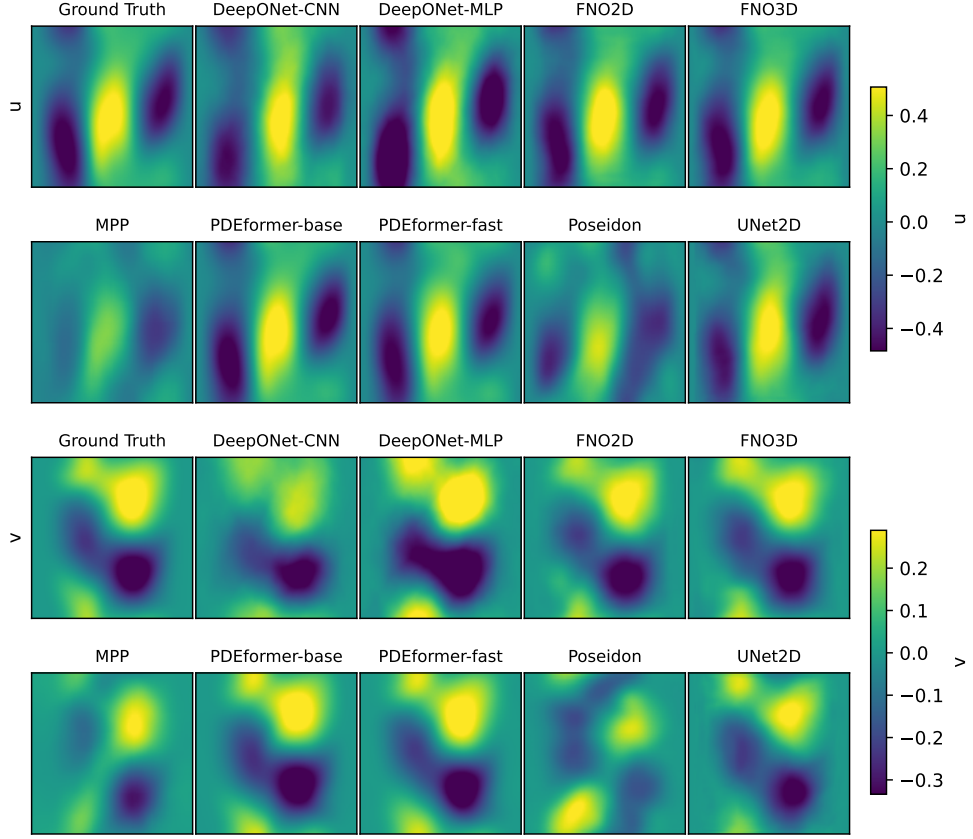
$$u_{tt} - a\Delta u + (-1)\sin(u) = 0$$

Fig. 44: Visualization of the Sine-Gordon equation on a square domain periodic along both axes.



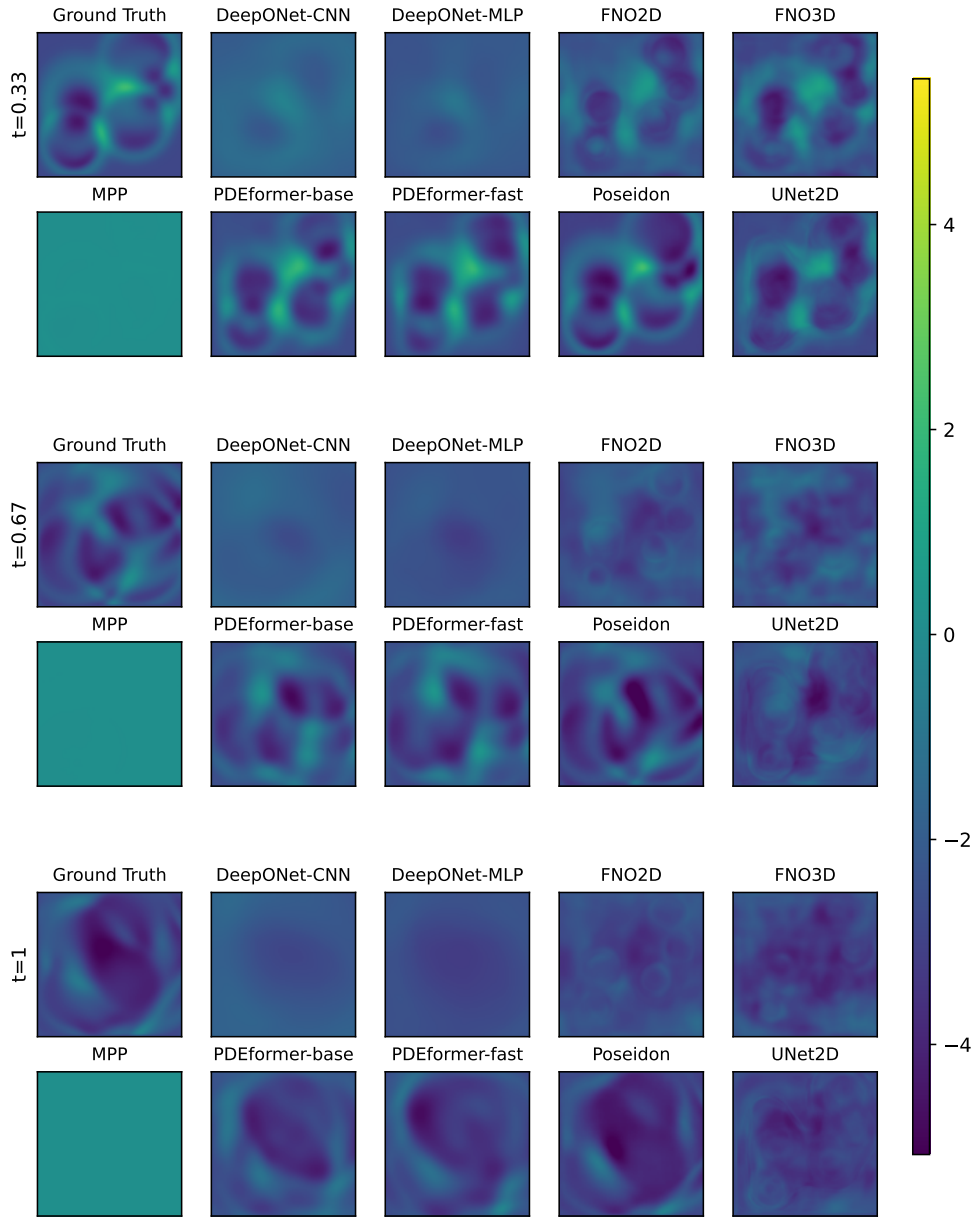
$$\begin{cases} u_t - \nu \Delta u + (u^2)_x + (uv)_y + p_x = 0, \\ v_t - \nu \Delta v + (uv)_x + (v^2)_y + p_y = 0, \\ s_t - D \Delta s + (us)_x + (vs)_y = 0, \\ u_x + v_y = 0 \end{cases}$$

Fig. 45: Visualization of the incompressible Navier-Stokes equation with tracer particle (INS-Tracer) on a square domain periodic along both axes, showing the solution components u, v, p at $t = 1$.



$$\begin{cases} u_t - \nu \Delta u + s_0(\mathbf{r}) + (u^2)_x + (uv)_y + p_x = 0, \\ v_t - \nu \Delta v + s_1(\mathbf{r}) + (uv)_x + (v^2)_y + p_y = 0, \\ u_x + v_y = 0, \end{cases}$$

Fig. 46: Visualization of the incompressible Navier-Stokes equation in a pipe (INS-Pipe), showing the solution components u, v at $t = 1$.



$$u_{tt} - c(\mathbf{r})^2 \Delta u = 0$$

Fig. 47: Visualization of the wave equation with Gaussian initial conditions.